1997

Innovative lateral bracing of high performance steel highway bridge I-girders

Sean Stephen Murphy
Lehigh University

Murphy, Sean Stephen

Innovative Lateral Bracing of High Performance Steel Highway Bridge I-Girders

June 1, 1997

INNOVATIVE LATERAL BRACING OF HIGH PERFORMANCE STEEL HIGHWAY BRIDGE I-GIRDERS

by

Sean Stephen Murphy

A Thesis

Presented to the Graduate and Research Committee

of Lehigh University

in Candidacy for the Degree of

Master of Science

in

Civil and Environmental Engineering

Lehigh University

May 7, 1997

This thesis is accepted and approved in partial fulfillment of the requirements for the Master of Science.

May 7, 1997

Date

Dr. Richard Sause, Thesis Advisor

Dr. Le-Wu Lu, Chairman of Department

Acknowledgments

I sincerely thank Dr. Richard Sause for serving as my advisor during my research. He patiently and clearly explained many concepts to me and vastly increased my understanding, not only in the area of lateral-torsional buckling but also in structural engineering in general. He knew that I could accomplish analytical work, and I greatly appreciate his faith in me. Dr. Dayan Xiao deserves thanks and recognition for his assistance with the finite element models.

I would like to extend my thanks to the Dr. John W. Fisher, Director of the Center for Advanced Technology for Large Structural Systems (ATLSS) for my support during my studies at Lehigh University. I am pleased and honored that I had the opportunity to work at the wonderful facility, and to interact with such knowledgeable faculty, staff, and fellow students.

For their love and support, I thank my mother, Dr. Susan K. H. Kurjiaka, and my brother and best friend, Matthew E. Murphy. Without their long distance support, I would not have been able to complete this thesis. There are many others who deserve my thanks: people who have influenced me personally and who have helped me become not only the engineer I am now, but the person. The list of those people would be too long to list here. I thank all of those people, friends from The RBA Group, Clemson University, and Lehigh University.

Table of Contents

Item Page

Title Page i

Certificate of Approval ii

Acknowledgments iii

List of Tables vii

List of Figures viii

Abstract 1

1. Introduction 2

1.1 Scope 2

1.2 Objective and Scope 2

1.3 Approach 3

1.4 Outline of Report 3

2. Background 4

2.1 Introduction 4

2.2. Buckling of Steel Bridge I-Girders 4

2.3 Design of I-Girder Bridge Superstructures 7

2.3.1 Components of I-Girder Bridge Superstructures 7

2.2.2 Loading Conditions and Limit States for Composite I-Girder of Bridge Superstructures 9

2.3.3 AASHTO Equations 12

2.4 Previous Research on Lateral-Torsional Buckling of Girders 17

2.4.1 Introduction 17

2.4.2 Lateral-torsional Buckling Analysis 17

2.4.4 Improved Lateral-Torsional Buckling Behavior 19

2.5 Prototype Bridges Used in Thesis 20

3. Bridge Girder Design Concepts 26

3.1 Introduction 26

3.2 Flange Rotational Restraint Brace Concept 26

3.2.1 Description 26

3.2.2 Behavior 27

Table of Contents, continued

Item Page

3.3 Batten Plate Concept 29
3.3.1 Description and Behavior 29
3.3.2 Finite Element Analysis 32
3.4 Pairs of Girders 35
3.4.1 Description 35
3.4.2 Benefits and Concerns 36
3.5 Summary 36
4. Finite Element Models of Lateral-Torsional Buckling Behavior 46
4.1 Introduction 46
4.2 Background 46
4.3 Finite Element Analysis 49
4.3.1 Introduction 49
4.3.2 Modeling of Test Specimen B2B-C1 49
4.3.3 Results of Analyses 52
4.3.4 Models of FRRB Behavior 53
4.4 Summary 56
5. Analysis of Girders with Flange Rotational Restraint Braces 68
5.1 Introduction 68
5.2 Finite Difference Solution of Differential Equations 70
5.2.1 Introduction 70
5.2.2 Formulation of Finite Difference Equations 70
5.2.3 Boundary Conditions 72
5.2.4 Assembling and Solving the Finite Difference Equations 76
5.3 Finite Difference Analysis of the Prototype Girders 79
5.4 Consideration of Inelastic Lateral-Torsional Buckling 82
5.5 Alignment Chart Analysis Method 85
5.5.1 Introduction 85
5.5.2 Analysis Procedure 87
5.5.3 Alignment Chart Analysis of Prototype Girders 89
5.6 Summary 90
6. Finite Element Analysis of Girders with Flange Rotational Restraint Braces 107

Table of Contents, continued

Item Page

6.1 Introduction 107
6.2 Finite Element Models of Prototype Girders 107
6.3 Results of Analysis 111
6.3.1 General Results 111
6.3.2 Discussion of Selected Cases 112
6.4 Summary 114
7. Conclusions, and Future Work 126
7.1 Conclusions 126
7.2 Future Work 128
References 129
Vita 131

List of Tables

Table Page

3.1 Boundary conditions at midspan of finite element models 38
3.2 Boundary conditions at support end of finite element models 38
3.3 Results of finite element models of girders with batten plates 39
4.1 Dimensions of beam specimens (Kubo and Fukumoto (1988)) 57
4.2 Mean material properties (Kubo and Fukumoto (1988)) 57
4.3 Boundary conditions at midspan of finite element models 57
4.4 Boundary conditions at support end of finite element models 58
4.5 Results of finite element model 58
4.6 Results of modified finite element models 58
5.1 Dimensions of prototype girder cross-sections 92
5.2 Dimensions of FRRBs 92
5.3 Results of alignment chart analysis 92
5.4 Results of analysis methods 93
5.5 Critical lateral-torsional buckling moment comparisons 93
6.1 Boundary conditions at midspan of finite element models 116
6.2 Boundary conditions at lateral supports of finite element models 116
6.3 Boundary conditions at support end of finite element models 117
6.4 Lateral-torsional buckling moment capacities for 33.5 m span girders 117
6.5 Lateral-torsional buckling moment capacities for 50 m span girders 117

List of Figures

Figure Page

2.1 Deflections caused by load (after Galambos (1968)) 22
2.2 Load-deflection curves for beams (after Galambos (1968)) 23
2.3 Normalized lateral-torsional buckling moment capacity versus unbraced length 23
2.4 Isometric view of typical girder arrangement 24
2.5 Typical diaphragm details 24
2.6 AASHTO terminology for cross-sections 25
2.7 Span and unbraced lengths used in thesis 25
3.1 Diaphragm with flange rotational restraint brace 40
3.2 Isometric view of girder pair with FRRBs 40
3.3 Comparison of lateral deflected shapes of compression flange 41
3.4 Elevation of stiffened beam (after Takabatake (1988)) 42
3.5 Web stiffeners and batten plates (after Takabatake (1988)) 42
3.6 Cross-section of finite element models for girders with batten plates 43
3.7 Stress-strain relationship used in finite element models 43
3.8 Location of batten plate centerlines in finite element models 44
3.9 Cross-section of girder at midspan 44
3.10 Cross-section of girder at support end 45
3.11 Comparison of framing plans 45
4.1 Cross-section from Kubo and Fukumoto (1988) 59
4.2 Normalized moment versus deflection (from Kubo and Fukumoto (1988)) 59
4.3 Normalized moment versus longitudinal strain in compression flange (from Kubo and Fukumoto (1988)) 60
4.4 Stress-strain relationship used in finite element models 60
4.5 Residual stress distribution for finite element models 61
4.6 Location of nodes at midspan of finite element models 61
4.7 Location of elements at midspan of finite element models 61
4.8 Normalized moment versus deflection for finite element model of B2B-C1 62
4.9 Deflected shape of finite element model of B2B-C1 62
4.10 Normalized moment versus longitudinal strain in compression flange for finite element model of B2B-C1 63

List of Figures continued

Figure

Page

4.11 Layout of compression flange with FRRB for modified finite element model 63

4.12 Normalized moment versus deflection for modified finite element model of B2B-C1 with FRRB 64

4.13 Deflected shape at end of analysis of modified finite element model of B2B-C1 with FRRB 64

4.14 Deflected shape immediately after lateral-torsional buckling of modified finite element model of B2B-C1 with FRRB 65

4.15 Normalized moment versus longitudinal strain in compression flange for modified finite element model of B2B-C1 with FRRB 65

4.16 Normalized moment versus deflection for modified finite element model of B2B-C1 with rotational spring 66

4.17 Deflected shape of modified finite element model of B2B-C1 with rotational spring 66

4.18 Normalized moment versus longitudinal strain in compression flange for modified finite element model of B2B-C1 with rotational spring 67

5.1 Cross-section of girder 94

5.2 Locations of diaphragms with FRRBs 94

5.3 Discretization of unbraced length for finite difference analysis 95

5.4 Boundary conditions for finite difference analysis 96

5.5 Deflected shape of portion of girder pair with FRRB 96

5.6 Comparison of AASHTO, classical, and finite difference solutions for 33.5 m span 485 MPa yield strength steel girder 97

5.7 Comparison of AASHTO, classical, and finite difference solutions for 33.5 m span 690 MPa yield strength steel girder 97

5.8 Comparison of finite difference solutions for L_b and L_b^{FRRB} with J included for 33.5 m span 485 MPa yield strength steel girder 98

5.9 Comparison of finite difference solutions for L_b and L_b^{FRRB} with J included for 33.5 m span 690 MPa yield strength steel girder 98

5.10 Comparison of finite difference solutions for L_b and L_b^{FRRB} with J included for 50 m span 485 MPa yield strength steel girder 99

5.11 Comparison of finite difference solutions for L_b and L_b^{FRRB} with J included for 50 m span 690 MPa yield strength steel girder 99

5.12 Comparison of finite difference solutions for L_b and L_b^{FRRB} without J for 33.5 m span 485 MPa yield strength steel girder 100

List of Figures continued

Figure Page

5.13 Comparison of finite difference solutions for L_b and L_b^{FRRB} without J for 33.5 m span 690 MPa yield strength steel girder 100

5.14 Comparison of finite difference solutions for L_b and L_b^{FRRB} without J for 50 m span 485 MPa yield strength steel girder 101

5.15 Comparison of finite difference solutions for L_b and L_b^{FRRB} without J for 50 m span 690 MPa yield strength steel girder 101

5.16 Comparison of AASHTO design limits with and without K factor for 33.5 m span 485 MPa yield strength steel girder 102

5.17 Comparison of AASHTO design limits with and without K factor for 33.5 m span 690 MPa yield strength steel girder 102

5.18 Comparison of AASHTO design limits with and without K factor for 50 m span 485 MPa yield strength steel girder 103

5.19 Comparison of AASHTO design limits with and without K factor for 50 m span 690 MPa yield strength steel girder 103

5.20 Alignment chart with sidesway inhibited (adapted from ACI (1995)) 104

5.21 Lateral deflection of girder pair and braced frame 105

5.22 Joints and unbraced lengths for alignment chart analysis 106

6.1 Top flange plan for 33.5 m span girder 118

6.2 Top flange plan for 50 m span girder 118

6.3 Stress-strain relationship used in finite element models 119

6.4 Residual stress distribution used in finite element models 119

6.5 Initial out-of-straightness for 33.5 m span girder with standard diaphragms 120

6.6 Initial out-of-straightness for 50 m span girder with standard diaphragms 120

6.7 Initial out-of-straightness for 33.5 m span girder with FRRBs 120

6.8 Initial out-of-straightness for 50 m span girder with FRRBs 121

6.9 Boundary conditions at midspan of FRRB 121

6.10 Location of nodes at midspan of 33.5 m span girder 121

6.11 Location of elements adjacent to midspan of 33.5 m span girder 122

6.12 Location of nodes at point of maximum lateral deflection of 50 m span girder 122

6.13 Location of elements at point of maximum lateral deflection of 50 m span girder 122

6.14 Normalized moment versus deflection for finite element model of 33.5 m span 690 MPa yield strength steel girder with smaller initial out-of-straightness 123

6.15 Deflected shape for primary unbraced length of finite element model of 33.5 m span 690 MPa yield strength steel girder with smaller initial out-of-straightness 123

6.16 Normalized moment versus longitudinal strain in compression flange for finite element model of 33.5 m span 690 MPa yield strength steel girder with smaller initial out-of-straightness 124

6.17 Normalized moment versus deflection for finite element model of 50 m span 485 MPa yield strength steel girder with smaller initial out-of-straightness 124

6.18 Deflected shape for primary unbraced length of finite element model of 50 m span 485 MPa yield strength steel girder with smaller initial out-of-straightness 125

6.19 Normalized moment versus longitudinal strain in compression flange for finite element model of 50 m span 485 MPa yield strength steel girder with smaller initial out-of-straightness 125

Abstract

This report investigates the design and behavior of high performance steel I-shaped girders with flange rotational restraint braces (FRRBs). An FRRB attaches directly to the compression flange of an I-girder at locations of lateral support (diaphragms). The FRRB allows an increase in the diaphragm spacing by improving the lateral-torsional buckling behavior of the girder. Increased diaphragm spacing improves the economy of a steel highway girder bridge. The result is significant because lateral-torsional buckling is a controlling limit state for the design of highway bridge girders using high performance steel with high strength (yield strength of 485 MPa (70 ksi) or more).

Finite element models for simulating lateral-torsional buckling behavior of highway bridge girders are developed and compared to previous test results. Analysis methods are developed to determine the lateral-torsional buckling behavior of I-girders with FRRBs. Finite difference and alignment chart analysis methods are used to determine the spacing of diaphragms with FRRBs for several prototype girders. Finite element models are used to verify the results of the analysis methods.

The results show that diaphragms with FRRBs allow the diaphragm spacing to be increased. The increase in diaphragm spacing is made possible by the improved lateral-torsional buckling behavior of girders with FRRBs. Laboratory tests are needed to further verify the analysis methods and results.

1. Introduction

1.1 Scope

This research is part of a project entitled "Innovative Bridge Designs Using High Performance Steels." The goal of the project is to investigate the feasibility of using high performance steel (HPS) in highway bridges. The first phase of the project investigated the use of HPS in current bridge designs. The research reported herein is part of the second phase of the project that focuses on new bridge design concepts that take advantage of the properties of HPS.

The first phase of the project found that the weight of steel bridge I-girders designed according to current highway bridge design practice can be reduced using HPS. However, the effectiveness of using steels with high yield strengths (yield strength of 485 MPa (70 ksi) or more) is constrained by buckling, deflection, and fatigue design limits. Diaphragms, diaphragm connection plates, and other attachments to bridge girders also reduce the cost effectiveness of HPS designs. The results of the first phase of the project indicated that innovative designs were needed which would eliminate the barriers posed by these design limits. This report investigates the design and behavior of HPS girders using innovations that address the barriers related to lateral-torsional buckling.

1.2 Objective and Scope

This report investigates innovative lateral bracing of HPS I-girders. The main focus is on a bracing concept which restrains the rotation of the compression flange (in its own plane). The objective of the report is to investigate the design and behavior of HPS I-girders which are braced using the flange rotational restraint brace (FRRB) concept. Finite element models to analyze the behavior of I-girders with FRRBs are developed. Analysis methods are developed

to enable I-girders with FRRBs to be used for highway bridge designs. Finite element models are used to verify the analysis methods.

1.3 Approach

The research presented in this report was conducted in the following steps:

(1) Identify methods to improve the lateral-torsional buckling behavior of HPS I-girders,
(2) Develop finite element models to simulate lateral-torsional buckling behavior of HPS girders, using data from previous research to calibrate the models,
(3) Develop analysis methods to determine the lateral-torsional buckling behavior of I-girders with FRRBs, and
(4) Perform finite element analyses to verify the analysis methods and to demonstrate the validity of the FRRB concept.

1.4 Outline of Report

The report is organized as follows. Design of steel highway bridge girders and previous research on lateral-torsional buckling is reviewed in Chapter 2. Chapter 3 outlines concepts for lateral bracing of bridge girders and provides a more detailed explanation of the FRRB concept. The topics discussed in Chapters 2 and 3 apply to positive moment regions of bridge girders. Chapter 4 discusses the development and verification of finite element models to simulate lateral-torsional buckling behavior of I-girders. Chapter 5 develops finite difference and alignment chart analysis methods to determine the lateral-torsional buckling behavior of I-girders with FRRBs. Chapter 6 uses finite element analyses to verify the analysis methods developed in Chapter 5. The items discussed in Chapters 4, 5, and 6 are focused on simply supported, single span bridge I-girders. The final chapter provides conclusions and recommendations for further research into the FRRB concept.

2. Background

2.1 Introduction

This thesis focuses on the lateral-torsional buckling behavior of bridge girders. In this chapter, buckling of girders is discussed with an emphasis on lateral-torsional buckling. The design of steel girder bridges is then discussed to show that the construction stage can be a critical stage for the lateral-torsional buckling behavior of girders. The pertinent code equations for the construction stage lateral-torsional buckling capacity are discussed. Previous lateral-torsional buckling research is then reviewed briefly. Finally, the bridges used as examples in this thesis are discussed.

2.2. Buckling of Steel Bridge I-Girders

The components of a steel bridge girder can buckle in three ways: (1) web buckling, (2) local flange buckling, and (3) lateral-torsional buckling. Web buckling is a general term for the three modes of buckling, bend buckling, shear buckling, and vertical buckling, that can occur in the web. All three modes of web buckling can be related to the thickness of the web relative to the web depth. Local flange buckling can occur when the compression flange is thin relative to the width of the flange. Lateral-torsional buckling is lateral movement of the compression flange accompanied by twisting of the entire cross-section. Lateral-torsional buckling is related not only to the dimensions of the girder cross-section but also to the distance between the locations at which the compression flange is laterally supported (braced).

For all forms of buckling, the susceptibility of the girder to buckling can be related to the slenderness of the related components. As the ratio of the width or height to the thickness (i.e., the slenderness ratio) increases, the component is increasingly slender. Components with high slenderness ratios are referred to as slender. Components with a slenderness ratio that is less than the certain limits are typically referred to as stocky.

Deflections can be in-plane or out-of-plane with respect to the applied load. Deflections in the direction of loading are referred to as in-plane deflections. For typical girders, the in-plane loading and deflections are intended to be coincident with the major principal axis. Figure 2.1(a) shows the in-plane deflection, v, due to a load applied in the direction of the vertical axis (labeled as the y axis). The orientations of the axes used throughout this thesis are also shown. The longitudinal axis of the girder is the z axis. The loading acts through the shear center of the girder in the y-z plane. The shear center and centroid of the cross-sections in Figure 2.1 are shown at the same location, which is the case when the girder is doubly-symmetric (top and bottom flanges of equal size). However, the flanges often have different sizes, and, in this case, the girder is symmetric about the y axis only, and the shear center will be along the web above or below the centroid.

Figure 2.1(b) shows in-plane and out-of-plane deflections. The lateral deflection, u, occurs along the transverse axis (x axis). The twist angle, ϕ, is centered about the point C_{LB}. The center of rotation, C_{LB}, is a distance y_{LB} below the centroid of the girder. In many cases, C_{LB} is close to the junction between the tension flange and the web.

The out-of-plane deflections shown in Figure 2.1(b) are those which accompany lateral-torsional buckling. Two coupled differential equations describe the lateral-torsional buckling equilibrium state in the girder. The solution of the equations describes the critical bending moment at which the girder will buckle in a lateral-torsional mode. The coupled differential equations for a girder symmetric about the y axis are as follows:

$$EI_y u^{iv} + M_x \phi'' + 2M_x' \phi' = 0 \qquad \text{(Eq. 2.1)}$$

$$EI_\omega \phi^{iv} - (GJ + M_x \beta_x)\phi'' - M_x' \beta_x \phi' + M_x u'' = 0 \qquad \text{(Eq. 2.2)}$$

where E is the elastic modulus, I_y is the moment of inertia with respect to the y axis, M_x is the applied moment about the x axis, I_ω is the warping moment of inertia, G is the shear modulus, J

is the torsional constant, β_x is a property related to symmetry about the x axis, and M'_x is the gradient of the applied moment. For a girder symmetric about the x axis, β_x is equal to zero.

Figure 2.2 shows hypothetical bending moment versus vertical deflection curves for a girder (Galambos, 1968). Curve OAE represents the case where neither local nor lateral-torsional buckling occurs. The girder is able to experience significant vertical deflections without loss of load-carrying capacity. Curve OBF represents the case where lateral-torsional or local buckling limits the load-carrying capacity while the girder is in the elastic range. Elastic buckling occurs while the entire cross-section is in the elastic range. Curves OCG represents the case where inelastic lateral-torsional or local buckling limits the load-carrying capacity. The inelastic buckling occurs after a portion of the girder cross-section is yielded. Bucking can occur after the cross-section is fully yielded, as represented by curve ODH.

Lateral-torsional buckling of a girder is strongly related to the unbraced length, L_b, defined as the distance between points of lateral support. A lateral support restrains the lateral and twisting deflections, but not the vertical deflections. Figure 2.3 shows the hypothetical normalized moment capacity of a steel girder, considering lateral-torsional buckling. The normalized bending moment capacity is plotted versus the unbraced length, L_b. Branch AB of the curve covers cases where the unbraced length is relatively short. The girder is able to reach the full moment capacity of the cross-section. Branch CD covers cases where the unbraced length is relatively long and girder moment capacity is controlled by elastic lateral-torsional buckling. Branch BC is a straight-line transition between the short unbraced length and the long unbraced length cases. Branch BC covers cases where the girder moment capacity is controlled by inelastic lateral-torsional buckling. The actual shape of the transition is slightly concave-down although most design specifications treat it as a straight line as shown in Figure 2.3.

2.3 Design of I-Girder Bridge Superstructures

2.3.1 Components of I-Girder Bridge Superstructures

The superstructure of a steel I-girder bridge consists of the primary load-carrying components that directly support the traffic on the bridge and secondary components that brace the primary load-carrying components. Modern steel girder highway bridges have a reinforced concrete deck, supported by parallel steel I-shaped girders. The behavior of the individual girders is controlled by several factors, including the distance between locations of lateral support, the yield strength of the various components of the cross-section, and the dimensions of the girder cross-section. Other important factors include the type of loading considered and the stage in the life of the bridge. If the steel bridge girder is made composite with the concrete deck, the behavior of the girder changes during the construction stage.

The superstructure of a steel I-girder bridge includes primary and secondary components. The primary components resist the bending moments and shears created by the loads on the bridge. In a typical steel I-girder bridge, the primary members are steel girders. The girders may be rolled steel shapes, often called beams or rolled beams, or I-shaped girders composed of welded plates, often called girders or I-girders. Rolled beams are used for shorter span bridges while I-girders are used for longer spans.

The secondary components provide lateral support to the primary load-carrying components. The secondary components of a steel girder bridge are called diaphragms. The diaphragms connect the girders across the width of the bridge. Figure 2.4 shows an isometric view of a segment of two steel I-girders. The arrangement of the secondary members can be seen in relation to the primary members. Note that the unbraced length, L_b, is equal to the diaphragm spacing. The diaphragms serve as locations of lateral support. The details of the diaphragms and connection to the girders are simplified in the figure to provide clarity.

The LRFD Bridge Design Specifications (1994) of the American Association of State Highway and Transportation Officials (AASHTO) briefly discuss the need for diaphragms. The AASHTO specifications list some of the cases when diaphragms are needed:

(1) stability of top flanges in compression prior to composite action with the deck,
(2) stability of bottom flanges in compression at all times,
(3) distribution of vertical dead and live loads between girders, and
(4) transfer of lateral wind loads on the fascia girders to the rest of the superstructure and the vertical supports.

One of the roles of the diaphragms is to distribute load between the primary members (i.e., to provide redundancy to the superstructure). If one girder is damaged or otherwise loses its load-carrying ability, the diaphragms redistribute the load, keeping the bridge from suffering an immediate catastrophic failure. However, the amount of redundancy provided by the diaphragms after the concrete deck becomes composite with the girders is a point of contention among bridge engineers (Mertz, 1996). After the concrete deck cures and becomes composite with the girders, it is more effective in distributing loads between girders than the diaphragms. So long as the deck remains composite with the girders, the deck provides the required redundancy.

Figure 2.5 shows a simplified connection detail between the girders and the diaphragm. The X-frame diaphragm is attached to the diaphragm connection plates which are attached to the web and flanges of the girders. The X-frame diaphragm components are typically angles with gusset plates welded to their ends; the gusset plates are not shown in Figure 2.5 for clarity. The gusset plates are then bolted to the connection plate which is welded to the flanges and web of the girder. The welds of the diaphragm connection to the flanges and the web tend to be critical fatigue details.

The diaphragms are typically installed in the field during the erection of the girders. When a girder is erected into position, the diaphragm gusset plates are bolted to the diaphragm connection plates. Since the connection plates and gusset plates are bolted together in the field, precise placement of the bolt holes in the gusset plates and the connection plates is required in the fabrication shop. Field installation, coupled with tight fabrication tolerances, make the diaphragm connection an expensive item in the superstructure. Although the amount of steel used to fabricate the diaphragms may be small, the labor and precision required in their fabrication and installation make the cost per unit weight of diaphragms very high (Huzzard, 1996).

The fifteenth edition of the AASHTO Standard Specifications for Highway Bridges (1992) arbitrarily limited the maximum diaphragm spacing to 7.6 m (25 ft) partly to provide lateral stability to the girders. The AASHTO LRFD Bridge Design Specifications (1994) requires only that the diaphragm spacing be determined for the construction stage or other applicable conditions. Although the current AASHTO LRFD specifications do not limit the spacing of the diaphragms, the practical limit on diaphragm spacing is approximately 7.6 m, particularly for HPS girders that are optimized to reduce their weight.

2.2.2 Loading Conditions and Limit States for Composite I-Girder of Bridge Superstructures

Several factors affect the design and behavior of a bridge superstructure. One factor is the loading conditions which are the direction, amplitude, and the variation of amplitude with time of the forces acting on the bridge. A second factor is the limit states of the components of the bridge superstructure. Limit states are limits on the capability of the components of a bridge to adequately resist the loading conditions. These two factors are related to the stages in the life of a bridge. The life span of a highway bridge has two primary stages: (1) the construction stage and (2) the service stage. The construction stage of the bridge includes the fabrication and

erection of the various components of the bridge. The service stage is the usable life of the bridge which may include rehabilitation and repairs. The construction stage is short compared to the service stage in the life of a modern highway bridge.

In each stage, the bridge experiences loads from both internal and external sources. Internal sources of loads are the components of the bridge superstructure itself or attachments like utility pipes; these are commonly referred to as the dead load. External sources include loads from vehicles, wind or earthquakes.

Combinations of different loads on the bridge are the loading conditions for which the bridge is designed (AASHTO, 1994). While many loading conditions need to be considered for the service stage, only a few loading conditions are considered for the construction stage. One important loading condition is the dead load of the bridge when the bridge is only partially completed. In the construction stage, each component has to be designed to resist its own factored dead load and the factored dead load for the components it supports. For instance, the steel superstructure must support the factored dead load from its own weight plus the weight of the concrete deck.

For each loading condition, each bridge component must be designed for one or more limit states. Some of the limit states used in the design of steel bridge superstructure are strength, deflection, fatigue resistance, web buckling, local flange buckling, and lateral-torsional buckling. The importance of each limit state changes between the construction and service stages. For instance, deflection and fatigue limit states are concerns for the bridge under the effect of live load during the service stage. Strength and the various buckling limits are concerns during both the construction and the service stages.

Bridge girders designed using high performance steels may be lighter than girders designed using lower strength conventional steels, but their design can be controlled by limit

states that do not control designs using lower strength steels (Sause, 1995). High performance steel (HPS) is steel with a yield strength of 485 MPa (70 ksi) or more. High performance steel is expected to have better weldability, ductility, and fracture toughness than other high yield strength steels. A girder designed using high performance steel would be smaller and lighter than a girder designed using conventional strength steels when all other factors are held constant.

Deflection limit states for HPS bridge girders are more critical than for conventional steel bridge girders. High strength steels have the same modulus of elasticity as conventional steels. A smaller, lighter HPS girder would deflect more than a conventional steel girder under the same load. Fatigue limit states for HPS bridge girders are also more critical than for conventional steel girders. Since the stress in a HPS girder is higher than in a conventional steel girder under the same loading conditions, the HPS girder would have a lower fatigue life unless more fatigue-resistant details are used. Buckling limit states for HPS girders are also more critical than for conventional steel girders since the buckling limit states are often independent of the yield strength of the material.

The girders in a bridge superstructure support the dead load of the bridge, including the wet concrete of the deck, during the construction stage. This dead load can be a significant portion of the total vertical load acting on the structure and is resisted only by the girders. A light-weight steel girder may be designed to satisfy all of the necessary limit states during the service stage when it is composite with the concrete deck. However, the web or compression flange may be slender during construction, and the stability of the girder may be a concern. After the compression flange is composite with the concrete deck, the flange has continuous lateral support in the positive moment region, eliminating the stability concern. Furthermore, after the compression flange is composite with the deck, the depth of the compression zone in

the web and the level of stress of compressive flexural stresses in the web and compression flange decrease with any additional load (e.g., wearing surfaces and live load), greatly reducing the possibility of web and local flange buckling. As a result, the compression flange in the positive moment region of a composite I-girder bridge tends to be small, and tends to be more critically loaded during the construction stage.

2.3.3 AASHTO Equations

The AASHTO LRFD Bridge Design Specifications (1994) include equations to determine the lateral-torsional buckling moment that are much simpler than the solution for the coupled differential equations, Equations 2.1 and 2.2. Figure 2.6 shows the nomenclature used by AASHTO LRFD in calculations of the slenderness and lateral-torsional buckling moment capacity of steel girders. The cross-section in Figure 2.6 is shown for the non-composite construction stage of the positive moment region of a girder.

The AASHTO equations assume that the section is doubly symmetric. This eliminates the β_x term in Equation 2.2. Most bridge girders are not doubly symmetric, as a large compression flange is not required for the service stage loading conditions in the positive moment region. A second assumption is that the moment gradient, M_x', can be ignored in the solution of the differential equations (i.e., uniform moment), and then can be included after the lateral-torsional moment is determined. The moment distribution factor, C_b, is used to adjust the lateral-torsional moment based on the actual distribution of the moment.

The primary focus of this thesis is lateral-torsional buckling of steel girders during construction. AASHTO LRFD Article 6.10.10 addresses constructibility of a steel I-girder. The constructibility articles use the non-compact design criteria for all girders and assumes non-composite behavior during construction. The nominal flexural resistance of the girder is considered in Article 6.10.10.2, and is defined by equations dealing with the web slenderness,

compression flange slenderness, and compression flange bracing (i.e., lateral support of the compression flange). Web slenderness is addressed in Article 6.10.10.2.2. Compression flange slenderness is addressed in Article 6.10.10.2.3. The compression flange bracing is addressed in Article 6.10.10.2.4.

In the following discussion of the design criteria, several references are made to the web slenderness and compression flange slenderness. The quantity $b_f/2t_f$ is the compression flange slenderness ratio and the quantity $2D_c/t_w$ is the web slenderness ratio. D_c is the depth of the web in compression, and b_f, t_f, D_c, and t_w are shown in Figure 2.6.

AASHTO LRFD Article 6.10.10.2.1 states that a girder which satisfies web slenderness and compression flange slenderness and are adequately braced against lateral-torsional buckling have a nominal flexural resistance, M_n, equal to the following:

$$M_n = R_b R_h M_y \qquad \text{(Eq. 2.3)}$$

where R_b and R_h are the flange stress reduction factors.

The flange stress reduction factors are defined in Article 6.10.5.4. The first is the hybrid reduction factor, R_h, and is for hybrid girders where the yield stress or the stress level in the flanges exceeds the yield strength of the web. The capacity of the flanges is reduced by R_h to account for the increased stresses in the flanges from yielding of the web (compared to stresses determined from beam theory). For girders with approximately equal yield strengths in the flanges and web, R_h equals 1.0. In this thesis, R_h is taken as 1.0.

The second flange stress reduction factor is the load shedding factor, R_b. The load shedding factor takes into account the non-linear variation of stresses caused by flexural buckling of a slender web. As the web buckles, it redistributes (sheds) stresses into the flanges. Rather than increase the stresses in the flanges, the reduction factor accounts for the shedding

of stresses into the flanges. R_b is used if a longitudinal stiffener is not provided and if the slenderness of the web exceeds the following:

$$\frac{2D_c}{t_w} \le \lambda_b \sqrt{\frac{E}{f_c}} \qquad \text{(Eq. 2.4)}$$

where λ_b is used to define the amount of restraint provided to the web by the flanges.

If the area of the compression flange is greater than or equal to the area of the tension flange then λ_b equals 5.76. Otherwise, λ_b equals 4.64. The load shedding factor is calculated as follows:

$$R_b = 1 - \left(\frac{a_r}{1200 + 300a_r}\right)\left(\frac{2D_c}{t_w} - \lambda_b \sqrt{\frac{E}{f_c}}\right) \qquad \text{(Eq. 2.5)}$$

where f_c is the current stress level in the compression flange,

$$a_r = \frac{2D_c t_w}{A_{fc}} \qquad \text{(Eq. 2.6)}$$

with A_{fc} is the area of the compression flange.

Article 6.10.10.2.2 defines the limits on the web slenderness by reference to Article 6.10.5.3.2b. There are two limits given in that article. One is without longitudinal stiffeners and the other includes the effect of longitudinal stiffeners against web buckling. The web slenderness limit without longitudinal stiffeners is as follows:

$$\frac{2D_c}{t_w} \le 6.77 \sqrt{\frac{E}{f_c}} \qquad \text{(Eq. 2.7)}$$

The web slenderness limit for girders with longitudinal stiffeners is as follows:

$$\frac{2D_c}{t_w} \le 11.63 \sqrt{\frac{E}{f_c}} \qquad \text{(Eq. 2.8)}$$

Article 6.10.10.2.3 defines the limit on the compression flange slenderness. The slenderness limit in LRFD Article 6.10.5.3.3c is used. The compression flange slenderness during construction is strictly limited to:

$$\frac{b_f}{2t_f} \le 1.38\sqrt{\frac{E}{f_c\sqrt{\frac{2D_c}{t_w}}}} \qquad \text{(Eq. 2.9)}$$

Article 6.10.10.2.4 provides a limit on the spacing of the compression flange bracing (provided by diaphragms and other braces) for the construction stage. If the unbraced length exceeds the limit, the nominal flexural resistance is calculated using Article 6.10.6.4. If the unbraced length is less than the limit, the yield moment can be reached, and the nominal flexural resistance is given by Equation 2.3. This corresponds to a girder in Branch AB of Figure 2.5. The limit on the unbraced length is as follows:

$$L_b = 1.76 r_t \sqrt{\frac{E}{F_{yc}}} \qquad \text{(Eq. 2.10)}$$

where r_t is taken as the radius of gyration of the compression flange about the vertical axis for the construction stage, and F_{yc} is the specified minimum yield strength of the compression flange.

If the limit on the unbraced length given by Equation 2.10 is exceeded, then the nominal flexural resistance is calculated using Article 6.10.6.4. The article provides the lateral-torsional buckling resistance for stocky web girders and slender web girders.

A stocky web girder is not susceptible to flexural buckling of the web. This allows the St. Venant torsional resistance, given by GJ in Equation 2.2, to be included in calculating the elastic lateral buckling moment. Also, Article 6.10.6.4.1 neglects inelastic lateral-torsional buckling of stocky web girders. A slender web girder is susceptible to flexural buckling of the web, and inelastic buckling.

If a longitudinal stiffener is provided or the web slenderness ratio satisfies the limit of Equation 2.4, then the web is stocky. The nominal flexural resistance, M_n, is the lateral-torsional buckling moment, as follows:

$$M_n = 3.14EC_bR_h\left(\frac{I_{yc}}{L_b}\right)\sqrt{0.772\left(\frac{J}{I_{yc}}\right)+9.87\left(\frac{d}{L_b}\right)^2} \le R_h M_y \qquad \text{(Eq. 2.11)}$$

where I_{yc} is the moment of inertia of the compression flange about the vertical axis and d is the total depth of the web.

If the web slenderness exceeds the limit of Equation 2.4, two unbraced limits are calculated, the plastic length, L_p, and the transition length between elastic and inelastic buckling, L_r. The plastic length, which defines point B, on Figure 2.3 is as follows:

$$L_p = 1.76r'\sqrt{\frac{E}{F_{yc}}} \qquad \text{(Eq. 2.12)}$$

where r' is the radius of gyration of the compression flange about the vertical axis. It should be noted that r' is equal to r_t (in Equation 2.10) only for the construction stage.

The transition length, L_r, is determined by setting Equation 2.11 equal to one half the yield moment (with R_h = 1 and C_b = 1) and solving for L_b. Since the web is slender, the St. Venant torsional resistance GJ is set to zero. L_r is as follows:

$$L_r = \sqrt{\frac{19.71I_{yc}d}{S_{xc}}\frac{E}{F_{yc}}} \qquad \text{(Eq. 2.13)}$$

where S_{xc} is the section modulus of the entire steel girder cross-section about the horizontal axis.

Slender web girders can buckle inelastically when L_b is between L_p and L_r. For those girders, the lateral-torsional buckling moment is determined, as a function of L_b, from a straight

line between the yield moment and L_p, and one-half of the yield moment and L_r (see Figure 2.3). The nominal flexural resistance is calculated as follows:

$$M_n = C_b R_b R_h M_y \left[1 - 0.5\left(\frac{L_b - L_p}{L_r - L_p}\right)\right] \leq R_b R_h M_y \qquad \text{(Eq. 2.14)}$$

If the unbraced length is greater than L_r, then the elastic lateral-torsional buckling moment is calculated as follows:

$$M_n = C_b R_b R_h \frac{M_y}{2}\left(\frac{L_r}{L_b}\right)^2 \leq R_b R_h M_y \qquad \text{(Eq. 2.15)}$$

The main focus of this thesis is the lateral-torsional buckling of bridge I-girders during the construction stage. Equation 2.4 defines the slenderness of the web. For stocky webs, Equation 2.11 determines the lateral-torsional buckling resistance. Most typical steel bridge I-girders will be slender during the construction stage, and Equation 2.14 and 2.15 will determine the lateral-torsional buckling resistance.

2.4 Previous Research on Lateral-Torsional Buckling of Girders

2.4.1 Introduction

Previous research has investigated the lateral-torsional buckling behavior of beams and girders in the elastic and inelastic ranges. Most of the research has considered the short span rolled beams or small welded girders that are used in buildings. Earlier work, for example Galambos (1963), dealt with solutions for inelastic buckling. Later work proposed methods to improve the elastic or inelastic behavior of beams. The previous research related to the research in this thesis is briefly summarized in this section.

2.4.2 Lateral-torsional Buckling Analysis

Austin, et. al (1957) analytically investigated the lateral-torsional buckling resistance of doubly-symmetric beams with varying elastic end-restraints. In frame structures, connections to

flexural members, such as beam-to-column connections, provide end restraints which vary between the pinned condition and the fully rigid condition. Austin, et. al (1957) used numerical integration of Equations 2.1 and 2.2 to analyze a variety of conditions. The end restraint was included in the boundary conditions. This restraint was provided equally to both the compression and tension flange.

Galambos (1963) investigated the inelastic lateral-torsional buckling of rolled wide flange beams under constant moment. An analytical solution for inelastic buckling was determined from the classical solution for elastic buckling by reducing the lateral and torsional resistance to account for the yielding that occurs in inelastic buckling. Galambos studied initially straight wide flange beams without imperfections. The investigation assumed the beam cross-section did not distort, indicating that web and flange buckling were not considered. Residual stresses, which cause the tips of the compression flange and the middle of the tension flange to yield before the remainder of the flanges, were included. As these portions of the flanges yield, the effective modulus and the overall stiffness of the section was reduced. As portions of the flanges yield, the remaining portions provide the resistance to inelastic lateral-torsional buckling. The investigation showed that yielding of the web was not a significant factor in the lateral-torsional buckling.

Kitipornchai and Trahair (1980) analytically investigated lateral-torsional buckling of singly-symmetric beams. Most design specifications treat all cross-sections as doubly-symmetric, an assumption that can be conservative or unconservative. The calculation for β_x to account for a single axis of symmetry can be complicated. Kitipornchai and Trahair (1980) related a simplified β_x to the ratio of I_{yc} over I_y. Kitipornchai and Trahair (1980) determined that the use of singly-symmetric properties allowed for more accurate determination of the lateral-torsional buckling resistance.

Kubo and Fukumoto (1988) investigated the interaction of local and lateral-torsional buckling in the inelastic range in doubly-symmetric welded girders. A girder can fail by local flange buckling, or lateral-torsional buckling, or in a combined mode of buckling. Kubo and Fukumoto (1988) performed three-point bending tests on beams with varying slenderness ratios and spans. Many of the beams had slenderness ratios similar to those of bridge I-girders during the construction stage. The ultimate load capacity and slenderness ratios of the tested beams were compared with the predicted capacities. In order to improve the prediction of the buckling capacity of slender flange beams, the buckling equation from the European Convention for Constructional Steelwork was modified to account for the interaction of local and lateral-torsional buckling.

2.4.4 Improved Lateral-Torsional Buckling Behavior

Szewczak, et. al (1983) performed a finite element investigation of different types of stiffeners for beams. The four types of stiffeners were transverse stiffeners, batten plates, box stiffeners, and cross stiffeners. The stiffeners were used on pin-ended, fix-ended, and cantilever beams. Szewczak, et. al (1983) examined the reduction of normal warping stresses and twisting provided by the stiffeners. The transverse stiffeners did not increase the torsional resistance of the beams, and the batten plates achieved a modest increase in the resistance. The box and cross stiffeners significantly reduced the warping normal stresses and twisting of the beams. Szewczak, et. al (1983) provided recommendations on the placement and size of the various stiffeners to maximize the resistance to the warping normal stresses and twisting.

Takabatake (1988) investigated the increase in the St. Venant torsional resistance and weak axis moment of inertia provided by transverse stiffeners and batten plates. The increase provided by the stiffeners was analytically determined, and incorporated into the lateral-torsional buckling moment calculation. Takabatake (1988) investigated beams loaded under

constant moment and varying moment produced by concentrated loads. The support conditions were either pinned or fixed. Takabatake (1988) determined that the effect of the increase in the weak axis moment of inertia was negligible for both types of stiffeners, but that the increase in the torsional resistance could substantially increase the lateral-torsional buckling load. Takabatake, et. al (1991) performed tests to verify the findings of Takabatake (1988). A correction factor was incorporated when the experiment results did not match the predicted increases for the torsional resistance.

Helwig and Frank (1995) analyzed the ability of stay-in-place metal deck forms (SIP forms) to improve the construction stage lateral-torsional buckling behavior of steel bridge girders. The buckling resistance is improved through the shear rigidity of the SIP forms. The SIP forms are typically installed before the concrete deck is placed. While the stability provided by metal deck forms is not considered in the AASHTO LRFD (1994) design specifications, the shear rigidity of SIP forms could be used to increase the lateral-torsional buckling resistance of I-girders during the construction stage.

2.5 Prototype Bridges Used in Thesis

Two prototype bridges were used in this thesis to design and analyze innovative lateral bracing concepts for HPS I-girder bridges. Both were simply supported, single span bridges. The first bridge is based on an actual bridge used in previous research (Czaplicki, 1996). The span is 33.5 m (110 ft). The second bridge has a span of 50 m (164 ft) and is not an actual bridge. The second bridge was created to investigate the effect of a longer span length on proposed lateral bracing concepts and has the same dimensions as the first bridge whenever possible. Figure 2.7 shows the span lengths and standard diaphragm spacing for the two prototype bridges used in this thesis. The transverse girder spacing of 3.92 m (12.86 ft) from the original 33.5 m bridge design was kept for both bridges. Also in this thesis, 485 MPa and

690 MPa (70 ksi and 100 ksi, respectively) yield strength steels were used in the design of girders for these bridges.

Skew of the prototype bridges was not considered. All of the diaphragms were assumed to be perpendicular to the girders. The superelevation of the roadway was also neglected. The deck was assumed to be approximately 229 mm (9 in) thick.

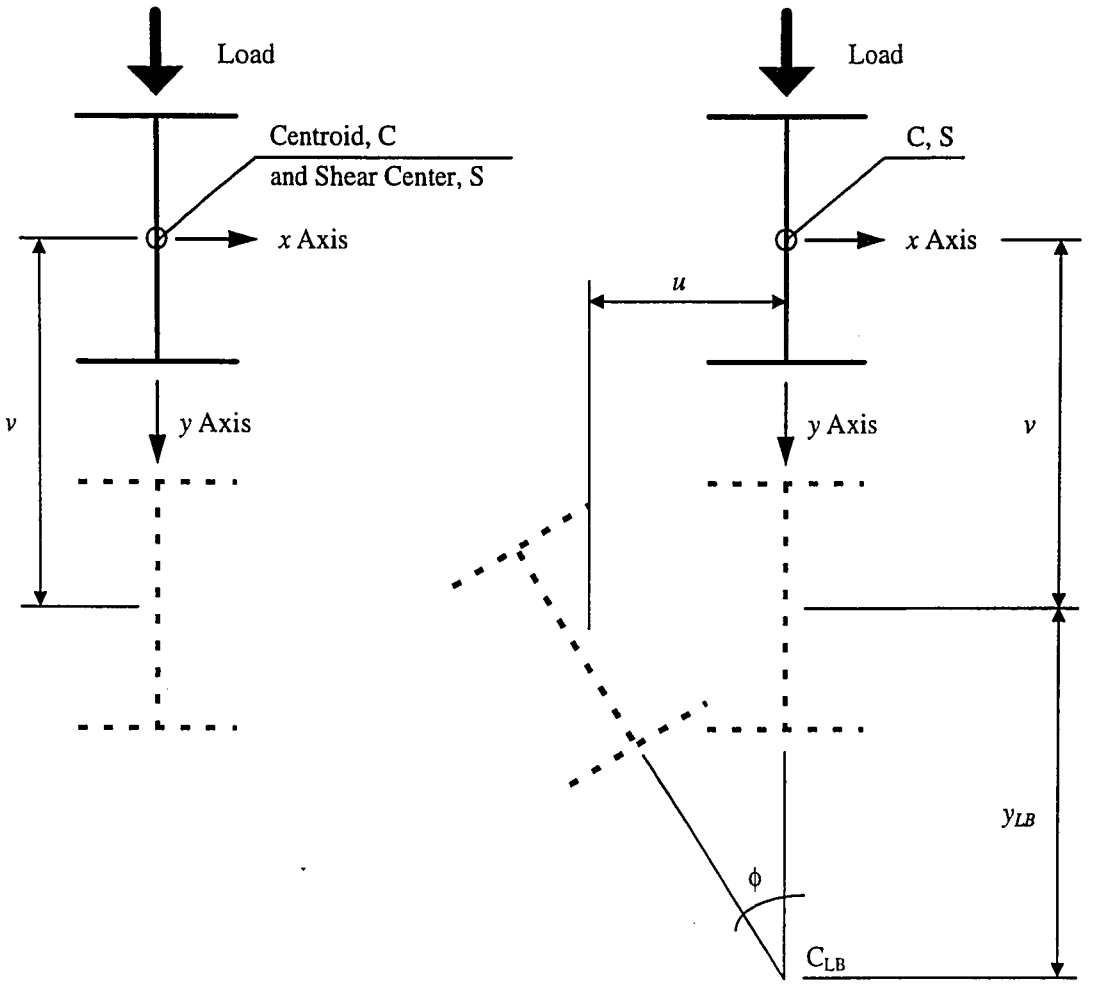

(a) In-plane Deflections (b) In-plane and Out-of-plane Deflections

Figure 2.1 Deflections caused by load (after Galambos (1968))

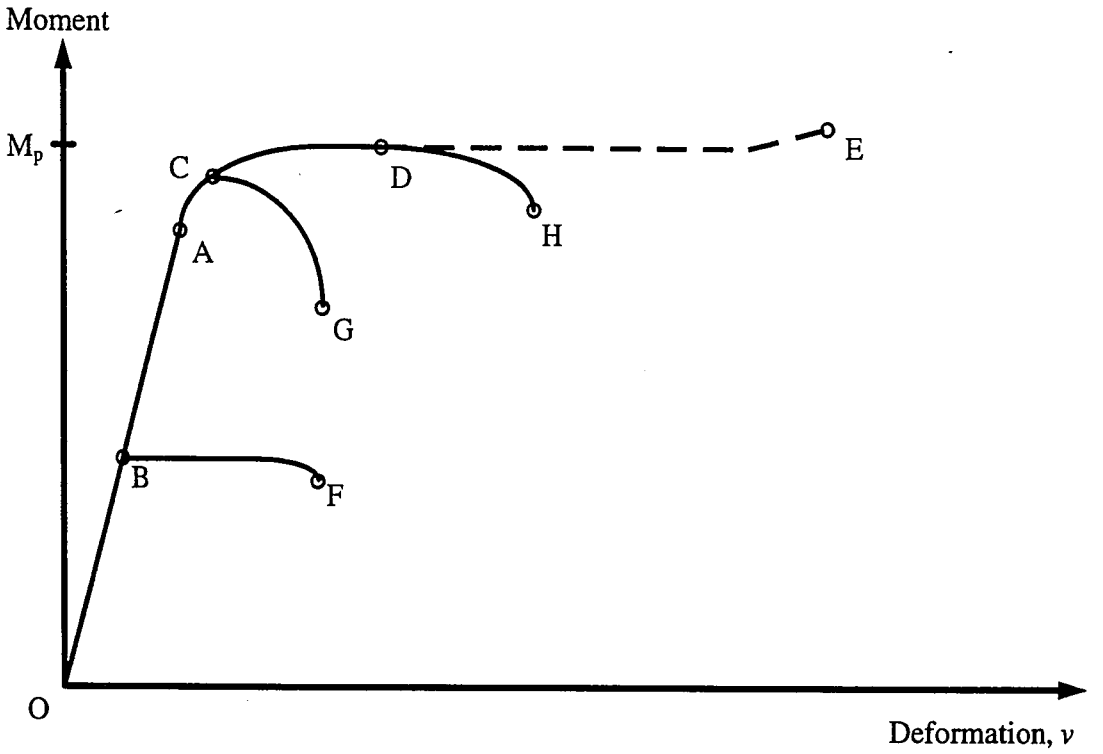

Figure 2.2 Load-deflection curves for beams (after Galambos (1968))

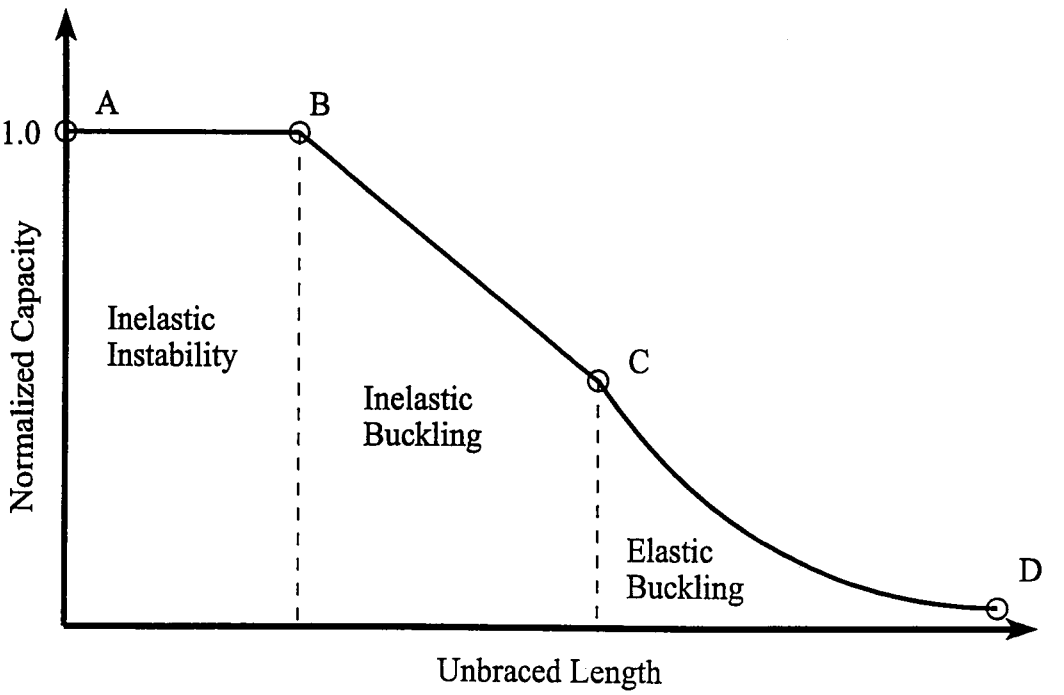

Figure 2.3 Normalized lateral-torsional buckling moment capacity versus unbraced length

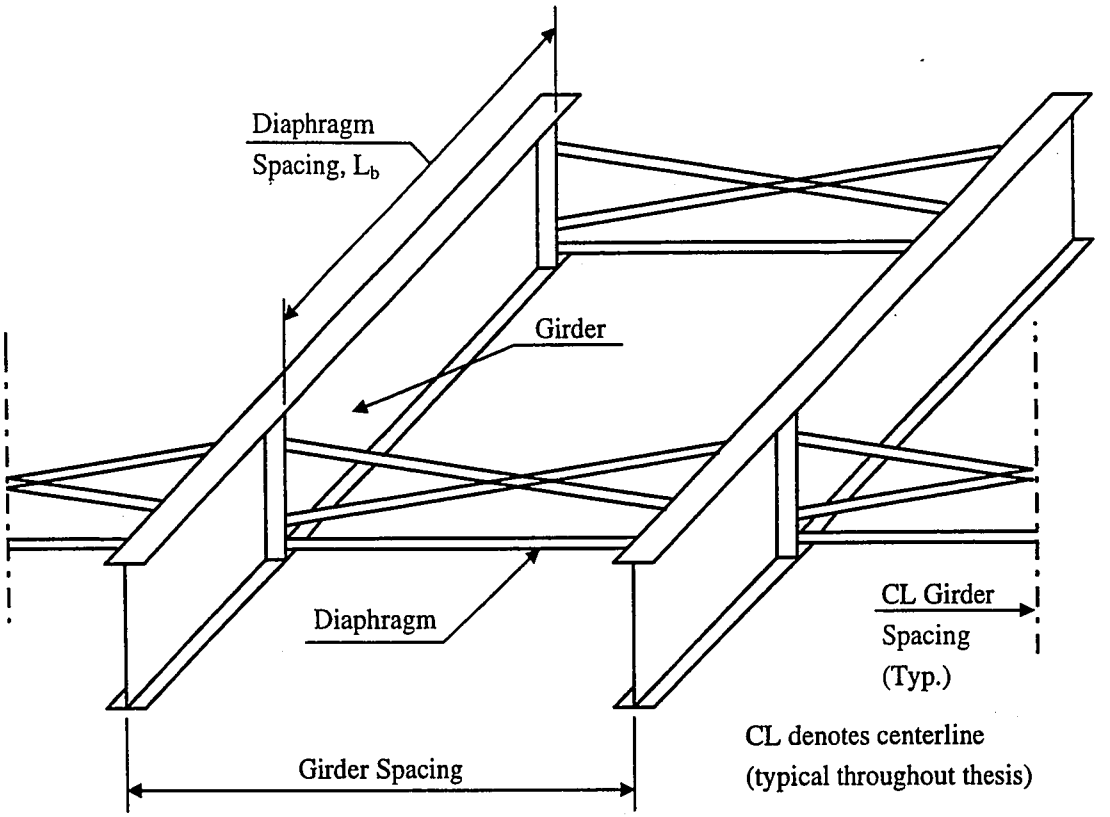

Figure 2.4 Isometric view of typical girder arrangement

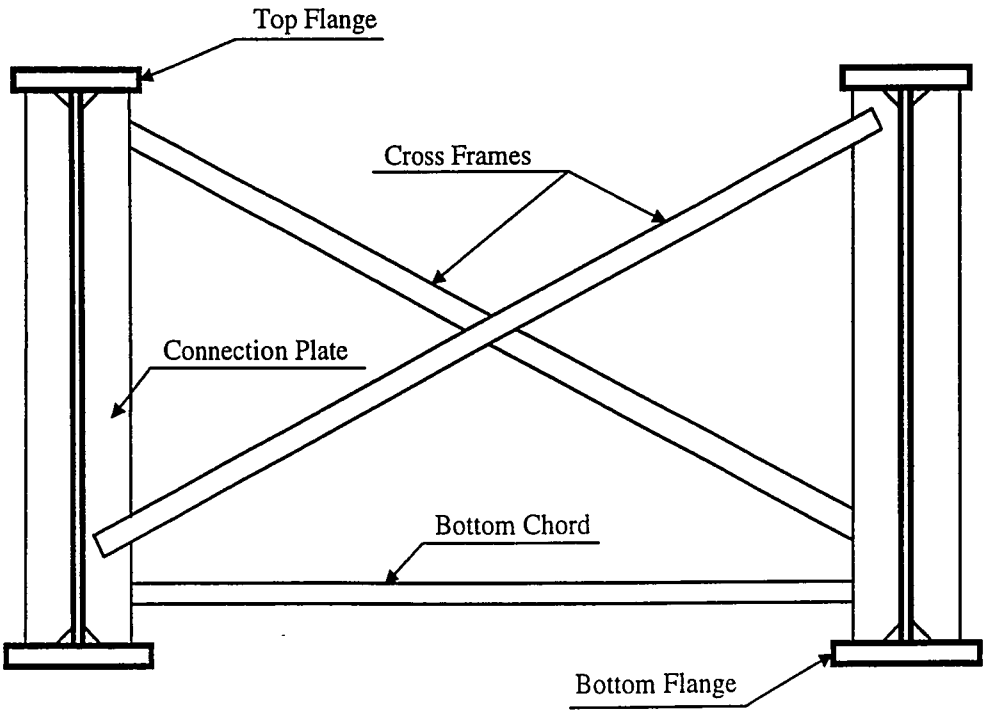

Figure 2.5 Typical diaphragm details

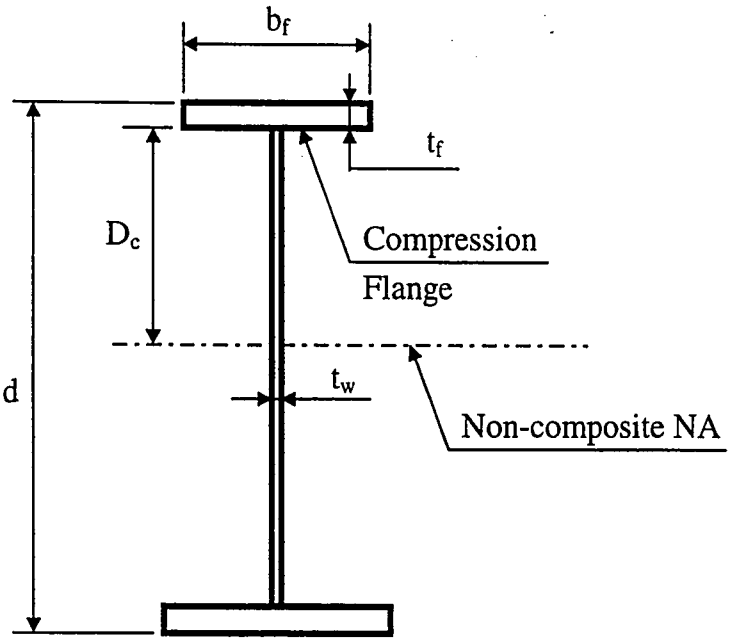

Figure 2.6 AASHTO terminology for cross-sections

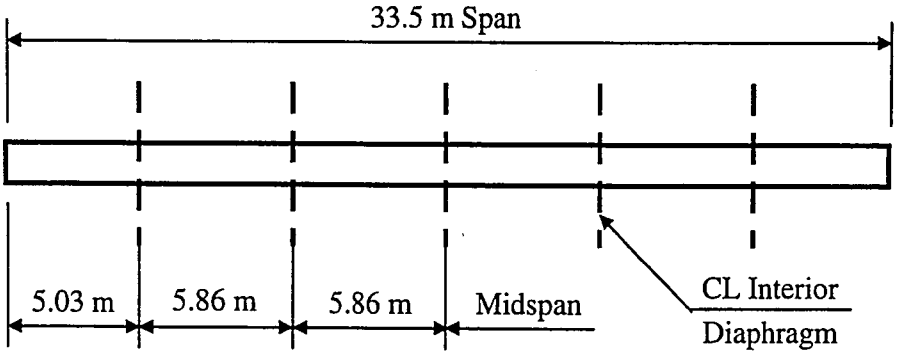

(a) 33.5 m span length

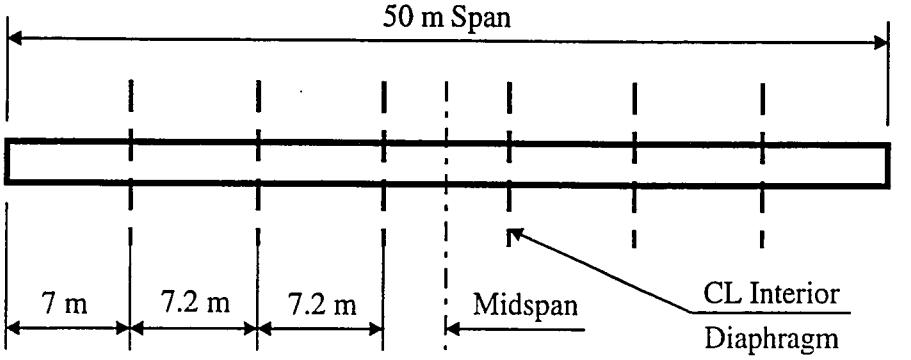

(b) 50 m span length

Figure 2.7 Span and unbraced lengths used in thesis

3. Bridge Girder Design Concepts

3.1 Introduction

Several bridge girder design concepts are discussed in this chapter. The design concepts, which are focused on the bracing of girders against lateral-torsional buckling, are the flange rotational restraint brace, the use of batten plates, and the pairing of girders. The flange rotational restraint brace allows an increase in the spacing of diaphragms (lateral bracing) without compromising the stability of the girders. The batten plates are used to increase the torsional resistance of the girder, reducing the need for bracing. The pairing of girders allows the number of diaphragms to be reduced and allows the fabrication and erection effort for the bridge superstructure to be reduced. The first and third design concepts are applicable to short and medium span I-girder bridges (with spans between 20 m to 150 m). The second design concept, batten plates, was developed for use in the shorter spans commonly seen in buildings, but is investigated here for applicability in bridges.

3.2 Flange Rotational Restraint Brace Concept

3.2.1 Description

The flange rotational restraint brace (FRRB) is an innovative concept for bracing welded plate girders that provides increased lateral support of the bridge girder compression flanges. The FRRB is attached to the compression flange of the girder at the location of a standard diaphragm (i.e., at the location of a standard girder lateral brace). It restrains the in-plane rotation of the compression flange and improves the lateral-torsional buckling behavior of the girder.

The FRRB consists of a plate or T-beam rigidly attached to the compression flange of the bridge girder, as shown in Figure 3.1. A standard diaphragm is located below the FRRB to brace the entire girder cross-section. However, the spacing of the diaphragms can be increased

because the FRRB improves the lateral-torsional buckling behavior of the girders. Figure 3.1 is a modification of Figure 2.4, which includes the FRRB and modified diaphragm connections to allow the attachment of the FRRB.

Figure 3.2 shows an isometric view of a segment of two girders braced with the FRRB concept. The unbraced length between the diaphragms with the FRRB is greater than the unbraced length using standard diaphragms. In both Figures 3.1 and 3.2, the diaphragm and FRRB are shown between only two girders, to coincide with the girder pair concept, discussed in Section 3.4. Diaphragms, FRRBs, and diaphragm connection plates are not shown between the two girders and the adjacent girders as shown previously in Figures 2.4 and 2.5.

The primary advantage of the FRRB is the possibility of increasing diaphragm spacing without decreasing the lateral-torsional buckling moment capacity of the bridge girders. Many benefits can be obtained by increasing the diaphragm spacing. The diaphragms and the diaphragm connections are expensive (Huzzard, 1996). The weld between the girder flange and the diaphragm connection plate is a category C fatigue detail which can control the fatigue design of I-girders. With fewer diaphragms, the connection plates can be moved to lower stress locations, and the fatigue performance of the girder can be improved. Alternately, if the diaphragm is still located at a high stress location, less economical details with better fatigue resistance can be used effectively, because there are fewer diaphragms.

3.2.2 Behavior

The FRRB improves the lateral-torsional buckling behavior of the girder by restraining the in-plane rotation of the girder compression flange. Here, in-plane refers to the plane of the flange. In positive moment regions of a bridge girder, the top flange of the girder is in compression and is subject to lateral-torsional buckling. In positive moment regions of composite girders, the top (compression) flange is often light weight because the bridge deck is

used to resist compression stresses due to bending under service conditions. After the deck cures, the top flange is continuously braced, and lateral-torsional buckling is not a concern in positive moment regions. However, lateral-torsional buckling behavior of the girder is often a critical limit state during construction of the bridge, before the light weight compression flange is composite with the deck. Traditional methods to improve the lateral-torsional buckling behavior of beams, such as stiffeners, batten plates, and cross-stiffeners, stiffen the web and improve the torsional resistance of the beam. However, these methods do not improve the lateral-torsional buckling behavior of bridge girders where the torsional resistance of the girder is small, and may be ignored due to the high web slenderness.

The FRRB behaves as a rotational spring which restrains the rotation of the flange in its plane. As the flange of the girder rotates in-plane at the location of the FRRB, the FRRB resists the rotation. The FRRB must have sufficient stiffness to produce an increase in the lateral-torsional buckling capacity.

Figure 3.3 compares the lateral deflected shapes of girders with standard diaphragms and with diaphragms with FRRBs. In Figure 3.3(a), the lateral deflected shape of a buckled compression flange of a girder with a standard diaphragm (brace) is shown. Over the unbraced length, the compression flange deflects as if the brace provides only a pinned support. Furthermore, Figure 3.3(a) assumes that the adjacent unbraced lengths are also buckled in the pinned-support shape, and that the adjacent unbraced lengths do not support the unbraced length shown in the figure. The girder with the FRRBs (Figure 3.3(b)) has less rotation at the diaphragm location due to the rotational restraint. The lateral deflection with the FRRBs takes on a shape with curvature reversals as shown in Figure 3.3(b).

The rigid connection between the FRRB and the compression flange allows the FRRB and the flange to act in a manner similar to the beams and columns, respectively, of a braced

frame with rigid connections. The compression flange behaves similar to a column in compression (SSRC, 1988), and the FRRB behaves as the beams of the frame, restraining the columns. The rotational restraint reduces the effective unbraced length of the compression flange between the braces, and the lateral-torsional buckling resistance is increased. The effect of the FRRBs can be quantified by an effective length factor. An unbraced length with pinned-pinned condition has an effective length factor, termed K, equal to 1.0. The effective length factor for the fixed-fixed condition is K equal to 0.5. The use of the effective length factor allows the brace spacing to be significantly increased. In the midspan region of the bridge girder, the diaphragm spacing can be increased approximately 50%, because K factors of approximately 0.65 are readily attainable using FRRBs.

3.3 Batten Plate Concept

3.3.1 Description and Behavior

A beam with stiffeners and batten plates has higher lateral-torsional buckling moment capacities than the same beam without stiffeners and batten plates. Takabatake (1988) states that the increase in the capacity is due to considering the effect of local increases of the torsional constant and the weak axis moment of inertia at the location of the attachments.

Figure 3.4 shows the elevation of a beam with the location of batten plates and stiffeners using the notation of Takabatake (1988). The distance z_{si} is the length from the end of the beam to the centerline of an arbitrary transverse stiffener i. Similarly, the distance z_{pi} is the length from the end of the beam to the centerline of an arbitrary batten plate i. The thickness of the stiffener is t_s while the width of the batten plate is b_p as shown in the figure. Although only one stiffener and batten plate are shown in the figure, any number of stiffeners or batten plates can be utilized. Figure 3.5 shows cross-sections at the locations of the transverse stiffeners and the batten plates. In each case, the stiffeners or batten plates are assumed to be on both sides of

the web. The width of the stiffener is b_s while the thickness of the batten plate is t_p as shown in the Figure 3.5.

Takabatake (1988) assumed the following: (1) the beam is a doubly symmetric, uniform I-shaped beam, (2) lateral buckling is elastic buckling, and (3) the beam has negligible in-plane distortion, initial imperfections, and residual stresses. While these assumptions simplify the calculation of the critical lateral-torsional buckling moment, the third assumption significantly constrains the applicability of the proposed method. Most I-shaped beams have significant residual stresses.

The effect of the local increase in the torsional constant and the weak axis moment of inertia provided by each stiffener and batten plate is determined using the Dirac function in series (Takabatake, 1988). The Dirac function enables the instantaneous change in the torsional constant and the weak axis moment of inertia to be determined. An energy method is used in conjunction with the assumptions listed above to develop the following relationships for the modified weak axis moment of inertia, I_{y1}, and the torsional constant, J_1:

$$I_{y1} = I_{y0} + \frac{2}{L}\sum_{i=1}^{s} I_{ys} t_s \sin^2\left(\frac{z_{si}\pi}{L}\right) + \frac{2}{L}\sum_{i=1}^{p} I_{yp} b_p \sin^2\left(\frac{z_{pi}\pi}{L}\right) \qquad \text{(Eq. 3.1)}$$

$$J_1 = J_0 + \frac{2}{L}\sum_{i=1}^{s} J_s t_s \cos^2\left(\frac{z_{si}\pi}{L}\right) + \frac{2}{L}\sum_{i=1}^{p} J_p b_p \cos^2\left(\frac{z_{pi}\pi}{L}\right) \qquad \text{(Eq. 3.2)}$$

where I_{y0} is the weak axis moment of inertia and J_0 is torsional constant of the unmodified beam, L is the unbraced length, I_{ys} and I_{yp} are the increases to the moment of inertia due to the stiffeners and the batten plates, respectively, and J_s and J_p are the increases to the torsional constant due to the stiffeners and the batten plates, respectively.

The critical moment for the modified beam is determined by using the increased torsional constant and weak axis moment of inertia in the standard elastic lateral-torsional

buckling equation. However, Takabatake (1988) states that the increase in the weak axis moment of inertia is negligible. Using the modified torsional constant and the unmodified weak axis moment of inertia yields the following critical moment for lateral-torsional buckling:

$$M_{cr} = \frac{\pi}{L}\sqrt{EI_y\left[GJ_1 + EI_\omega\left(\frac{\pi}{L}\right)^2\right]} \qquad \text{(Eq. 3.3)}$$

Takabatake, et. al (1991) performed experiments on 14 beams to verify the validity of Equations 3.1 and 3.2. While the beams with stiffeners and batten plates performed better than those without them, the results did not compare well with the predicted results. Takabatake, et. al (1991) reconciled the differences in the results by applying a correction factor, κ, to the torsional constant. The correction factor, κ, accounts for the effect of the location of the stiffener on the torsional constant. The correction factor has different coefficients for transverse stiffeners versus batten plates. For batten plates, the correction factor depends on z_{pi}. For z_{pi} between zero and $L/2$:

$$\kappa(z) = 10.250\left(\frac{z}{L}\right)^2 - 4.342\left(\frac{z}{L}\right) + 0.608 \qquad \text{(Eq. 3.4)}$$

For z_{pi} between $L/2$ and L:

$$\kappa(z) = 10.250\left(\frac{z}{L}\right)^2 - 16.158\left(\frac{z}{L}\right) + 6.517 \qquad \text{(Eq. 3.5)}$$

The effect of κ is to reduce the increase of the torsional constant. The modified formulation for the increased torsional constant has κ inside the appropriate summation as follows:

$$J_1 = J_0 + \frac{2}{L}\sum_{i=1}^{s} J_s\kappa(z_{si})t_s\cos^2\left(\frac{z_{si}\pi}{L}\right) + \frac{2}{L}\sum_{i=1}^{p} J_p\kappa(z_{pi})b_p\cos^2\left(\frac{z_{pi}\pi}{L}\right) \qquad \text{(Eq. 3.6)}$$

The correction factor κ introduced by Takabatake, et. al (1991) to account for differences between the experimental results and the theoretical results is based on a limited number of tests. Hence the correction factored has only limited applicability.

In contrast to the theoretical approach taken by Takabatake (1988), Szewczak, et. al (1983) considered the effect of stiffeners in terms of the flexural and torsional stresses. Torsional loads create pure torsional, warping shear, and warping normal stresses in addition to the typical normal and shear stresses. Szewczak, et. al (1983) performed finite element analyses to determine the extent of torsional stiffening provided by several different stiffener configurations. Szewczak, et. al (1983) concluded that the contribution of stiffeners depends not only on the type and location of the stiffeners but also on the torsional supports of the beam. The stiffeners can increase the torsional stresses under some support conditions and stiffener arrangements. For multiple stiffeners, Szewczak, et. al (1983) report that the reduction in the stresses can be significant if the location is at the quarter points for pinned torsional restraints. Szewczak, et. al (1983) conclude that transverse stiffeners are ineffective in reducing torsional stresses while batten plates exhibit some ability to reduce torsional effects.

3.3.2 Finite Element Analysis

Takabatake, et. al (1991) and Szewczak, et. al (1983) performed studies on the effect of stiffeners on the lateral-torsional behavior of beams with dimension proportions typical of building frames. The method developed by Takabatake (1988) allows for the consideration of numerous stiffeners as might be required for bridge girders. Finite element analyses were performed to determine if batten plates can improve the lateral-torsional buckling behavior of bridge girders. A commercial finite element package was utilized for elastic lateral-torsional buckling analyses of girders with batten plates.

The 33.5 m bridge mentioned in Section 2.4 was used as the test span in the finite element analyses. Due to the symmetry of the girder and the loading conditions, only one half of the bridge was modeled. Figure 3.6 shows the cross-section dimensions of the singly-symmetric girder used in the buckling analysis. The depth dimension is the center-to-center distance between the top and bottom flanges. Each batten plate is 1325 mm (52.2 in) high by 670 mm (26.4 in) wide. The thickness of each batten plate is 20 mm (0.79 in).

Figure 3.7 depicts the simplified stress-strain relationship for the steel used in the finite element model. The elastic modulus, E, is 200,000 MPa (29,000 ksi), and the Poisson's ratio, ν, is 0.295. The yield strength, F_y, is 485 MPa (70 ksi), and the ultimate strength, F_u, is 690 MPa (100 ksi).

The half-span model was divided into 100 evenly spaced elements lengthwise. The length of all elements was 167.5 mm (6.59 inches). The flange elements were all 87.5 mm (3.44 inches) wide; four elements were used across the total width of the flange, to allow residual stresses to be included in the model. The residual stresses are discussed further in Chapter 4. Six elements were used across the depth of the web. The width of the web elements depended on their proximity to the flanges. The web elements attached to the flanges had the smallest width. The web elements near the center of the web were the widest. Each batten plate was composed of four columns of elements with the same dimension as those used in the web. Eight noded thick shell elements were used for each element. The transverse shear strain can be determined along with the membrane and bending strains in the thick shell elements.

In order to judge the effect of the batten plates, several configurations of batten plates were developed. Figure 3.8 shows the locations of the batten plates in the configurations. The numbers indicate the number of nodes from the batten plate centerline to the midspan. Each

batten plate location has one batten plate on each side of the web. The nomenclature for the configurations is as follows:

(1) B-0: no batten plates in each half-span and bracing at the end,
(2) B-2: 2 batten plates in each half-span and bracing at the end,
(3) BB-2: 2 batten plates in each half-span and bracing at midspan and end,
(4) B-4: 4 batten plates in each half-span and bracing at the end,
(5) B-4A: same as B-4 but with a different spacing,
(6) B-6: 6 batten plates in each half-span and bracing at the end, and
(7) B-12: 12 batten plates in each half-span and bracing at the end.

Boundary conditions were used to impose symmetry about the midspan cross-section. Also, boundary conditions modeled the support and bracing at the end of the girder. Figure 3.9 shows the cross-section of the model at the midspan. Points A, B and C all lie along the y axis of the beam; point A is in the top flange, point B is in the web and point C is in the bottom flange. Points A' and C' are points in flanges away from the axis. The z axis is the longitudinal axis of the beam. Table 3.1 lists the boundary conditions for each point at the midspan. The deflections of the midspan cross-section are controlled through point A. The web is not permitted to distort at this cross-section so points B and C are rigidly constrained to point A. The boundary conditions are required by the symmetry conditions at midspan. Figure 3.10 shows a cross-section of the model at the support end. The points are defined in the same way as for Figure 3.9. The fixed boundary below the bottom flange prevents y axis deflection. Also, x axis deflection and z axis rotation (twist) are not permitted. Table 3.2 lists the boundary conditions for each point at the support end. The boundary conditions are controlled through point C. The web is not permitted to distort at this cross-section. Thus, the points on the web are rigidly constrained to point C. As a result of this constraint, lateral deflection and twist of the cross-section are not permitted.

The top flange of the girder was loaded with a uniform unit pressure along its length. The buckling loads and modes were determined using an eigenvalue analysis. Table 3.3 lists the flange pressure required to cause the girder model to laterally buckle. The critical moment is the maximum moment due to a uniform load based on the flange pressure times the top flange width. The critical moment labeled as Takabatake Method was determined using Equations 3.1, 3.3, and 3.6. As shown in Table 3.3, the method developed by Takabatake (1988) does not provide reasonable results for this girder. Furthermore, the results in Table 3.3 show that a large number of batten plates are needed to provide even a modest increase in the critical moment (i.e., the lateral-torsional buckling moment capacity).

3.4 Pairs of Girders

3.4.1 Description

The FRRB has the potential to reduce the number of diaphragms and corresponding attachments to the girder by increasing the distance between diaphragms (i.e., the unbraced length). To further reduce the number of attachments, the girders of the bridge can be fabricated and erected as pairs of girders. A girder pair is composed of two welded plate girders connected by diaphragms along the length of the girder. The girder pair can be fabricated in the shop and transported to the field as a unit. Alternately, the installation of the diaphragms can be completed in the field. After erection, the girder pair would not be connected to other girder pairs in the bridge by diaphragms. The use of girder pairs could reduce erection time, the number of diaphragms, and the number of diaphragm connections. Redundancy in the bridge is provided by the concrete deck and the diaphragms of the girder pair.

Figure 3.11 compares framing plans for hypothetical superstructures using (a) standard diaphragms and (b) girder pairs with diaphragms with FRRBs. The number of diaphragms and corresponding attachments is reduced significantly using girder pairs with FRRBs.

3.4.2 Benefits and Concerns

By reducing the number of diaphragms and corresponding attachments to each girder, the economics of the bridge can be improved. Fewer attachments can also improve the fatigue life of each girder. If the girder pair is fabricated entirely in the shop, better quality fabrication and assembly can occur. Typical steel bridges are erected with an initial pair of girders and then individual girders are framed into the system. This requires attachment of the diaphragms to each girder during erection. With the girder pairs, each pair can be erected independently. Without the attachment of diaphragms during girder erection, the erection and inspection process is improved in several ways. For instance, the proper tightening of the diaphragm connection bolts during erection would no longer be a concern as the diaphragm connections would be completed before erection. Each girder pair is a stable unit.

The redundancy of the bridge is a concern. However, redundancy is not significantly reduced by using girder pairs. Each girder is attached to a second girder and therefore load can be transferred through the secondary members, the diaphragms, and FRRBs. The concrete deck can distribute loads to each girder and between the girder pairs.

The girder pair concept generates a second concern. The second concern is that the system needs to be able to incorporate the grading of the roadway. If the girders are level in each pair, one of the girders would have a large deck haunch. Alternately, if the diaphragm is inclined to follow the grading, it may complicate the design, fabrication, transportation, and erection of a girder pair. Also, the girder pair concept may not be useful for bridges where the diaphragms are primary members, such as horizontally curved bridges.

3.5 Summary

Three bridge girder design concepts were discussed in this chapter. The FRRB design concept has the potential to increase the unbraced length (diaphragm spacing) for bridge girders.

Subsequent chapters discuss means to analyze the effectiveness of FRRBs to improve the lateral-torsional buckling moment. The batten plate concept can increase the torsional resistance of the cross-section. It was found that the effect of the batten plates did not substantially reduce the need for bracing. The girder pairs can be used with or without the FRRB design concept to increase the economy of an I-girder bridge.

Table 3.1 Boundary conditions at midspan of finite element models

DOF	Location				
	A	A'	B	C	C'
Δx	free	free	rigid constraint to point A	rigid constraint to point A	free
Δy	free	free	"	"	free
Δz	fixed	fixed	"	"	fixed
θx	fixed	fixed	"	"	fixed
θy	fixed	fixed	"	"	fixed
θz	free	free	"	"	free

Table 3.2 Boundary conditions at support end of finite element models

DOF	Location				
	A	A'	B	C	C'
Δx	rigid constraint to point C	free	rigid constraint to point C	fixed	free
Δy	"	free	"	fixed	fixed
Δz	"	free	"	free	free
θx	"	free	"	free	free
θy	"	free	"	free	free
θz	"	free	"	fixed	fixed

Table 3.3 Results of finite element models of girders with batten plates

Study Case	Flange Pressure (N/mm^2)	Critical Moment (kN-m)	
		Finite Element Analysis	Takabatake Method
B-0	0.0136	667	438
B-2	0.0167	821	2,029
BB-2	0.0494	2,424	6,177
B-4	0.0186	913	3,380
B-4A	0.0197	966	4,713
B-6	0.0217	1,065	5,600
B-12	0.0323	1,587	10,929

Note: To convert to ksi, 1 ksi = 6.90 N/mm^2 (MPa). To convert to kip-ft, 1 kip-ft = 1.356 kN-m

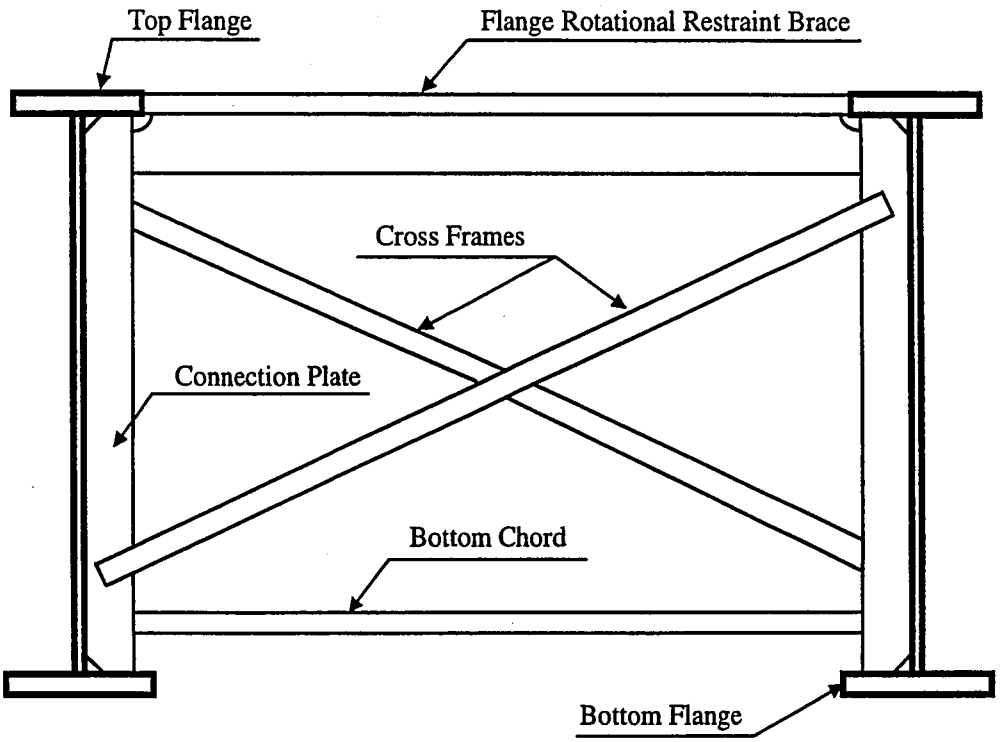

Figure 3.1 Diaphragm with flange rotational restraint brace

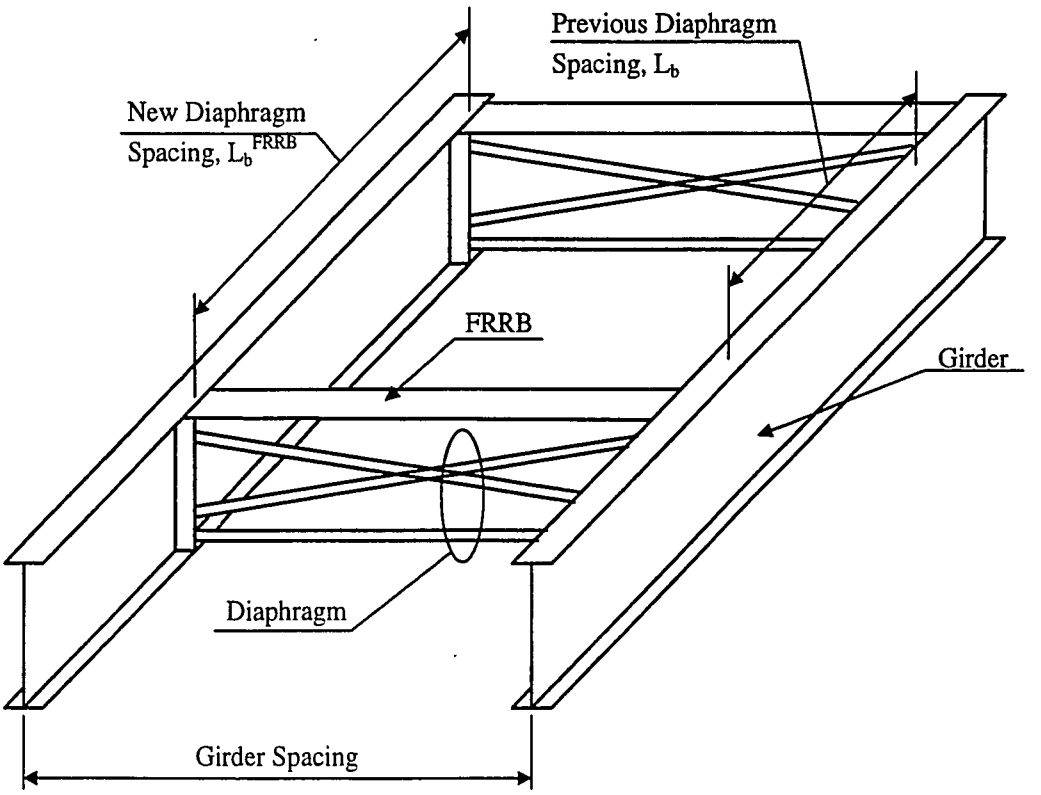

Figure 3.2 Isometric view of girder pair with FRRBs

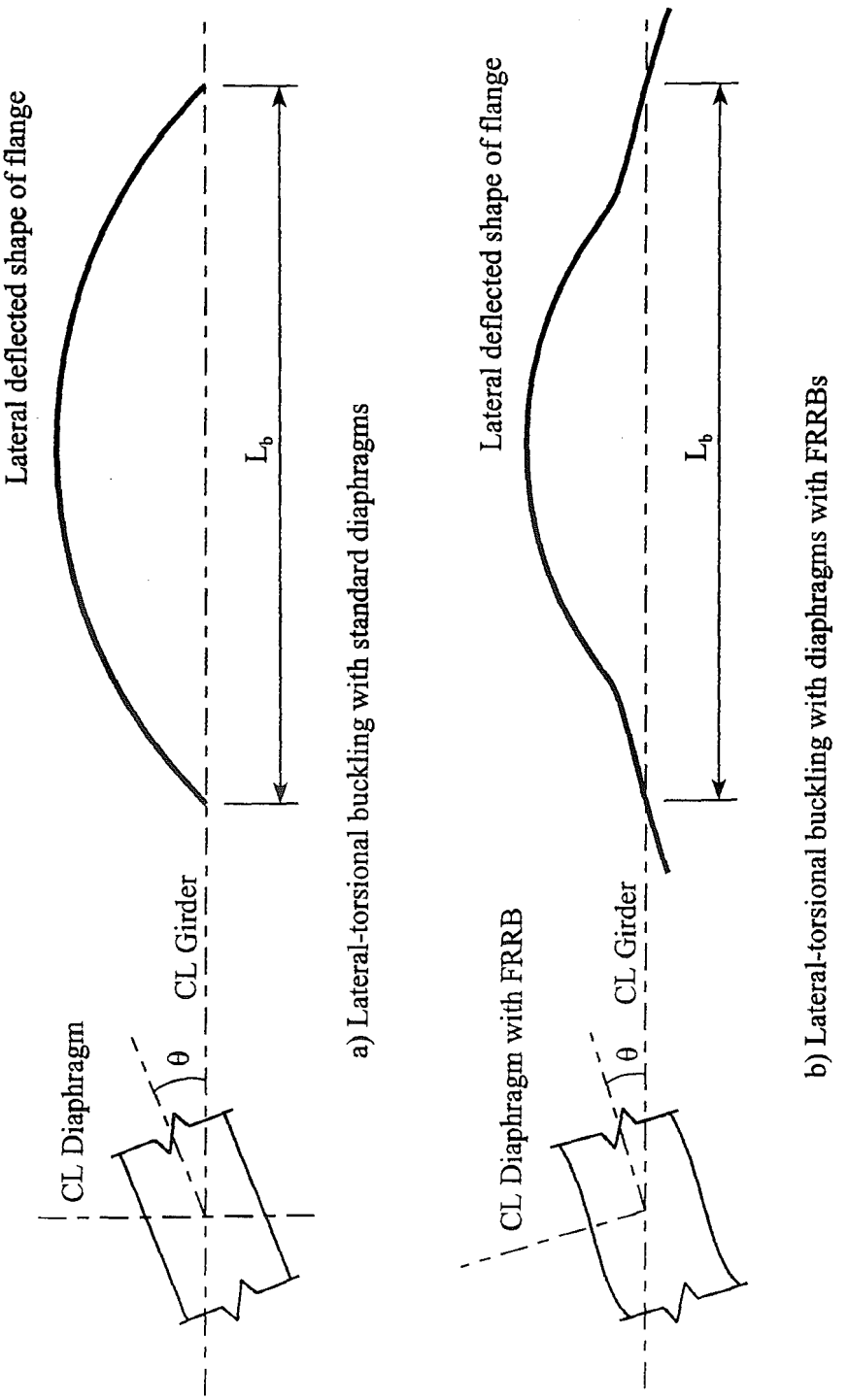

Figure 3.3 Comparison of lateral deflected shapes of compression flange

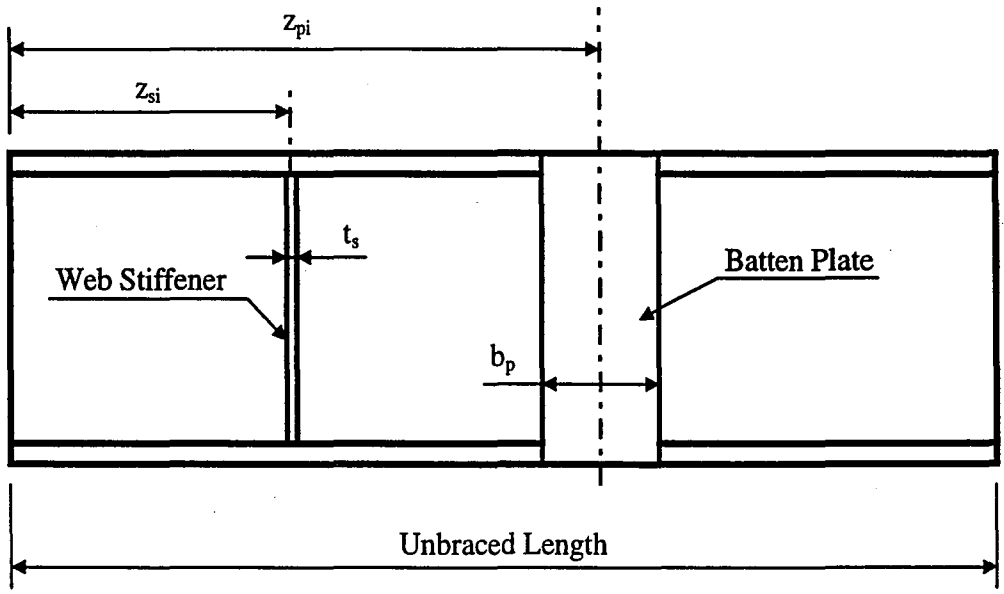

Figure 3.4 Elevation of stiffened beam (after Takabatake (1988))

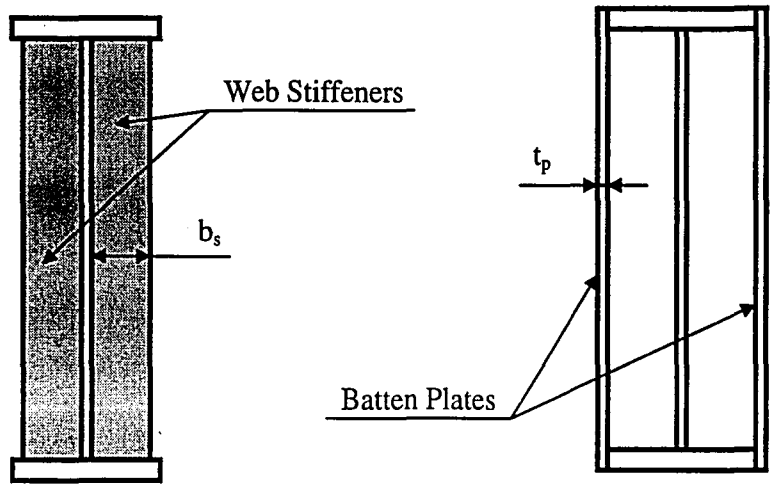

Figure 3.5 Web stiffeners and batten plates (after Takabatake (1988))

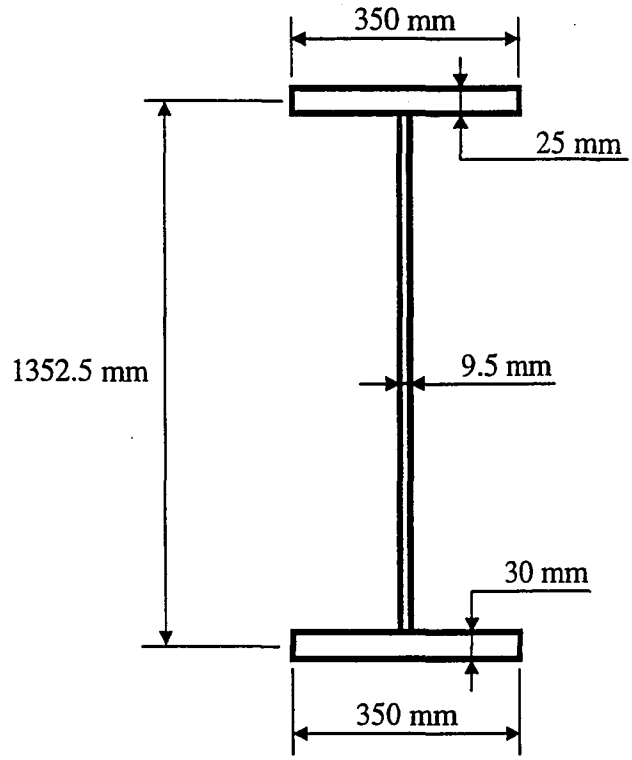

Figure 3.6 Cross-section of finite element models for girders with batten plate

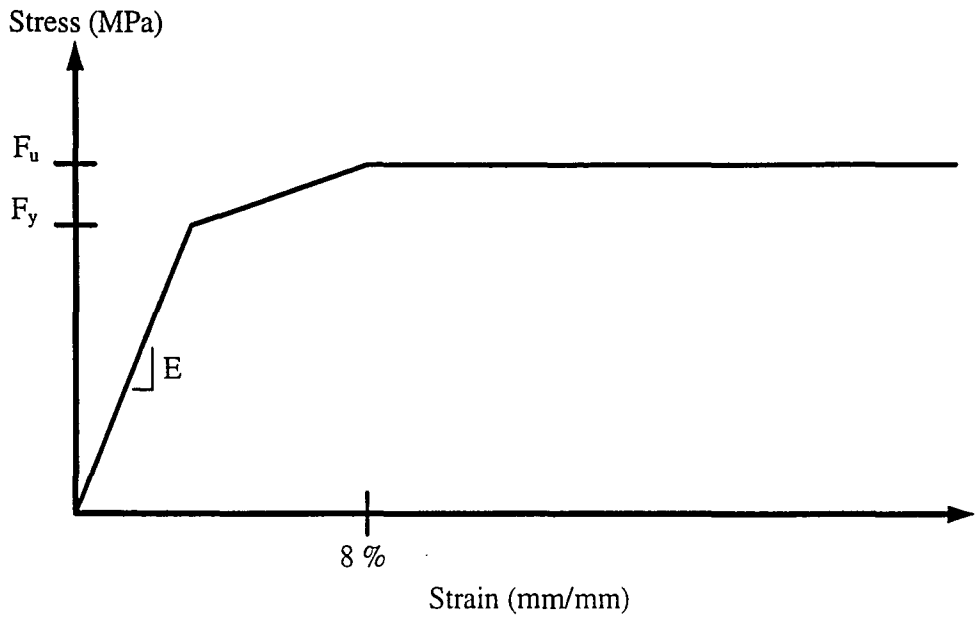

Figure 3.7 Stress-strain relationship used in finite element models

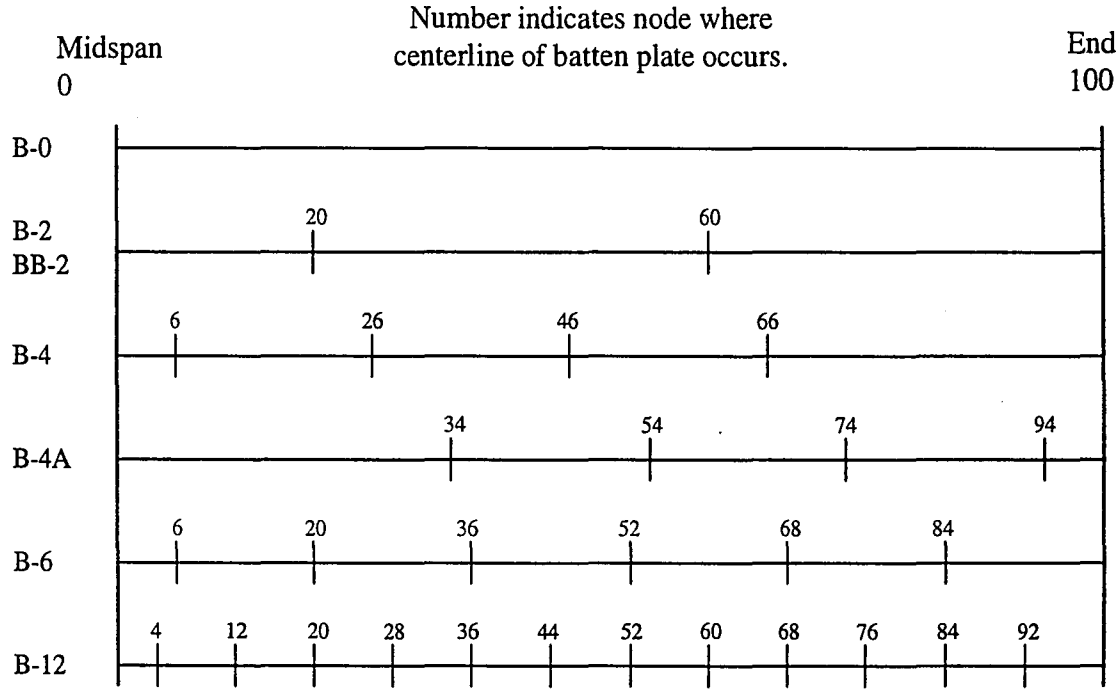

Figure 3.8 Location of batten plate centerlines in finite element models

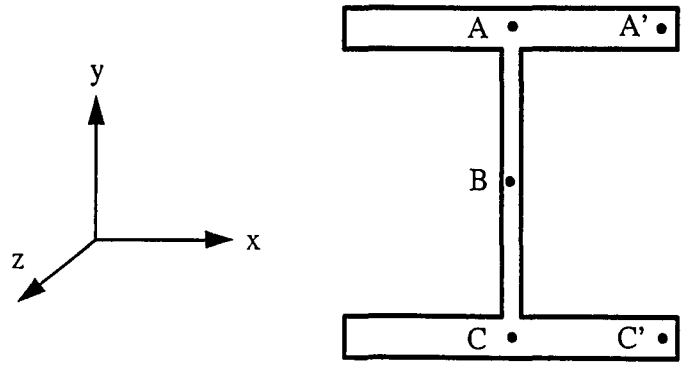

Figure 3.9 Cross-section of girder at midspan

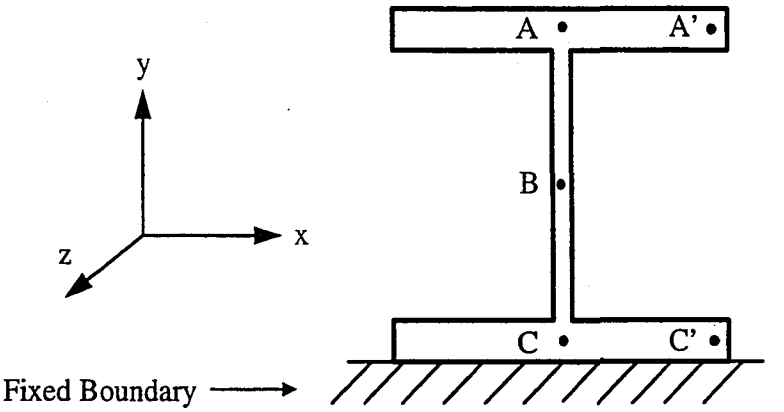

Figure 3.10 Cross-section of girder at support end

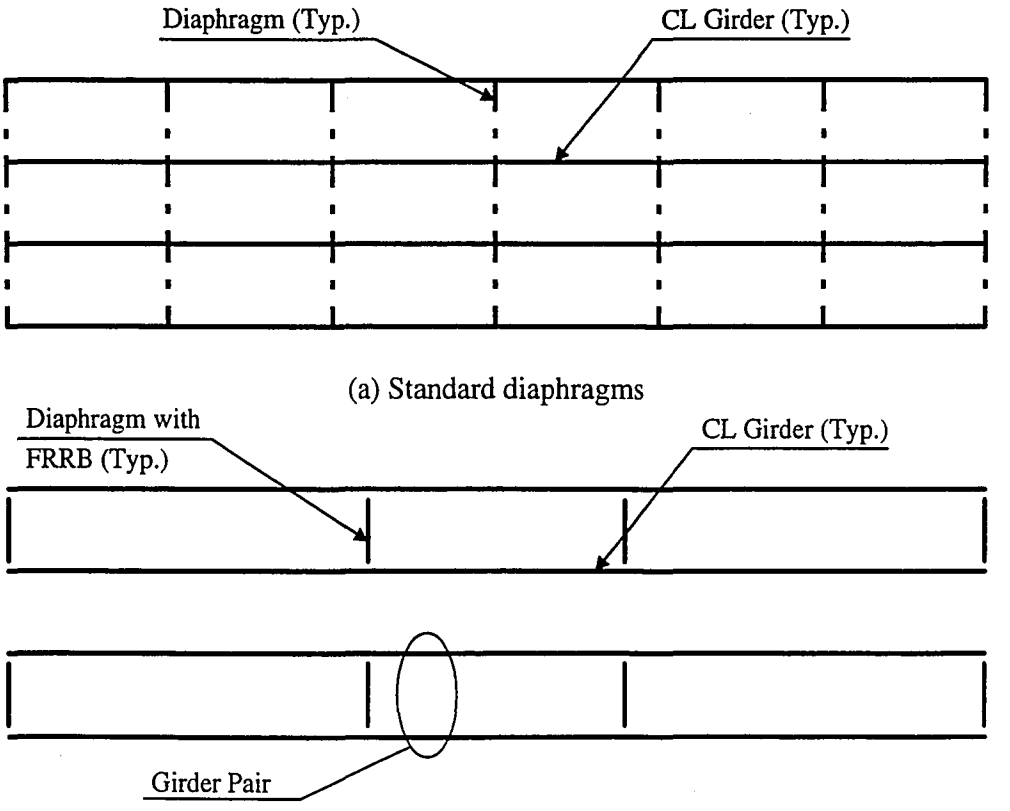

(a) Standard diaphragms

(b) Girder pair with FRRB

Figure 3.11 Comparison of framing plans

4. Finite Element Models of Lateral-Torsional Buckling Behavior

4.1 Introduction

Finite element models of inelastic lateral-torsional buckling of steel I-girders are developed and verified in this chapter. The primary purpose of developing and analyzing the models is to determine the effectiveness of the FRRB concept. A study by Kubo and Fukumoto (1988) provided examples of lateral-torsional buckling that were used to calibrate the finite element modeling approach. Then a brief study of inelastic buckling of a finite element girder model with FRRBs was conducted. The finite element models and methods of analysis developed in this chapter are the basis for the other finite element analyses presented in this thesis.

4.2 Background

Kubo and Fukumoto tested welded-plate beams to investigate the interaction of lateral-torsional and local buckling. Although the beam spans were quite short, the web slenderness ratio (h/t_w) and the lateral-torsional slenderness ratio (L_b/r_y) of the beams were close to those typical for steel bridge I-girders. The compression flange slenderness ratios for the beams in the test were higher than permitted than by the AASHTO LRFD (1994) Bridge Design Specifications without severe reductions in the moment capacity.

The beams tested by Kubo and Fukumoto (1988) had spans between 1.5 m (4.92 ft) and 3.35 m (11 ft). They tested four series of beams with different overall dimensions (overall depth by flange width):

(1) B1B - 250 mm deep by 125 mm wide,
(2) B2B - 300 mm deep by 150 mm wide,
(3) B3B - 200 mm deep by 150 mm wide, and
(4) B4B - 250 mm deep by 150 mm wide.

Table 4.1 shows the dimensions and slenderness ratios of three of the beams from the B2B series. The web and compression flange slenderness ratios, given by h/t_w and b/t_f respectively, are similar for the three specimens, but the lateral-torsional slenderness varies. B2B-C1 has a lateral-torsional slenderness ratio, given by L_b/r_y, typical for steel bridge girders. In Figure 4.1 a cross-section of the symmetric girder defines the dimensions listed in Table 4.1.

The material properties were determined for the web and flange plates for each beam series in the test. For specimen B2B-C1, the yield stress of the flange was 286 MPa (41.5 ksi). The web yield stress was 292 MPa (42.3 ksi). The average elastic modulus, Poisson's ratio, yield strength and ultimate strength values are given in Table 4.2 for all four series.

The residual stresses were measured for each test series using the sectioning method. The average value of the residual stresses measured in the series B2B was $0.33 \cdot F_y$ at the center of the flange and $0.50 \cdot F_y$ at the flange tips. The high residual stresses were attributed to the welding process. The initial out-of-straightness (geometric imperfections) was measured for the beams at five equally spaced points along the beam. The initial out-of-straightness had a mean value of $L/7{,}300$ in the strong direction of the beam (perpendicular to the major axis) and a mean value of $L/5{,}320$ in the weak direction of the beam (perpendicular to the minor axis).

The beams were simply-supported and loaded in 3 point bending. The load was applied at midspan, 25 mm (1 in) above the top flange. Bearing stiffeners were placed on both sides of the web at the point of loading. The ends of the beams were restrained against lateral deflection and twisting but were not restrained against warping. The unbraced length, L_b, was equal to the span length, L.

Figure 4.2 shows the normalized moment capacity versus midspan deflection curves for beam B2B-C1 (Kubo and Fukumoto, 1988). Beam B2B-C1 laterally buckled at an ultimate moment, M_{ult}, of 37.2 kN-m (27.4 kip-ft). The ultimate moment of B2B-C1 was approximately 58% of the yield moment, and the corresponding load, P_{ult}, was 44.4 kN (10.0 kips). In the test, the lateral deflections were measured at each flange and the vertical deflection was measured at the center of the bottom flange. Twisting of the section accompanied the lateral deflection as shown by the difference in the top and bottom flange lateral deflections in Figure 4.2. Since the web slenderness is low (and the web is stocky), the torsional resistance of the entire cross-section aids in resisting the buckling.

Figure 4.3 shows the normalized moment capacity versus longitudinal strains on the upper and lower surface of the top (compression) flange for beam B2B-C1 (Kubo and Fukumoto, 1988). The strain gages at the upper surface are ε_1 on the left flange tip of the beam and ε_2 on the right flange tip. The strain gages on the bottom surface are ε_3 on the left flange tip of the beam (beneath ε_1) and ε_4 on the right flange tip (beneath ε_2). The strains in Figure 4.3 were measured near the tips of the flange on the top and bottom surfaces.

When the strain measurements begin to show differences, strain separation is occurring. Strain separation can occur in two ways. The first type of strain separation can be seen by differences in the strains on the opposite tips of the flange. When the strains on the opposite tips of a flange separate, one tip is experiencing less compressive strain than the other tip, indicating lateral-torsional buckling. The second way is denoted by differences in strains on the same tip and on the opposite surfaces. When the strains on the upper and lower surfaces of a flange separate, one surface is experiencing less compressive strain than the other surface. This is indicative of local flange buckling. As the beam buckles, the strain at one location can go into positive strain.

For beam B2B-C1, strain separation occurs between the two flange tips (compare ε_1 and ε_2, and ε_3 and ε_4), indicating lateral-torsional buckling, followed by local buckling on one side. Clearly at the peak load, the two strains at each flange tip (ε_1 and ε_2, and ε_3 and ε_4) are the same, indicating local buckling occurs after the peak load is reached. After one mode of buckling has initiated, the beam is locally weakened and other modes of buckling can be introduced.

4.3 Finite Element Analysis

4.3.1 Introduction

Finite element analyses were performed to simulate the test of beam B2B-C1. Since Kubo and Fukumoto were investigating the interaction of local and lateral buckling, not all of the tests were of interest in the present thesis. However, test results for beam B2B-C1 allow finite element models which fail by lateral-torsional buckling to be calibrated. Also, since beam B2B-C1 had a high lateral-torsional slenderness ratio (L_b/r_y), it had proportions similar to those of a steel bridge girder.

4.3.2 Modeling of Test Specimen B2B-C1

The finite element analyses presented in this section were not intended to precisely replicate test results from Kubo and Fukumoto (1988). The analyses were conducted to calibrate a finite element analysis approach to simulate the lateral-torsional buckling behavior of girders with geometric imperfections and residual stresses. The goal of the analyses was to provide lateral-torsional buckling behavior similar to that of beam B2B-C1 as reported by Kubo and Fukumoto (1988). The finite element model was intentionally coarse to allow for easy modification, rapid computation, and a minimum of output data.

The dimensions of beam B2B-C1 were used to create the model. Due to the symmetry of the beam and the loading, only half of the span was modeled. The half span of 1675 mm was

divided into 40 equal elements with 41.875 mm lengths. Each flange was divided into four elements across the width to permit residual stress to be modeled. The flange elements were 37.625 mm wide by 41.875 mm long. The web was divided into eight elements 36.75 mm wide by 41.875 mm long. The thickness of each element was the same as the plate thickness given in Table 4.1. Eight noded thick shell elements were used for all of the elements. In thick shell elements, the transverse shear strain can be determined along with the membrane and bending strains.

The material properties used in the model differed from the data for the B2B series (Kubo, 1988). The yield strength, F_y, for the web and flanges was 290 MPa (42.1 ksi) in the model with an ultimate strength of 438 MPa (63.5 ksi). Since the yield strength was a bit higher than in the actual specimen, the yield moment of the cross-section in the model was slightly higher than the actual specimen. The Poisson's ratio was 0.28 and the elastic modulus was 210,000 MPa (30,600 ksi). Figure 4.4 shows the stress-strain relationship used in the finite element model. A tri-linear stress-strain relationship was used in the model. The first portion of the relationship is the elastic behavior of the material. The hardening and plastic portions which follow the elastic portion use the von Mises yield surface.

The finite element package utilized for the analysis allowed only a constant initial stress over a single element. With only four elements across the flange, the model for the residual stresses in the specimen was highly simplified. The outside elements of each flange had a compressive residual stress and the interior elements had an equal tensile residual stress. Figure 4.5 shows the residual stress pattern used in the model. The residual stress used, 150 MPa (21.8 ksi) is approximately $0.50 \cdot F_y$. No residual stress is used in the web as the lateral-torsional buckling is not significantly affected by web residual stresses (Galambos, 1963).

The initial out-of-straightness (geometric imperfections) were modeled by adjusting the coordinates of the nodes of the web and the top flange. The maximum initial out-of-straightness was 1 mm (0.04 inches), approximately twice the average reported by Kubo and Fukumoto (1988). The following equation was used to specify the initial out-of-straightness of the compression (top) flange perpendicular to the minor axis of the beam (i.e., the sweep):

$$dx_1 = -\frac{1}{2} - \frac{1}{2}\cos\left(\frac{2z}{L}\right) \qquad \text{(Eq. 4.1)}$$

where z varies between 0 at the midspan and $L/2$ at the support end. The following equation was used to specify variation in the sweep over the height of the web:

$$dx_2 = \frac{1}{2} - \frac{1}{2}\cos\left(\frac{y}{d}\right) \qquad \text{(Eq. 4.2)}$$

where y varies between 0 and the depth, d. The tension (bottom) flange was assumed to be straight. The total out-of-straightness of the web was the product of dx_1 and dx_2.

The residual stresses and the initial out-of-straightness in the model can greatly affect the behavior of the model. With too much initial out-of-straightness, the model will buckle prematurely or not behave as expected. If not enough residual stress or initial displacement is included, then the model will be too strong. The amount of residual stresses was varied from the 150 MPa shown in Figure 4.5 to arrive at a model that behaved as expected. Other residual stresses attempted included 100 MPa, 120 MPa, and 200 MPa.

Boundary conditions were used to impose symmetry at the midspan cross-section. Also, boundary conditions modeled the support end bracing at the end of the girder. Figure 3.9 shows the cross-section of the model at the midspan; the points in the figure are defined in Section 3.3.2. Table 4.2 lists the boundary conditions for each point at the midspan. The web deflections at midspan are controlled through point A. The web does not distort, thus points B and C are rigidly constrained to point A. The remaining boundary conditions are required by

the symmetry conditions at midspan. Figure 3.10 shows a cross-section of the model at the support end. Table 4.3 lists the boundary conditions for each point at the support end. The support conditions are controlled through point C. The web is not permitted to distort.

4.3.3 Results of Analyses

Non-linear, displacement-controlled static analyses of the finite element model were conducted. Table 4.5 compares the results of the finite element analyses to the results of the test of beam B2B-C1 by Kubo and Fukumoto. Only the results based on the model with a residual stress of 150 MPa are shown. The finite element analysis results are very similar to the test results. The table lists the maximum load, P_{ult}, and the corresponding moment, M_{ult}.

The test results and the finite element analysis results are very similar. The finite element analysis captured the lateral-torsional buckling behavior of the beam very well despite the approximations made for the initial out-of-straightness and residual stresses. Figure 4.6 shows the location of the nodes used in the discussion of the analysis results. All of the nodes are at the midspan of the girder. The vertical (y axis) deflection is labeled *u2* for each node, and the transverse (x axis) deflection is labeled *u3*. Figure 4.7 shows the location of elements used in the discussion of the results. The strains in each direction are given at the upper and lower surfaces of each element. The circles on the figure show the location where the strains are reported.

Figure 4.8 compares the normalized moment versus the midspan deflection of the finite element model with the results from Kubo and Fukumoto (1988). The locations of the nodes in the finite element model are shown in Figure 4.6. The lateral deflection of the top and bottom flanges are shown at Nodes 32100 and 100, respectively. For Node 32700, the vertical deflection is shown and compared to the elastic deflection from linear elastic theory. The expected elastic deflection compares well with vertical deflection from the finite element

analysis with a constant difference of 10 percent until the beam experiences significant lateral deflections. The analysis did not run through the post-buckling behavior.

The lateral deflection of Node 32100 is similar to the lateral deflection of the compression flange of the test beam. In the test, the beam begins to experience significant lateral deflections at a smaller load as can be seen in Figure 4.8. Node 100 does not experience much lateral deflection, since the beam rotates about a point C_{LB} close to the bottom flange. The test deflections and finite element deflections compare very well.

Figure 4.9 shows the deflected shape of the finite element model. The deflection has been magnified and the view rotated. Figure 4.9 shows that the beam pivots about a location along the vertical axis close to the juncture of the bottom (tension) flange to the web. This results in a large lateral deflection of the top (compression) flange with little or no lateral deflection of the tension flange. The lack of distortion in the web confirms that the web was sufficiently stocky to mobilize the torsional stiffness of the entire cross-section.

Figure 4.10 compares the strain separation in the top flange of the finite element model of the beam with the test results from Kubo and Fukumoto (1988). The figure shows the normalized moment versus strain. The locations of the elements shown in the figure are given in Figure 4.7. The strain separation occurs between the two sides of the girder, indicating lateral buckling. The analysis was terminated before local buckling.

4.3.4 Models of FRRB Behavior

The finite element model of beam B2B-C1 was modified to include the effect of FRRBs attached to the ends of the beam. The first modified model included an FRRB modeled using shell elements. Analysis of this model was intended to show that an FRRB would improve the lateral-torsional behavior of the beam. The second modified model restrained the in-plane rotation of the compression flange by attaching a rotational spring to the compression

flange at the support end. Analysis of the second model was intended to show that the simplest form of rotational restraint at the end of the unbraced length would improve the lateral-torsional behavior of the beam.

The FRRB had the same thickness as the top flange, and was four elements wide. The widths of the elements across the width of the FRRB were the same as the lengths of the elements in the girder flange, so the total width of the FRRB was 167.5 mm (6.6 in). The length of the FRRB was used to control the stiffness of the FRRB since the width and thickness were set. The rotational restraint provided by the FRRB can be related to the rotational stiffness, $k_\theta = 2EI/L$, of the FRRB. The derivation of this stiffness is given in Chapter 5. Figure 4.11 shows a plan view of the model with the FRRB incorporated. The length of the FRRB in the model is shown in Figure 4.11. Only half of the FRRB was included in the model due to the symmetry. The reasons for the symmetry assumptions and the symmetry boundary conditions used in the finite element model are discussed in Chapters 5 and 6. The rotational stiffness of the FRRB is 502 kN-m.

The rotational spring used in the second modified model had a stiffness of 3,000 kN-m, approximately six times stiffer than the FRRB. The rotational spring was added to the compression flange at the support end as a specialized element in the finite element model. The spring element provided rotational stiffness only with respect to the vertical axis of the girder.

Table 4.6 shows the ultimate load, P_{ult}, and the corresponding moment, M_{ult}, from the analyses of the two modified models. The analysis with the FRRB achieved an increase of 59% of the lateral-torsional buckling critical moment. Although stiffer, the rotational spring achieved an increase of 54% of the lateral-torsional buckling critical moment, 97% of the critical moment of the analysis with the FRRB. The difference in the behavior is possibly

caused by the FRRB providing additional lateral and twisting restraint along the length of the top flange.

Figure 4.12 shows the normalized moment versus midspan deflection for the FRRB model. The location of the nodes is the same as in Figure 4.8. As with the previous analysis, the elastic deflection compares well to the vertical deflection with a constant difference of 10 percent until the beam experiences significant lateral deflections. Node 100 experiences more lateral deflection than in the previous analysis (although the load level is higher). In the latter part of the analysis, the lateral displacement at Node 100 is roughly 60 percent of the magnitude of that at Node 32100. This indicates that the location of point C_{LB} has moved up higher along the girder web than in the previous analysis.

Figure 4.13 shows the deflected shape of the finite element model at the final step in the analysis. The displacement has been magnified and the view rotated. A local buckle has formed in the top flange near the midspan. Figure 4.14 shows the deflected shape of the finite element model at an earlier stage of the analysis. The view was just after the beam buckled laterally. The rotation and magnification of the deflected shape are the same as in the previous figure. The local buckle that was visible in Figure 4.13 is just beginning to become visible in this figure.

Figure 4.15 shows the normalized moment versus strain for the FRRB model. The strain separation shown in the figure indicates the occurrence of both lateral-torsional buckling and local flange buckling. Figure 4.15 shows that a local buckle develops near the point at which the peak load is reached, confirming the observation from Figure 4.13. The beam has buckled locally immediately after the lateral buckle formed. However, the lateral buckle had begun to form earlier in the beam when the strains on the opposite tips of the flange began to separate.

Figure 4.16 shows the normalized moment capacity versus midspan deflection for the analysis of the second modified model with the rotational spring. The elastic deflection compares well to the vertical deflection with a constant difference of nearly 10 percent until the beam experiences significant lateral deflections. The location of point C_{LB} has moved up higher than in the original model. This can be seen by the large lateral deflections of the bottom flange. The model did not run through the post-buckling behavior.

Figure 4.17 shows the deflected shape of the finite element model with the rotational spring. The displacement has been magnified and the view rotated. The twisting of the beam corresponds to the shape expected from a beam in lateral-torsional buckling. The top flange in compression has moved laterally and rotated over while the bottom flange in tension has mostly translated due to rotation. Figure 4.18 shows the normalized moment capacity versus strain for finite element model with the rotational spring. The strain separation indicates lateral-torsional buckling has occurred.

4.4 Summary

Several conclusions can be drawn from the development and analysis of finite element models of beam B2B-C1. First, finite element models can be developed to simulate the lateral-torsional buckling behavior of I-shaped girders. Through careful consideration of the finite element modeling parameters, beam B2B-C1 from Kubo and Fukumoto (1988) served as a basis for modeling lateral-torsional buckling behavior. Two of the most important modeling parameters were the initial out-of-straightness and the residual stresses in the flanges. Second, the modified finite element model with the FRRB had better lateral-torsional buckling behavior than the original model of the beam alone. The modified model with the rotational spring also had better lateral-torsional buckling behavior than the beam. These results provide further motivation for the studies of I-girders with FRRBs, presented in Chapters 5 and 6.

Table 4.1 Dimensions of beam specimens (Kubo and Fukumoto (1988))

Specimen	d	b_f	t_w	t_f	L_b	L_b/r_y	b/t_f	h/t_w
B2B-A1	298.0	150.3	3.05	4.32	1800	53.8	17.40	94.80
B2B-B1	298.3	150.5	3.05	4.31	2400	71.6	17.46	94.98
B2B-C1	298.3	150.5	2.94	4.22	3350	99.7	17.83	98.59

Note: All dimensions are in mm. To convert to inches, 1 inch = 25.4 mm.

Table 4.2 Mean material properties (Kubo and Fukumoto (1988))

Series	Location	F_y (MPa)	F_u (MPa)	E (MPa)	ν	ΔL (%)
B1B	4.5 mm - flange	298	446	211,000	0.280	39
B2B	3.2 mm - web	316	464	211,000	0.278	37
B3B	4.5 mm - flange	262	438	209,000	0.296	42
B4B	3.2 mm - web	303	464	215,000	0.301	36

Table 4.3 Boundary conditions at midspan of finite element models

DOF	Location				
	A	A'	B	C	C'
Δx	free	free	rigid constraint to point A	rigid constraint to point A	free
Δy	free	free	"	"	free
Δz	fixed	fixed	"	"	fixed
θx	fixed	fixed	"	"	fixed
θy	fixed	fixed	"	"	fixed
θz	free	free	"	"	free

Table 4.4 Boundary conditions at support end of finite element models

DOF	Location				
	A	A'	B	C	C'
Δx	rigid constraint to point C	free	rigid constraint to point C	fixed	free
Δy	"	free	"	fixed	fixed
Δz	"	free	"	free	free
θx	"	free	"	free	free
θy	"	free	"	free	free
θz	"	free	"	fixed	fixed

Table 4.5 Results of finite element model

	P_{ult} (kN)	M_{ult} (kN-m)	M_{ult} / M_y	P_{FE} / P_{test}
Test Results	44.4	37.2	0.58	-
FE Model	43.8	36.7	0.56	0.99

Note: To convert to kips, 1 kip = 4.45 kN. To convert to kip-ft, 1 kip-ft = 1.356 kN-m

Table 4.6 Results of modified finite element models

	P_{ult} (kN)	M_{ult} (kN-m)	M_{ult} / M_y	$P_{modified} / P_{FE}$
Original FE Model	43.8	36.7	0.56	-
FE Model with FRRB	70.4	59.0	0.91	1.59
FE Model with Spring	68.3	57.2	0.88	1.54

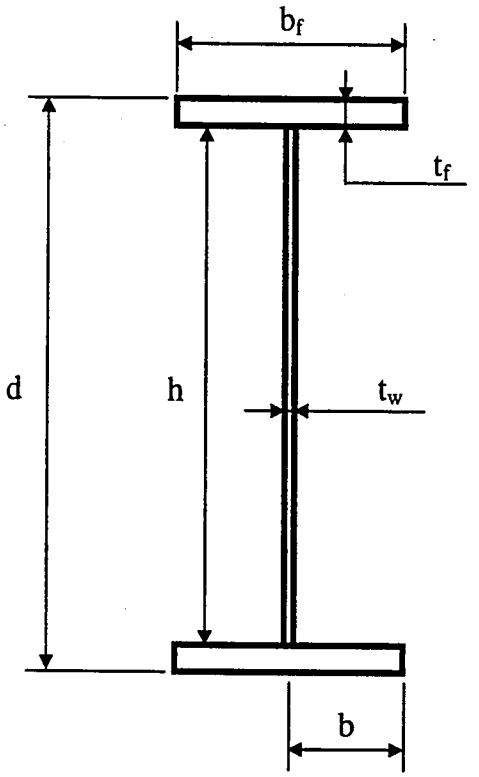

Figure 4.1 Cross-section from Kubo and Fukumoto (1988)

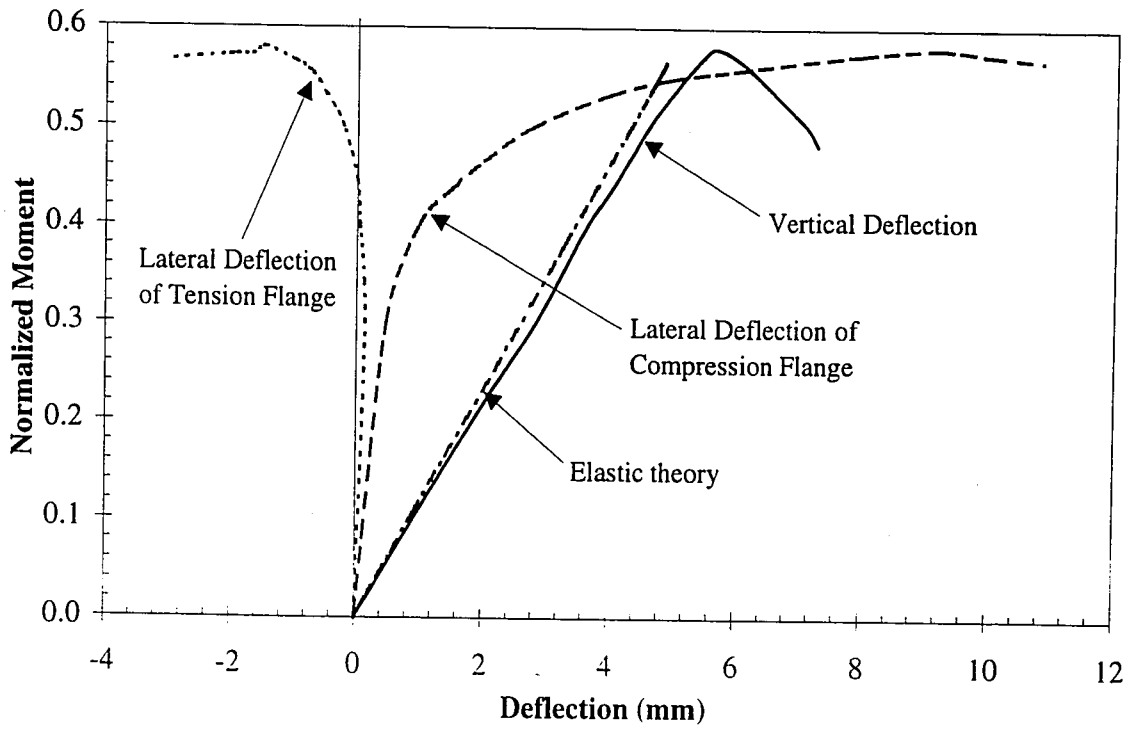

Figure 4.2 Normalized moment versus deflection (from Kubo and Fukumoto (1988))

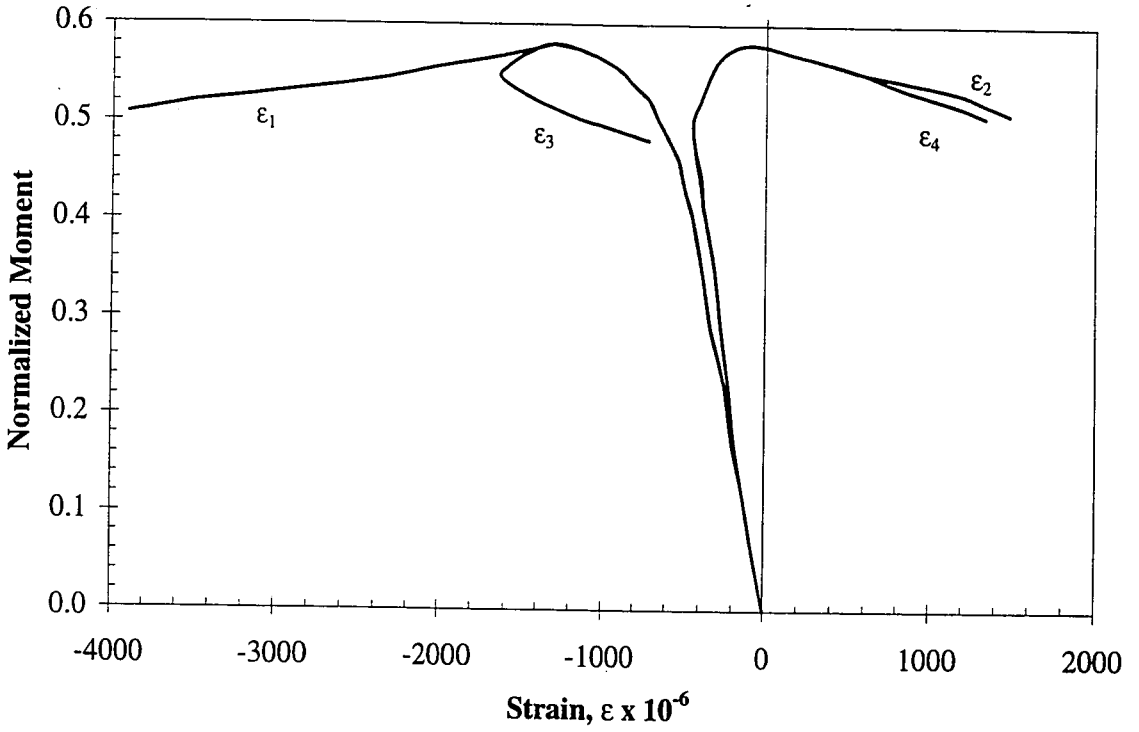

Figure 4.3 Normalized moment versus longitudinal strain in compression flange (from Kubo and Fukumoto (1988))

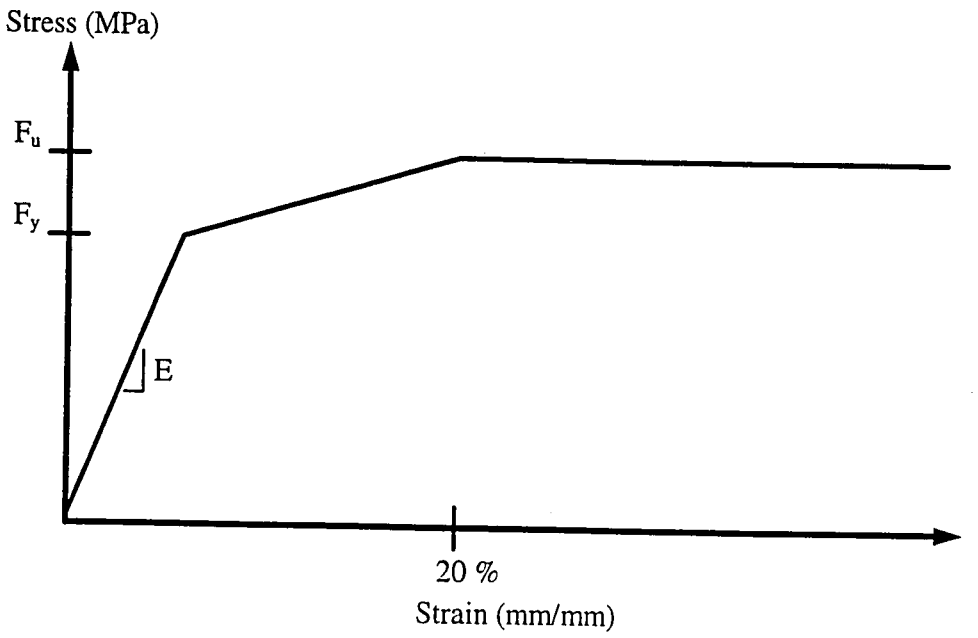

Figure 4.4 Stress-strain relationship used in finite element models

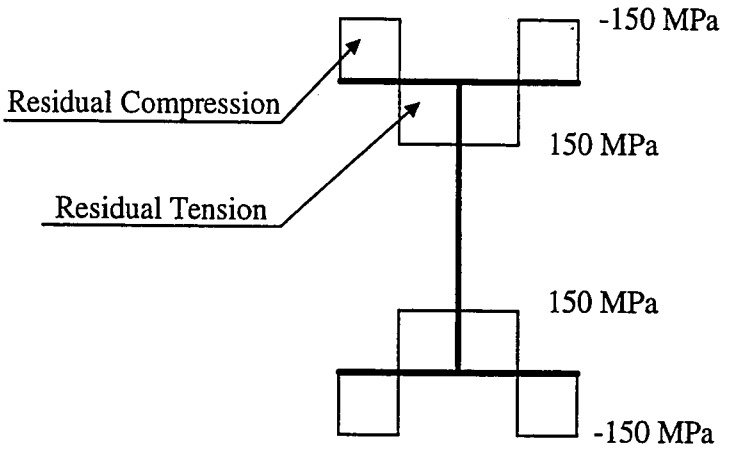

Figure 4.5 Residual stress distribution for finite element models

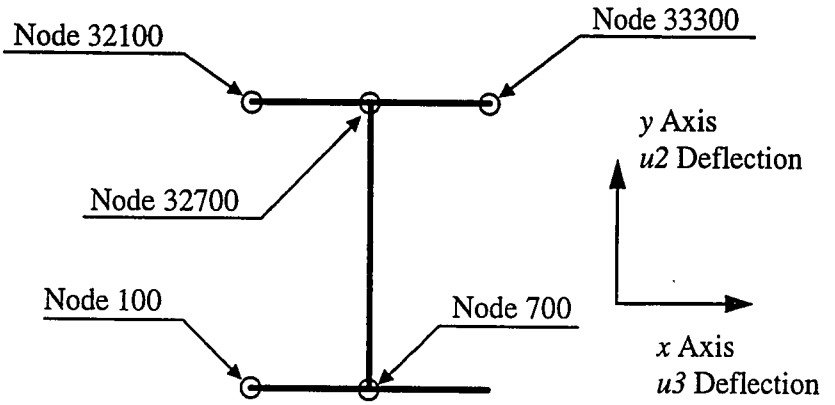

Figure 4.6 Location of nodes at midspan of finite element models

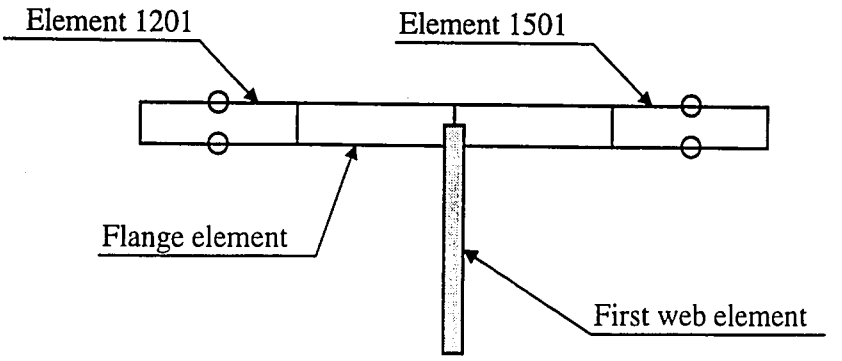

Figure 4.7 Location of elements at midspan of finite element models

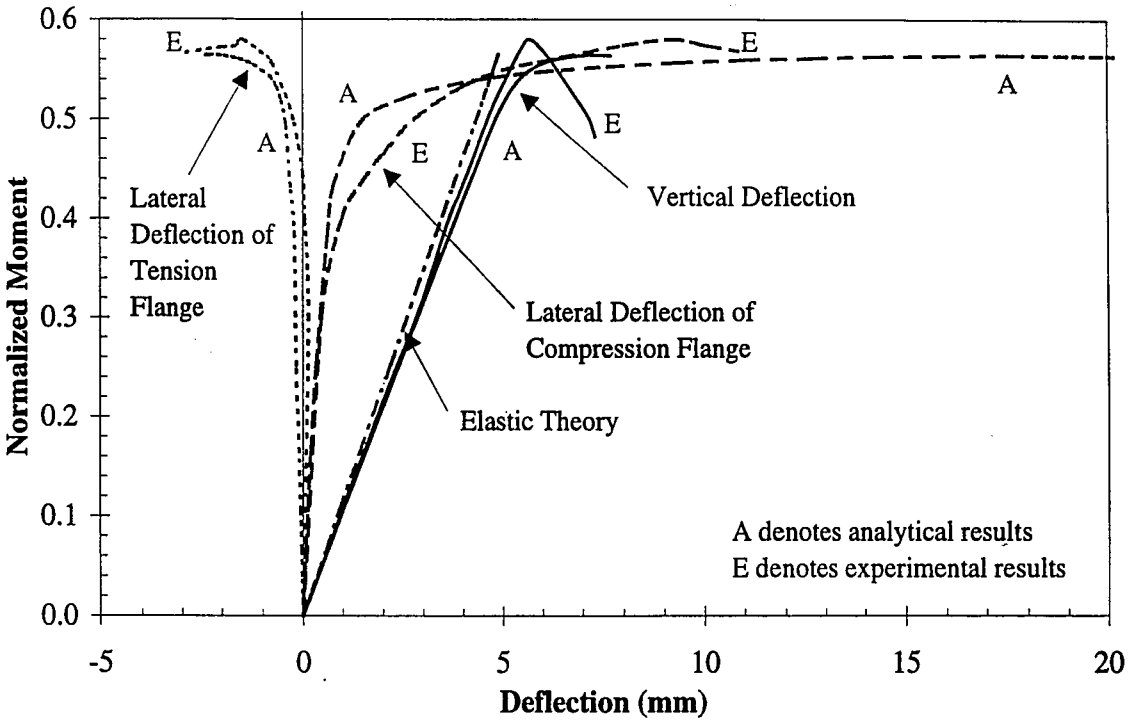

Figure 4.8 Normalized moment versus deflection for finite element model of B2B-C1

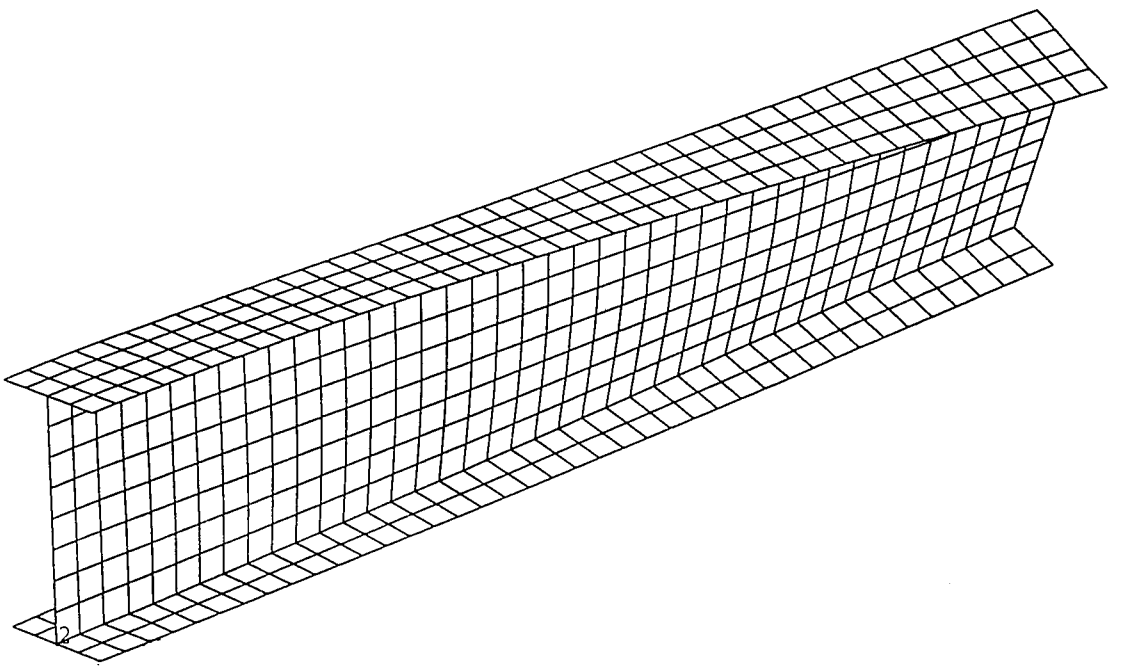

Figure 4.9 Deflected shape of finite element model of B2B-C1

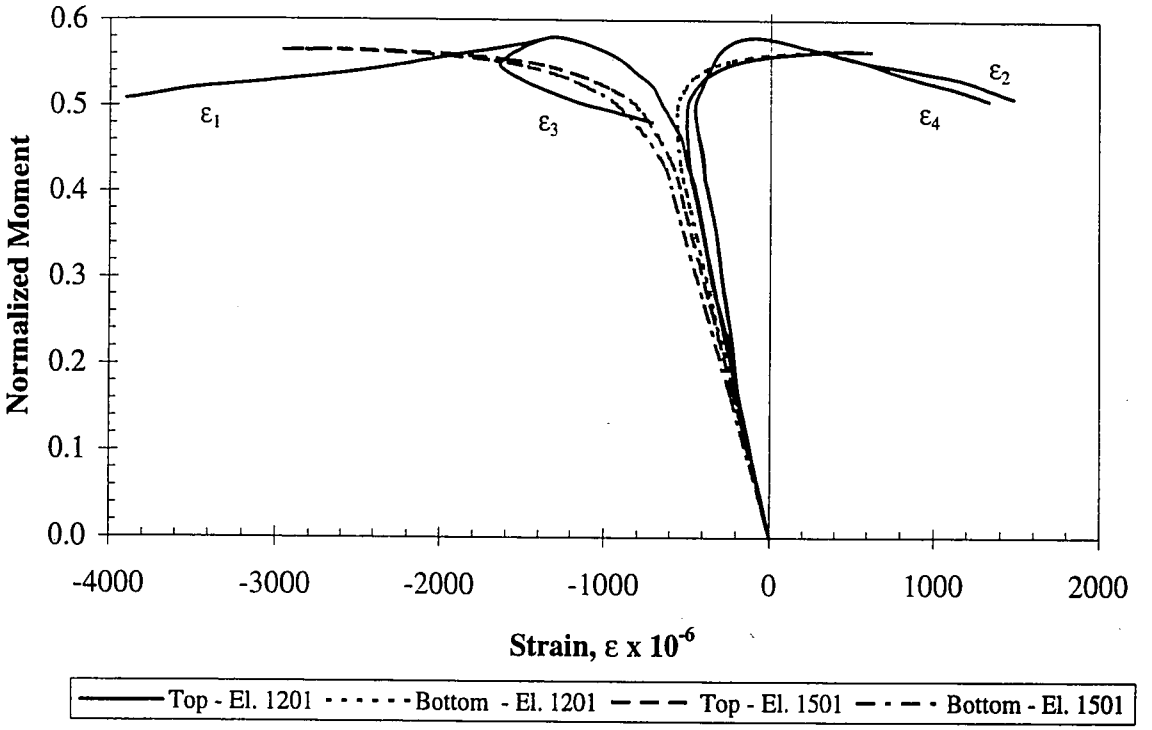

Figure 4.10 Normalized moment versus longitudinal strain in compression flange for finite element model of B2B-C1

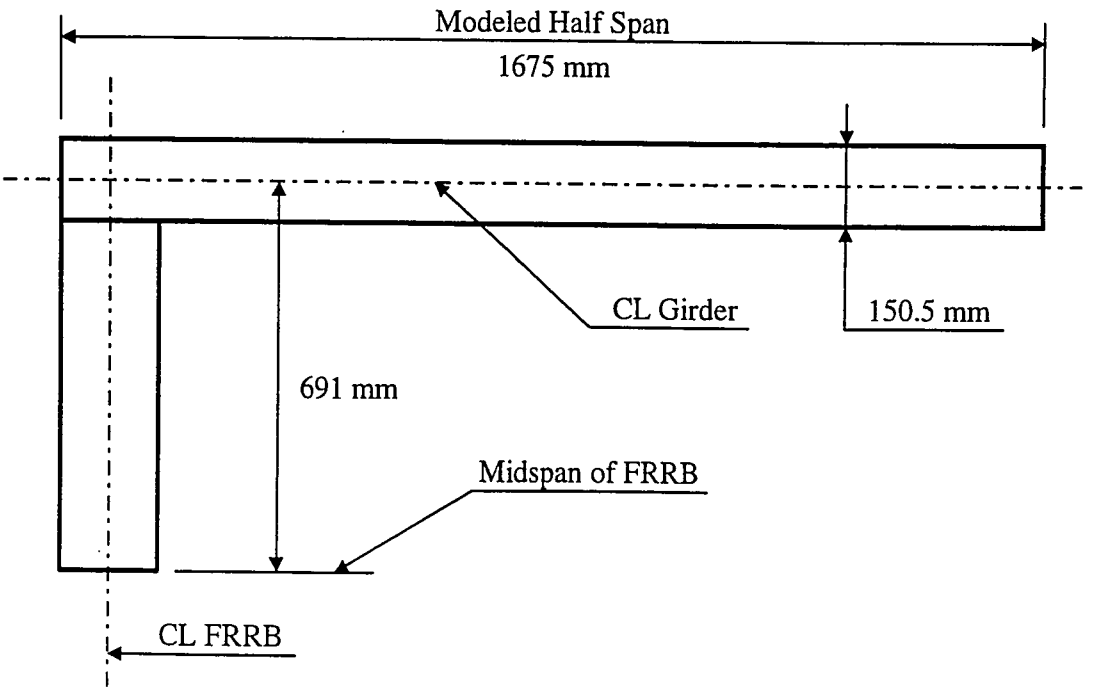

Figure 4.11 Layout of compression flange with FRRB for modified finite element model

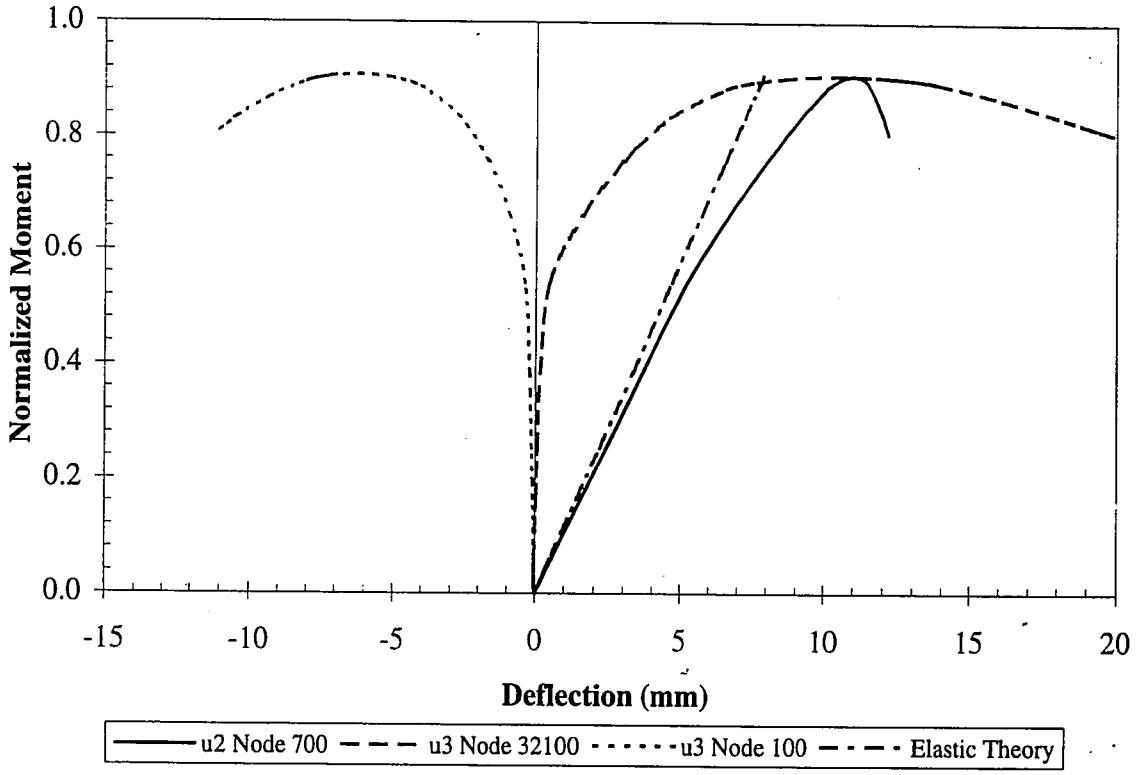

Figure 4.12 Normalized moment versus deflection for modified finite element model of B2B-C1 with FRRB

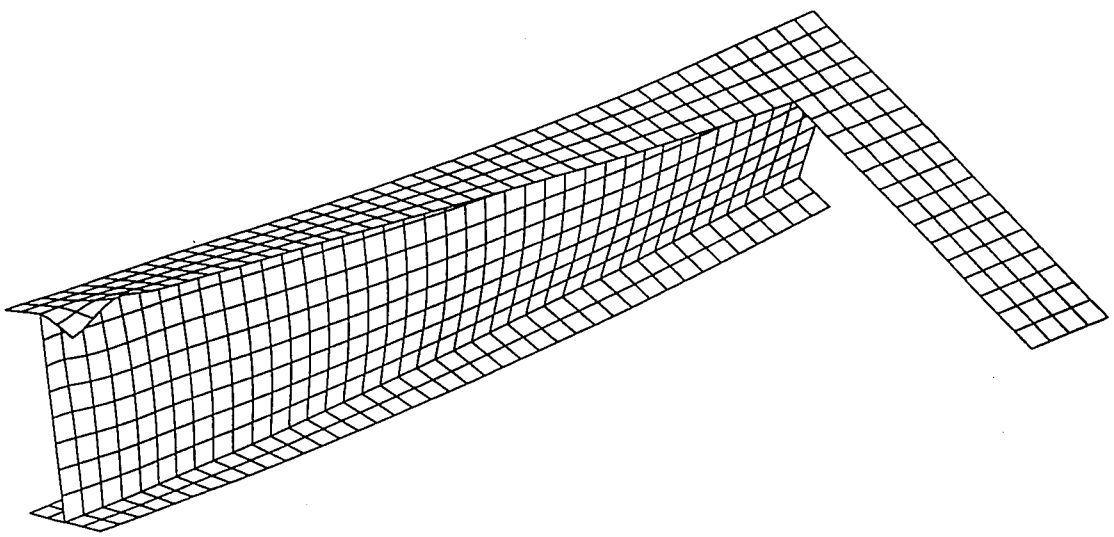

Figure 4.13 Deflected shape at end of analysis of modified finite element model of B2B-C1 with FRRB

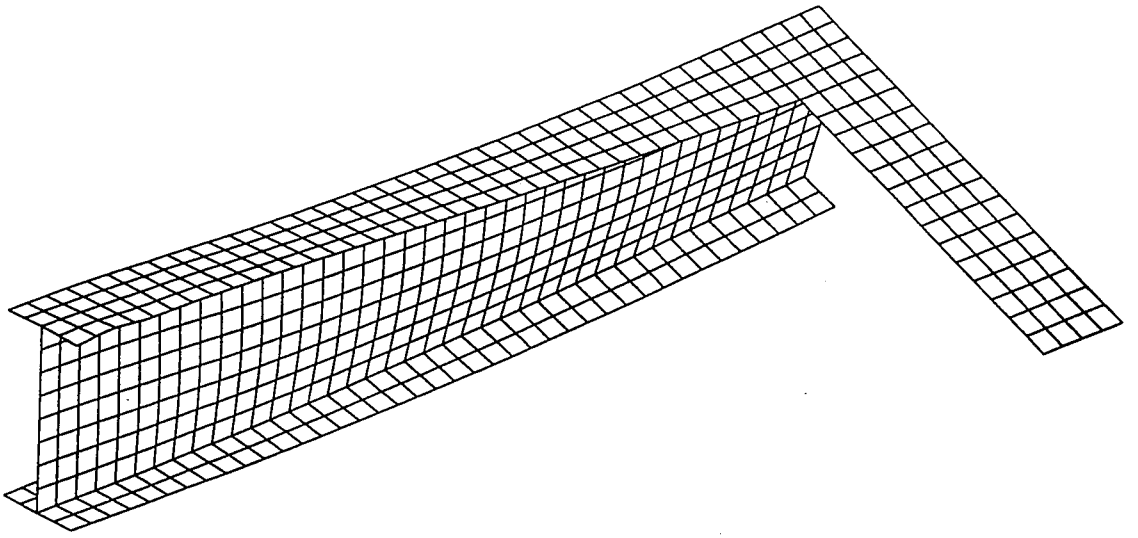

Figure 4.14 Deflected shape immediately after lateral buckling of modified finite element model of B2B-C1 with FRRB

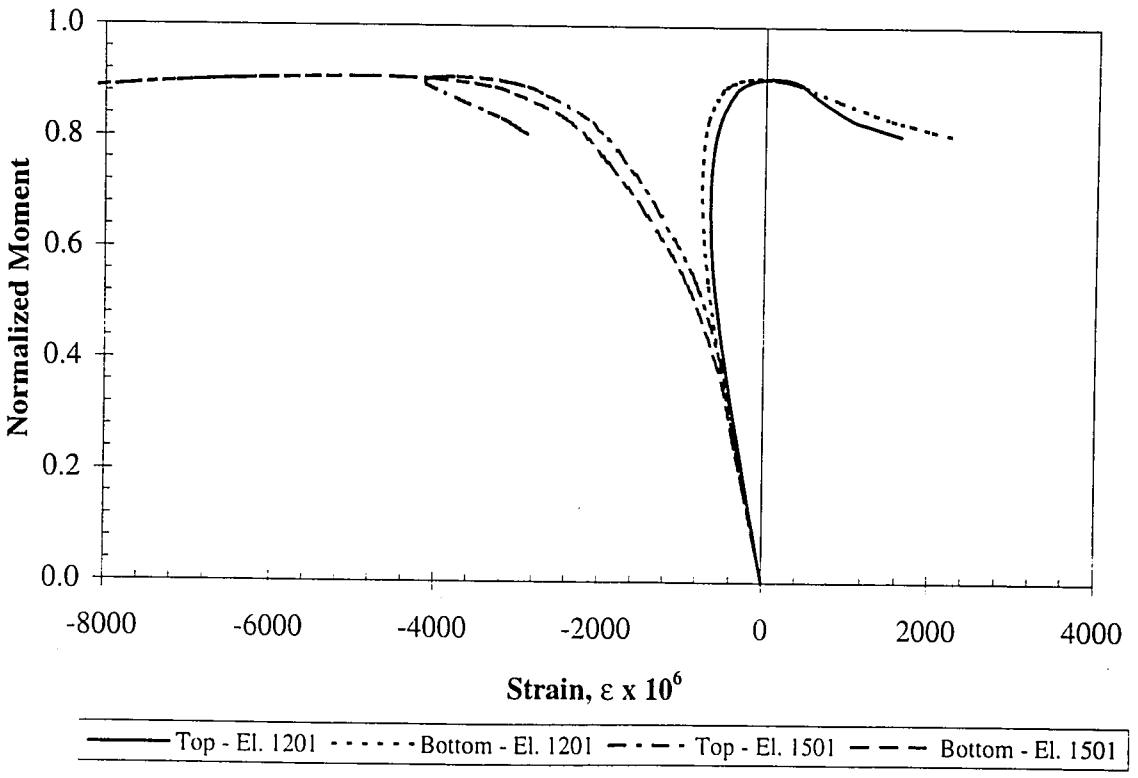

Figure 4.15 Normalized moment versus longitudinal strain in compression flange for modified finite element model of B2B-C1 with FRRB

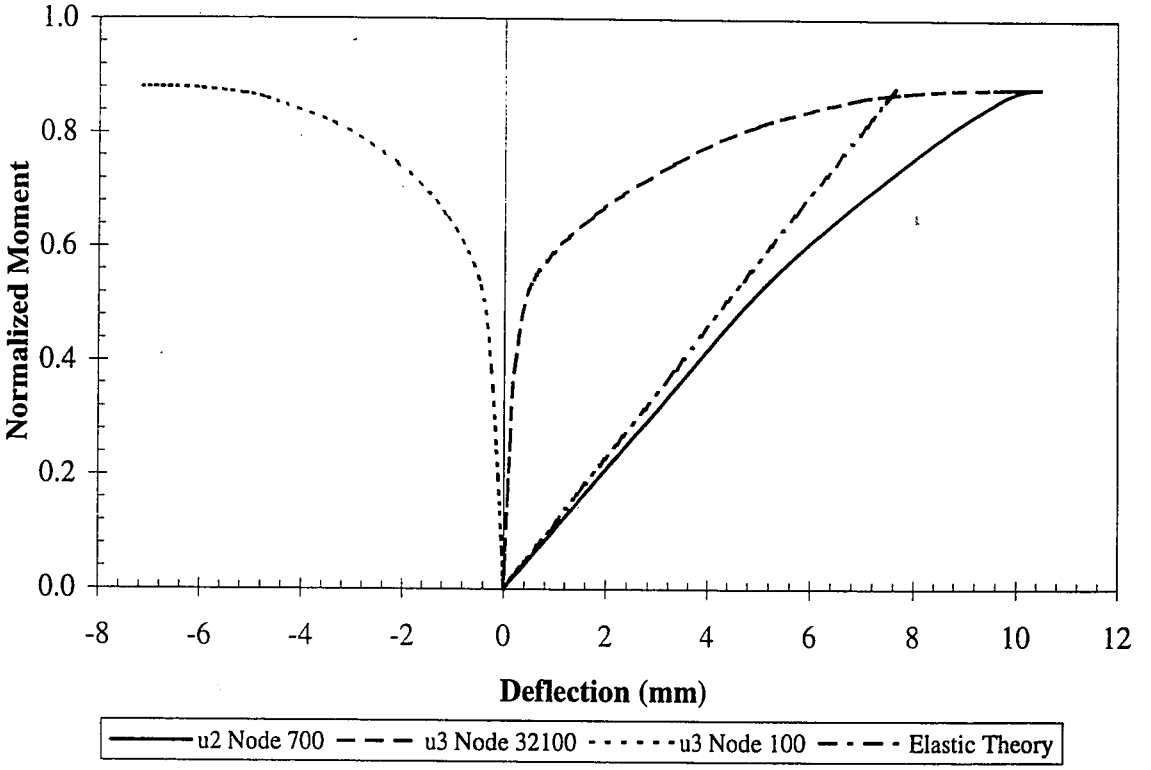

Figure 4.16 Normalized moment versus deflection for modified finite element model of B2B-C1 with rotational spring

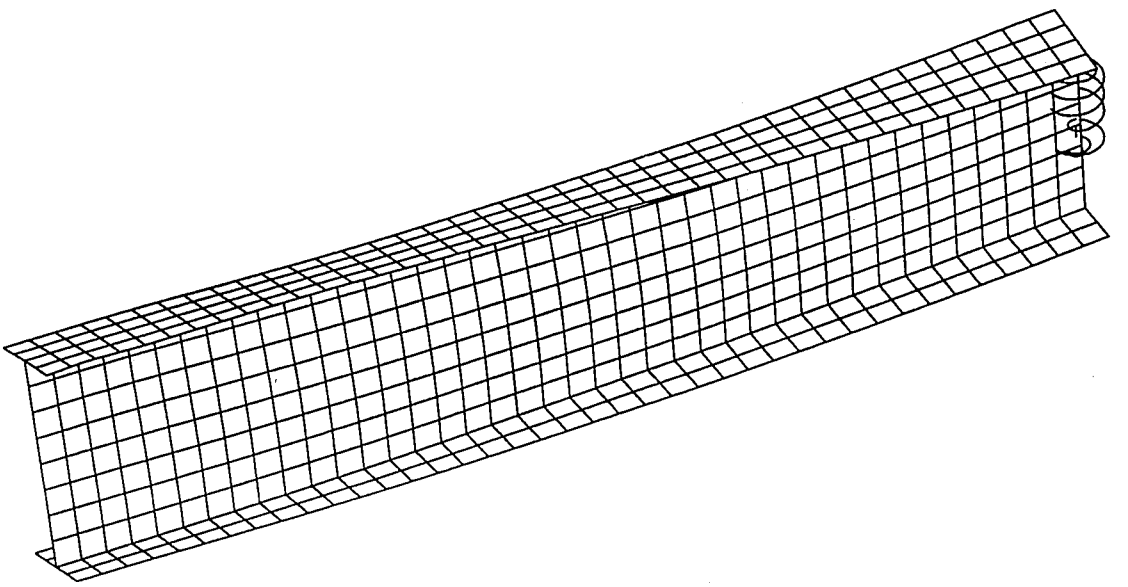

Figure 4.17 Deflected shape of modified finite element model of B2B-C1 with rotational spring

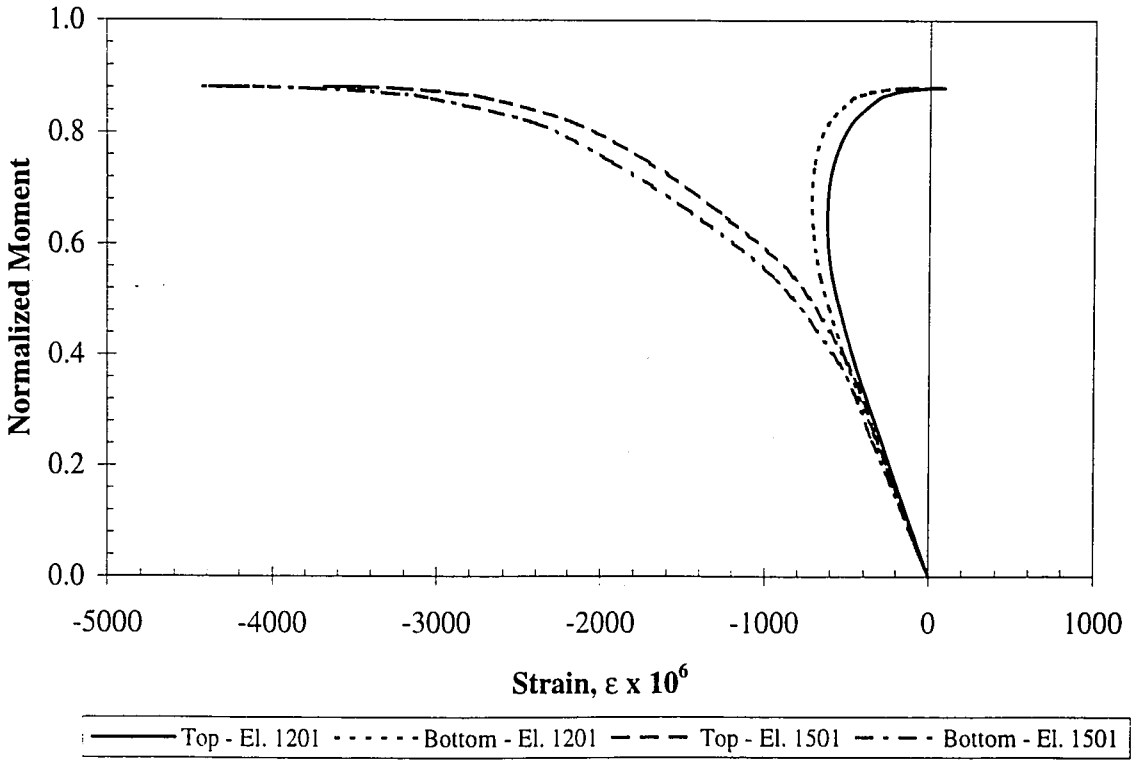

Figure 4.18 Normalized moment versus longitudinal strain in compression flange for modified finite element model of B2B-C1 with rotational spring

5. Analysis of Girders with Flange Rotational Restraint Braces

5.1 Introduction

Methods for analyzing the lateral-torsional buckling resistance of girders with flange rotational restraint braces are presented in this chapter. The first method involves solution of the differential equations considering the rotational restraint provided by the FRRB. The second method uses frame alignment charts to determine the restraining effect of the FRRB. Both methods result in effective length (K) factors which are used with AASHTO LRFD design equations to determine the lateral-torsional buckling resistance. The equations are used so that inelastic buckling can be included in the resistance calculations.

The analysis of girders with FRRBs begins with the design of prototype girders according to the AASHTO LRFD Bridge Design Specifications (1994). A standard diaphragm spacing is used. The diaphragm spacing is then increased and the required dimensions of FRRBs are determined using the analysis methods presented in this chapter.

The analysis methods are applied to prototype I-girders for the prototype bridges described Section 2.5. Four prototype I-girders are designed, including girders for the 33.5 m (110 ft) span bridge and the 50 m (164 ft) span bridge. For each bridge, girders with steel yield strengths of 485 MPa (70 ksi) and 690 MPa (100 ksi) are designed. Thus, the span length of the bridge and the yield strength of the steel are the two parameters that were varied. The girder spacing and thickness of the deck were held constant. Initially, the girders are designed for the original unbraced lengths shown in Figure 2.7.

A program previously developed for steel girder design was utilized to develop cross-section dimensions for the prototype girders. The program uses the AASHTO LRFD design specifications (Czaplicki, 1996). The program optimizes the cross-sections to achieve the minimum weight. The cross-sectional dimensions provided by the program were impractical or

had a high lateral-torsional buckling resistance as a results of very large compression (top) flanges. The cross-sections were adjusted to insure that lateral-torsional buckling would control the girder design for the construction stage. These adjustments included decreasing the top flange size and also increasing the web thickness. This adjustment increased the weight of the cross-sections by approximately ten percent.

Table 5.1 lists the cross-section dimensions of the four prototype girders. Figure 5.1 shows the general arrangement of the cross-sections and defines the symbols used in Table 5.1. The girders were designed as composite girders in the service stage. Lateral-torsional buckling controlled the design for the construction stage. A girder design was controlled by lateral-torsional buckling when the lateral-torsional buckling capacity slightly exceeded the factored construction stage load. The design of the girders for the service stage assumed that the 485 MPa (70 ksi) limit on the use of the plastic moment capacity could be ignored, and that fatigue did not control the design of the cross-section.

The prototype girders were initially designed for the original unbraced lengths shown in Figure 2.7. FRRBs were then designed for the girders (without changing the girder cross-sections) using the increased unbraced lengths shown in Figure 5.2. Figure 5.2(a) shows the increased unbraced lengths for the 33.5 m span. Figure 5.2(b) shows the increased unbraced lengths for the 50 m span. Table 5.2 lists the FRRB dimensions. The FRRB dimensions are constant for a given span length (i.e., they do not change with yield strength). The FRRB length given in the table is the center-to-center girder spacing. The FRRB dimensions were determined such that a prototype girder with the increased unbraced lengths shown in Figure 5.2 would have a lateral-torsional buckling capacity similar to that of the prototype girder with the same cross-section dimensions and the unmodified unbraced lengths shown in Figure 2.7.

5.2 Finite Difference Solution of Differential Equations

5.2.1 Introduction

The couple differential equations for lateral-torsional buckling, discussed in Section 2.2.3, can be solved using a finite difference approach. As noted in Chapters 3 and 4, the FRRBs provide rotational restraint at the ends of an unbraced length between diaphragms (i.e., at the boundaries of the unbraced length). The differential equations cannot be solved directly with the FRRB boundary conditions. However, a finite difference method can be used to solve the coupled equations.

The finite difference method provides an approximate solution to differential equations. The domain of the independent variables of the differential equation is discretized, and the derivatives of the dependent variables are replaced with difference formulas written in terms of the dependent variables at discrete points. Over the domain of discrete points, the differential equations written in terms of the difference formulas become a system of simultaneous equations which can be solved to determine the values of the dependent variables at those points. The difference formulas are approximations of the derivatives. The accuracy of the approximation increases with an increase in the number of points. Of course, with an increase in the number of points, the size of the system of the simultaneous equations increases.

5.2.2 Formulation of Finite Difference Equations

The lateral-torsional buckling behavior of a girder is defined by two coupled differential equations, Equations 2.1 and 2.2, which are repeated here:

$$EI_y u^{iv} + M_x \phi'' + 2M_x' \phi' = 0 \qquad \text{(Eq. 5.1)}$$

$$EI_\omega \phi^{iv} - \left(GJ + M_x \beta_x\right)\phi'' - M_x' \beta_x \phi' + M_x u'' = 0 \qquad \text{(Eq. 5.2)}$$

For an unbraced length with certain boundary conditions, closed form solutions of Equations 5.1 and 5.2 can be obtained. For pin-ended lateral supports, u can related to ϕ by solving Equation 5.1. Then Equation 5.2 can be solved using the relationship between u and ϕ.

Figure 5.3 shows an unbraced length, L_b^{FRRB}, discretized into $2m$ even segments, h, with $2m+1$ points. One lateral support end is point 0 and the other lateral support is point $2m$. These two points represent the ends of the unbraced length. The midpoint of the unbraced length occurs at point m. The numbering of the other points is sequential from point 0 to point $2m$. Points exist outside the unbraced length, such as point -1 shown in Figure 5.3. Those points are used to describe the boundary conditions. The finite difference model shown in Figure 5.3 can be used for unbraced lengths with or without FRRBs.

Equations 5.1 and 5.2 require difference formulas for the second and fourth derivatives of u and ϕ. The deflections u and ϕ are functions of the independent variable z which is the distance from the lateral support at one end. The distance to point i is z_i, and the corresponding u and ϕ deflections are $u(z_i)$ and $\phi(z_i)$, written as u_i and ϕ_i. Equations 5.1 and 5.2 can be rearranged by separating the "resistance" terms from the "demand" terms. The resistance terms are those terms that contain section and material properties. The demand terms are those which the moment, M_o. The separation of the equations simplifies the matrix operations involved in the solution. Equation 5.1 has the following form in terms of finite differences:

$$EI_y \frac{(u_{i+2} - 4u_{i+1} + 6u_i - 4u_{i-1} + u_{i-2})}{h^4} = -M_o \frac{(\phi_{i+1} - 2\phi_i + \phi_{i-1})}{h^2} \qquad \text{(Eq. 5.3)}$$

Equation 5.2 has the following form in terms of finite differences:

$$EI_\omega \frac{(\phi_{i+2} - 4\phi_{i+1} + 6\phi_i - 4\phi_{i-1} + \phi_{i-2})}{h^4} - GJ \frac{(\phi_{i+1} - 2\phi_i + \phi_{i-1})}{h^2} = M_o \beta_x \frac{(\phi_{i+1} - 2\phi_i + \phi_{i-1})}{h^2} - M_o \frac{(u_{i+1} - 2u_i + u_{i-1})}{h^2} \qquad \text{(Eq. 5.4)}$$

Equations 5.3 and 5.4 are written for each point in the domain shown in Figure 5.3. Thus for $2m+1$ points, a system of $2(2m+1)$ equations results. In Equations 5.3 and 5.4, the moment gradient, M_x', is assumed to be zero (i.e., uniform moment) to simplify the equations.

5.2.3 Boundary Conditions

Boundary conditions at the ends of the unbraced length are necessary to solve Equations 5.1 and 5.2. When the finite difference method is used to solve the equations, the boundary conditions allow the dependent variables (u and ϕ) at points outside the domain (i.e., the unbraced length) to be eliminated from the system of equations. In Equations 5.3 and 5.4, one or two points before and after each point in the domain are included in the difference formulas. At points near the boundaries, points outside the boundaries are included in the difference formulas. Writing equations for the boundary conditions will allow the points outside of the boundaries to be related to points inside the boundaries (the domain).

The boundary conditions are complicated due to the presence of the FRRB. The problem is simplified if the unbraced length is assumed to be symmetric with regards to the length, and a solution is generated for only one half of the unbraced length. This requires that the unbraced length is divided into two halves, as shown in Figure 5.3. Figure 5.4 shows the boundary conditions at the midpoint and support end of half of an unbraced length.

At the midpoint of the unbraced length, symmetric boundary conditions are imposed. The midpoint boundary conditions have the following form:

$$u_m' = 0 = \frac{u_{m+1} - u_{m-1}}{2h}$$
$$\phi_m' = 0 = \frac{\phi_{m+1} - \phi_{m-1}}{2h} \qquad \text{(Eq. 5.5)}$$

where m indicates the midpoint of the unbraced length.

The equations above can be solved for the value of the dependent variables at points beyond the midpoint in terms of values at points within the half of the unbraced length being analyzed as follows:

$$u_{m+1} = u_{m-1}$$
$$\phi_{m+1} = \phi_{m-1} \qquad \text{(Eq. 5.6)}$$

The relationships in Equation 5.6 are intuitive. If the segment is symmetric along the length, then the lateral deflection at a point just before the midpoint will be the same as at an equidistant point just after the midpoint. These relationships are used in the system of simultaneous equations, represented by Equations 5.3 and 5.4, to eliminate points outside the boundary at point *m*.

The support end with an FRRB has more complicated boundary conditions. Austin, et. al (1957) investigated I-beams with in-plane rotational restraint of both flanges. For an I-girder with FRRBs on the compression flange, the boundary conditions in terms of u and ϕ, are similar to those developed by Austin, et. al (1957). The moment induced in the compression flange from the curvature of the compression flange is related to the rotational stiffness of the FRRB. The total lateral deflection of the compression flange, u_c, is a combination of the lateral deflection, u, and twist, ϕ, of the section

$$u_c = u + \phi \cdot d'(1-\rho) \qquad \text{(Eq. 5.7)}$$

where d' is the distance center to center of the flanges and ρ is the singly-symmetric parameter defined by Kitipornchai and Trahair (1980). The singly-symmetric parameter is defined as the following:

$$\rho = \frac{I_{yc}}{I_y} \qquad \text{(Eq. 5.8)}$$

Lateral deflection of the compression flange, as a result of lateral deflection and twisting of the section, induces a moment in the compression flange about its vertical axis, M_{yc}:

$$M_{yc} = EI_{yc}u_c'' = EI_{yc}\left[u'' + \phi'' \cdot d'(1-\rho)\right] \quad \text{(Eq. 5.9)}$$

The lateral deflection of the compression flange produces a rotation about the vertical axis of the flange at the location of the FRRB. The rotation of the FRRB about the vertical axis of the compression flange creates the following moment, M_{FRRB}:

$$M_{FRRB} = k_\theta u_c' = k_\theta\left[u' + \phi' \cdot d'(1-\rho)\right] \quad \text{(Eq. 5.10)}$$

where k_θ is related to the rotational stiffness of the FRRB and equals the following:

$$k_\theta = \frac{2E_f I_{yf}}{L_s} \quad \text{(Eq. 5.11)}$$

where E_f is the modulus of elasticity for the FRRB, I_{yf} is the moment of inertia of the FRRB about the vertical axis, and L_s is the girder center-to-center spacing. As shown in Figure 5.4, the FRRB can be represented by a rotational spring with stiffness k_θ at the lateral support.

Figure 5.5 shows the deflected shape of a portion of a girder pair with an FRRB. The points of inflection in the lateral deflection of the compression flange are denoted with a circle. The detail above the deflected shape shows the moments acting at the joint between the compression flange and the FRRB. Using equilibrium about the joint, the moments are related as follows:

$$2M_{yc} = M_{FRRB} \quad \text{(Eq. 5.12)}$$

Substituting Equations 5.9 and 5.10 into Equation 5.12 yields the relationships between the lateral deflection of the compression flange and the rotation of the FRRB. After separating the variables, the relationships are as follows:

$$EI_{yc}u'' = \frac{k_\theta}{2}u'$$
$$EI_{yc}\phi'' = \frac{k_\theta}{2}\phi' \qquad \text{(Eq. 5.13)}$$

The boundary conditions at the support end with the FRRB can be expressed in terms of finite differences by replacing the derivatives with the finite difference formulas. In addition, lateral deflection and twist are restrained at the support ($z = 0$, $i = 0$), meaning u_0 and ϕ_0 equals zero. The boundary condition for the lateral deflection in terms of finite differences at the support location is the following:

$$EI_{yc}\frac{(u_1 - 2u_0 + u_{-1})}{h^2} = \frac{k_\theta}{2}\frac{(u_1 - u_{-1})}{2h} \qquad \text{(Eq. 5.14)}$$

Since u_{-1} is not in the segment being analyzed, Equation 5.14 can be rearranged to relate u_{-1} to u_1:

$$u_{-1} = \frac{-4EI_{yc} + k_\theta h}{4EI_{yc} + k_\theta h}u_1 = C_0 u_1 \qquad \text{(Eq. 5.15)}$$

where C_0 is the rotational restraint coefficient at point z_0. For simply supported lateral boundary conditions, k_θ would equal zero and C_0 would equal -1 which is the expected value. For fixed lateral boundary conditions, k_θ would equal infinity and C_0 would equal +1.

The boundary condition for ϕ are similar. The finite difference formulas for the twist in terms of finite differences at the support location is the following:

$$EI_{yc}d'(1-\rho)\frac{(\phi_1 - 2\phi_0 + \phi_{-1})}{h^2} = d'(1-\rho)\frac{k_\theta}{2}\frac{(\phi_1 - \phi_{-1})}{2h} \qquad \text{(Eq. 5.16)}$$

Since ϕ_{-1} is not in the segment being analyzed, Equation 5.16 can be rearranged to relate ϕ_{-1} to ϕ_1:

$$\phi_{-1} = \frac{-4EI_{yc} + k_\theta h}{4EI_{yc} + k_\theta h}\phi_1 = C_0\phi_1 \qquad \text{(Eq. 5.17)}$$

where C_0 is the same constant as defined in Equation 5.15.

5.2.4 Assembling and Solving the Finite Difference Equations

Once the boundary conditions are expressed in terms of finite differences, the number of simultaneous equations will equal the number of unknowns. For the model of one half of the unbraced length shown in Figure 5.5, the number of equations will be $2m$ where m is the number of segments from the support end to the midpoint of the unbraced length. Since the differential equations are coupled, the resulting simultaneous equations must be solved together.

The unknowns are the critical lateral-torsional moment, M_o and the deflections u_i and ϕ_i (from the u_1 and ϕ_1 to the u_m and ϕ_m). The simultaneous equations can be written in matrix form. The critical moment is obtained from an eigenvalue analysis of the resistance matrix and the demand matrix.

The resistance matrix, **R**, is composed of the elements from the left hand sides of Equations 5.3 and 5.4. The demand matrix, **D**, is composed of the right hand sides of Equations 5.3 and 5.4. Since the unknown lateral-torsional buckling moment is a common element of the right hand sides, the moment, M_o, can be brought outside of the demand matrix. In order to facilitate the construction of the matrices, they can be partitioned into sub-matrices as follows:

$$\left([\mathbf{R}] - M_o[\mathbf{D}]\right)\begin{pmatrix}\mathbf{u}\\ \phi\end{pmatrix} = \left(\begin{bmatrix}\mathbf{R}_{1,1} & \mathbf{0}\\ \mathbf{0} & \mathbf{R}_{2,2}\end{bmatrix} - M_o\begin{bmatrix}\mathbf{0} & \mathbf{D}_{1,2}\\ \mathbf{D}_{2,1} & \mathbf{D}_{2,2}\end{bmatrix}\right)\begin{pmatrix}\mathbf{u}\\ \phi\end{pmatrix} = 0 \qquad \text{(Eq. 5.18)}$$

where zero terms for entire sub-matrices have been applied according to Equations 5.3 and 5.4. Each sub-matrix, including those that are zero matrices, is of size $m \times m$. The vector is composed of **u** and ϕ deflection sub-vectors, each containing m elements.

The coefficients in front of the values of the lateral deflection u_i on the left hand side of Equation 5.3 populate the $\mathbf{R}_{1,1}$ sub-matrix. Terms from the ith simultaneous equation are placed in the ith row. Only some of the values in each sub-matrix are shown to give a sense of the construction of the sub-matrices. The boundary conditions, expressed in terms of finite differences, have been applied as appropriate for each sub-matrix. The following matrix shows the elements of the $\mathbf{R}_{1,1}$ sub-matrix:

$$\mathbf{R}_{1,1} = \frac{EI_y}{h^4}\begin{bmatrix} 6+C_0 & -4 & 1 & \cdots & \cdots & 0 \\ -4 & 6 & -4 & & & \vdots \\ 1 & -4 & 6 & & & \vdots \\ \vdots & & & \ddots & & \vdots \\ \vdots & & & & 7 & -4 \\ 0 & \cdots & \cdots & \cdots & -8 & 6 \end{bmatrix} \qquad \text{(Eq. 5.19)}$$

In a similar manner, the coefficients in front of the values of the twist ϕ_i on the left hand side of Equation 5.4 populate the $\mathbf{R}_{2,2}$ sub-matrix as follows:

$$\mathbf{R}_{2,2} = \frac{EI_\omega}{h^4}\begin{bmatrix} 6+C_0 & -4 & 1 & \cdots & \cdots & 0 \\ -4 & 6 & -4 & & & \vdots \\ 1 & -4 & 6 & & & \vdots \\ \vdots & & & \ddots & & \vdots \\ \vdots & & & & 7 & -4 \\ 0 & \cdots & \cdots & \cdots & -8 & 6 \end{bmatrix} + \frac{GJ}{h^2}\begin{bmatrix} 2 & -1 & 0 & \cdots & \cdots & 0 \\ -1 & 2 & -1 & & & \vdots \\ 0 & -1 & 2 & & & \vdots \\ \vdots & & & \ddots & & \vdots \\ \vdots & & & & 2 & -1 \\ 0 & \cdots & \cdots & \cdots & -2 & 2 \end{bmatrix} \qquad \text{(Eq. 5.20)}$$

The coefficients in front of the twist ϕ_i on the right hand side of Equation 5.3 populate the $\mathbf{D}_{1,2}$ matrix. The coefficients in front of the deflection u_i on the right hand side of Equation 5.4 deflections populate the $\mathbf{D}_{2,1}$ sub-matrix. The $\mathbf{D}_{2,1}$ sub-matrix has the same coefficients as the $\mathbf{D}_{1,2}$ sub-matrix. Both sub-matrices are as follows:

$$\mathbf{D}_{1,2} = \mathbf{D}_{2,1} = \frac{1}{h^2}\begin{bmatrix} -2 & 1 & \cdots & \cdots & 0 \\ 1 & -2 & & & \vdots \\ \vdots & & \ddots & & \vdots \\ \vdots & & & -2 & 1 \\ 0 & \cdots & \cdots & 2 & -2 \end{bmatrix} \qquad \text{(Eq. 5.21)}$$

The remaining coefficients in front of the twist ϕ_i on the right hand side of Equation 5.4 involving the β_x term populate the $\mathbf{D}_{2,2}$ matrix. The terms also have a sign opposite to the other demand sub-matrices. The sub-matrix has the following form:

$$\mathbf{D}_{2,2} = \frac{\beta_x}{h^2}\begin{bmatrix} 2 & -1 & \cdots & \cdots & 0 \\ -1 & 2 & & & \vdots \\ \vdots & & \ddots & & \vdots \\ \vdots & & & 2 & -1 \\ 0 & \cdots & \cdots & -2 & 2 \end{bmatrix} \qquad \text{(Eq. 5.22)}$$

When the sub-matrices are assembled to complete the resistance and demand matrices, an eigenvalue analysis can be performed to solve for the critical moment, M_o. The complete resistance and demand matrices will be of size $2m \times 2m$, making the eigenvalue analysis large for an unbraced length divided into a large number of segments.

The lowest eigenvalue corresponds to the critical lateral-torsional buckling moment. After the eigenvalues are found, the eigenvectors can be determined. The eigenvectors give the deformed shape. The eigenvectors can be checked to see if the deflections along the unbraced length correspond to the expected deformed shape. For instance, the lowest mode of the segment should have the u deflections increasing from a small value at point 1 to a maximum at

the midpoint *m*. The deformed shape for a pin-ended girder is a sine curve, so the shape of the lateral deflections of the a girder with an FRRB would be similar to a sine curve.

5.3 Finite Difference Analysis of the Prototype Girders

The finite difference method was used to determine the critical lateral-torsional buckling moment for the principal unbraced length of the prototype girders described in Section 5.1. The principal unbraced length is the one with the maximum bending moment assuming uniformly distributed loads are applied during the construction stage. For the 33.5 m span girders, the middle unbraced length of 9.05 m (29.68 ft) in Figure 5.2(a) has the maximum moment. For the 50 m span girders, the 11 m (36.09 ft) unbraced lengths have the maximum moment at the midspan FRRB shown in Figure 5.2(b).

To determine the lateral-torsional buckling resistance, the finite difference method is used in several steps. First, the prototype girders are analyzed without including FRRBs. The unbraced length is varied and the variation of the lateral-torsional buckling resistance is compared against the closed form solutions and the AASHTO LRFD design specifications. This verifies the finite difference approach. Then, FRRBs are included, and the variation of the lateral-torsional buckling resistance with unbraced length is compared with the results generated without including FRRBs. This comparison allows effective length (K) factors for the prototype girders with FRRBs to be determined. In Section 5.4, the K factors are used with the standard AASHTO LRFD lateral-torsional buckling resistance equations so that inelastic buckling can be considered.

As discussed in Section 2.2.4, the AASHTO LRFD design specifications have several expressions for the lateral-torsional buckling resistance during the construction stage. One of the major concerns is the slenderness of the web as defined by Equation 2.4. A girder with a web slenderness less than the limit in Equation 2.4 can mobilize the St. Venant torsional

resistance of the girder against lateral-torsional buckling. The AASHTO design specifications allow elastic lateral-torsional buckling resistance to be used for girders with web slenderness less than the limit in Equation 2.4 up to the yield moment.

Girders with slender webs, exceeding the limit in Equation 2.4, cannot mobilize the St. Venant torsional resistance. The elastic lateral-torsional buckling resistance, defined by Equation 2.15 for slender webs, reflects this condition. Furthermore, inelastic buckling is considered when the unbraced length is between the plastic length, L_p, and the transition length, L_r. The capacity of girders with slender webs is further reduced by the load shedding factor, R_b. All of the cross-sections listed in Table 5.1 have slender webs under the factored construction stage load.

Each of the prototype girders was analyzed without FRRBs for a range of unbraced lengths. Initially, the St. Venant torsional resistance was included in the analysis. The sections were also analyzed without including the St. Venant torsional resistance included. The girders were assumed to behave elastically over the range of unbraced lengths.

The finite difference analyses without FRRBs were compared with the classical solution given by Galambos (1968) for singly-symmetric sections and with the lateral-torsional buckling resistance given by Equation 2.11 from the AASHTO LRFD design specifications. Figure 5.6 shows the normalized moment capacity (defined as the lateral-torsional buckling moment divided by the yield moment) versus the unbraced length for the 33.5 m span 485 MPa yield strength steel prototype girder. The figure shows that AASHTO, classical, and finite difference solutions are very similar. Two sets of curves are shown: those including the St. Venant torsional resistance and those without it. It should be noted that, when the St. Venant torsional resistance is neglected, the results for the AASHTO equation for stocky webs (Equation 2.11) are the same as the results from the AASHTO equation for slender webs

(Equation 2.15) with R_b = 1. In Figure 5.6, the curves including the St. Venant torsional resistance are above the curves without the torsional resistance. Figure 5.7 shows similar results for the 33.5 m span 690 MPa yield strength steel prototype girder.

Each of the prototype girders was also analyzed with FRRBs. The results were compared to the finite difference analysis results without FRRBs. As discussed earlier, the FRRB provides a rotational restraint which is quantified using the coefficient C_0. C_0 depends on the rotational stiffness of the FRRB, k_θ, as well as the moment of inertia and the elastic modulus of the compression flange, and the finite difference segment length, h. For a wide range of unbraced lengths, the rotational restraint provided to the girder by the FRRB should be kept constant as the unbraced length (and h) change. This is accomplished by keeping C_0 constant over the range of unbraced lengths. Thus, rather than assuming that the same FRRB dimensions would be used over the range of unbraced lengths, C_0 was kept constant.

For a given lateral-torsional buckling moment, each girder with and without FRRBs will have a corresponding unbraced length. The K factor is the ratio of the unbraced lengths at the same moment capacity:

$$K = \frac{L_b}{L_b^{FRRB}} \qquad \text{(Eq. 5.23)}$$

The lengths in Equation 5.23 can be found for a given lateral-torsional buckling moment by constructing normalized moment capacity versus unbraced length curves. These are constructed for the four prototype girders. The graphs compare the (elastic) finite difference solutions with and without the FRRBs.

Figure 5.8 shows the normalized moment capacity versus unbraced length for the 33.5 m span 485 MPa yield strength steel prototype girder. The web is assumed to be stocky, and the St. Venant torsional resistance is included. A consistent K factor of 0.66 is determined, with the

rotational restraint coefficient, C_0, held constant. Figure 5.9 shows the normalized moment capacity versus unbraced length for the 33.5 m span 690 MPa yield strength steel prototype girder. The web is assumed to be stocky. A consistent K factor of 0.66 is determined for a constant C_0. Figure 5.10 shows the normalized moment capacity versus unbraced length for the 50 m span 485 MPa yield strength steel prototype girder. The web is assumed to be stocky. A consistent K factor of 0.68 is determined for a constant C_0. Figure 5.11 shows the normalized moment capacity versus unbraced length for the 50 m span 690 MPa yield strength steel prototype girder. The web is assumed to be stocky. A consistent K factor of 0.66 is determined for a constant C_0.

The prototype girders were also analyzed assuming the web was slender and the St. Venant torsional resistance was not included. Figure 5.12 shows the normalized moment capacity versus unbraced length for the 33.5 m span 485 MPa yield strength steel prototype girder. A consistent K factor of 0.66 is determined for a constant C_0. Figure 5.13 shows the normalized moment capacity versus unbraced length for the 33.5 m span 690 MPa yield strength steel prototype girder. A consistent K factor of 0.66 is determined for a constant C_0. Figure 5.14 shows the normalized moment capacity versus unbraced length for the 50 m span 485 MPa yield strength steel prototype girder. A consistent K factor of 0.68 is determined for a constant C_0. Figure 5.15 shows the normalized moment capacity versus unbraced length for the 50 m span 690 MPa yield strength steel prototype girder. A consistent K factor of 0.66 is determined for a constant C_0.

5.4 Consideration of Inelastic Lateral-Torsional Buckling

The finite difference analysis provides the elastic lateral-torsional buckling moment, either with or without the FRRB. Both slender and stocky webs can be considered by neglecting or retaining the St. Venant torsional resistance. However, the finite difference

analysis method formulated in Section 5.2 does not consider inelastic lateral-torsional buckling. The differential equations used in Section 5.2 do not consider inelastic behavior.

The AASHTO LRFD (1994) Bridge Design Specifications provide approximate results for inelastic buckling. On a graph of lateral-torsional buckling moment versus unbraced length, a straight line extends between two critical unbraced lengths. The first length is the plastic length, L_p, defined by Equation 2.12. At this unbraced length and less, the yield moment is taken as the lateral-torsional buckling moment. The second length is the transition length, L_r, defined by Equation 2.13. At this unbraced length, one half of the yield moment is taken as the lateral-torsional buckling moment. The straight line defines the remaining inelastic buckling resistance between these two unbraced lengths. For an unbraced length greater than L_r, the capacity is an elastic lateral torsional buckling capacity.

To determine the inelastic lateral-torsional buckling capacity of the prototype girders, the AASHTO LRFD design specifications (Equations 2.14 and 2.15) were used with the K factors determined from the finite difference analyses in which the webs were assumed to be slender. The prototype girders have webs that are slender for the construction stage. Also, inelastic lateral-torsional buckling is considered only for girders with slender webs by the AASHTO LRFD specifications. With a consistent K factor, an effective unbraced length can be used in Equations 2.14 and 2.15 to determine the lateral-torsional buckling moment. The following equation determines the effective length, L_{eff}:

$$L_{eff} = KL_b^{FRRB} \qquad \text{(Eq. 5.24)}$$

The K factors were determined from the finite difference analyses in which the web was assumed to be slender. L_{eff} was used in Equations 2.14 and 2.15 with the load shedding factor, R_b, to generate curves of lateral-torsional buckling moment versus unbraced length for the prototype girders. Also, L_b^{FRRB} was used in Equations 2.14 and 2.15 without the K factor

and with R_b to generate curves of lateral-torsional buckling versus unbraced length. The factored construction stage design moment is also with the curves to illustrate how the original unbraced lengths (diaphragm spacing without FRRBs) and the effective unbraced length (considering the increased diaphragm spacing with the FRRBs) meet the design criteria.

Figure 5.16 shows the lateral-torsional buckling moment versus unbraced length for the 33.5 m span 485 MPa yield strength steel girder. Figure 5.17 shows the lateral-torsional buckling moment versus unbraced length for the 33.5 m span 690 MPa yield strength steel girder. For both 33.5 m span girders, the factored construction stage design moment is 4,688 kN-m (3,458 kip-ft). With the original unbraced length of 5.86 m (19.23 ft) and no FRRBs, the lateral-torsional buckling moment is 5,266 kN-m (3,884 kip-ft) for the 485 MPa girder and 4,994 kN-m (3,683 kip-ft) for the 690 MPa girder. For the increased unbraced length of 9.05 m (29.68 ft) with FRRBs (and considering K), the lateral-torsional buckling moment is 5,164 kN-m (3,809 kip-ft) for the 485 MPa girder and 4,867 kN-m (3,590 kip-ft) for the 690 MPa girder. For both girders, the lateral-torsional buckling moment at the new unbraced length with FRRBs is slightly below the moment at the original unbraced length without FRRBs.

Figure 5.18 shows the lateral-torsional buckling moment versus unbraced length for the 50 m span 485 MPa yield strength steel girder. Figure 5.19 shows the lateral-torsional buckling moment versus unbraced length for the 50 m span 690 MPa yield strength steel girder. For both 50 m span girders, the factored construction stage design moment is 10,430 kN-m (7,693 kip-ft). With the original unbraced length of 7.2 m (23.62 ft) and no FRRBs, the lateral-torsional buckling moment is 11,283 kN-m (8,322 kip-ft) for the 485 MPa girder and 10,638 kN-m (7,846 kip-ft) for the 690 MPa girder. For the increased unbraced length of 11.0 m (36.09 ft) with FRRBs (and considering K), the lateral-torsional buckling moment is 10,868 kN-m (8,016 kip-ft) for the 485 MPa girder and 10,446 kN-m (7,705 kip-ft) for the 690 MPa girder. For both

girders, the lateral-torsional buckling moment at the new unbraced length with FRRBs is slightly below the moment at the original unbraced length without FRRBs.

5.5 Alignment Chart Analysis Method

5.5.1 Introduction

As discussed in Section 3.2.2, the effect of an FRRB on the lateral-torsional buckling of a bridge I-girder is similar to the beam in a braced frame. The compression flange of the girder is similar to a column, when the compression flange bends about the vertical axis of the girder (the strong axis of the flange). With some modifications, the standard methods for determining the effect of beams on the buckling of a column in a braced frame can be utilized to analyze the effects of FRRBs on the lateral-torsional buckling of a bridge I-girder.

The stability of a frame in a building depends on both the columns and the beams. The beams provide a rotational restraint to the ends of the column, if a rigid joint is provided. The length of the column is modified by the effective length factor, K, to account for the rotational restraint provided by the beams in standard buckling solutions for a column with pinned-pinned support conditions.

The ratio of the rotational stiffness of the compression elements (the columns) and the restraining elements (the beams), Ψ, is found at each end of the compression elements. The two ratios are marked on an alignment chart, shown for sidesway inhibited (braced frame) in Figure 5.20. The K factor is defined by the intersection with the K axis of a straight line between Ψ_A and Ψ_B.

There are two standard alignment charts, one for sidesway inhibited and the other for sidesway allowed. In frame structures, sidesway occurs when the lateral bracing system for the frame allows lateral motion of the frame at any floor level (the location of the beams) relative to the base. If the frame is braced against sidesway, the K factor reduces the effective length of

the column. If the frame is not restrained against sidesway, the K factor increases the effective length. Bridge girders are restrained against lateral deflection at the bearings. Furthermore, the locations of diaphragms are assumed to be locations where the lateral deflection of the compression flange is restrained. Thus, the alignment chart for sidesway inhibited is used.

Figure 5.21 compares the lateral deflection of a bridge girder pair with the lateral deflection of a frame. Figure 5.21(a) shows a girder pair with several unbraced lengths. The FRRB in Figure 5.21(a) is bent in single curvature. Figure 5.21(b) shows the sidesway inhibited case for a frame. Figure 5.21(b) also shows the single curvature in the bracing element (the beam) when sidesway is inhibited.

Several assumptions are made regarding the effective length factor for braced frames. These assumptions can be applied to the analysis of the FRRB with some modifications:

(1) the behavior is elastic,
(2) members have constant cross-sections,
(3) the rotations at the ends of the beams are equal in magnitude and produce single curvature in the beams with sidesway inhibited,
(4) joints are rigid,
(5) columns at a joint have restraint provided by the joint distributed in proportion to their I/L ratios, and
(6) columns buckle simultaneously.

Some of these assumptions require additional consideration. Regarding elastic behavior, most bridge I-girders are proportioned to buckle inelastically. The alignment charts can be adapted to use for inelastic buckling of girders as discussed in the previous section. A long bridge girder often has changes in dimensions over the length of the girder to economize the design. The changes affect the stiffness of the compression flange. The compression element stiffness of interest is based on the moment of inertia of the compression flange about the vertical axis of the flange. Thus, a change in the flange thickness has little effect on this

stiffness. However, since the second assumption does not generally apply to bridge girders, the stiffness of the compression flange should be carefully considered. To calculate a conservative value of the *K* factor, the stiffness of the compression flange should not be underestimated.

The joint between the compression flange and the FRRB should be as rigid as possible. The joint may be welded or bolted. A bolted connection allows the connection to be made in the field without field welds. The bolted connection must provide sufficient rotational restraint.

Regarding the assumption that all columns buckle simultaneously, the finite element analyses discussed in Chapter 6 indicate that the compression elements do buckle simultaneously.

5.5.2 Analysis Procedure

The alignment chart analysis method is intended to be a simpler way to determine *K* factors than the finite difference analysis method. For frames, the ratio Ψ relates the rotational stiffness of a column with that of the connecting beams. The ratio Ψ is modified for a bridge I-girder with FRRBs. For the compression flange of the girder, only the moment of inertia of the flange about the vertical axis, I_{yc}, is considered. The rotational restraint provided by the FRRB is determined from the elastic modulus, moment of inertia and length of the FRRB components. The stiffness ratio Ψ has the following form:

$$\Psi = \frac{\sum \left(EI_{yc} / L_b \right)_{compression}}{\sum \left(E_f I_{yf} / L_s \right)_{brace}} \qquad \text{(Eq. 5.25)}$$

The moment of inertia of the compression flange is assumed to have no contribution from the web. When the web is stocky, the AASHTO LFRD design specifications allow one-third of the web depth in compression to contribute to I_{yc}. Including the web, I_{yc} is calculated as:

$$I_{yc} = \frac{b_{tf}^3 t_{tf}}{12} + \frac{D_c t_w^3}{36} \cong \frac{b_{tf}^3 t_{tf}}{12} \qquad \text{(Eq. 5.26)}$$

However, the contribution from the web is negligible since the web thickness is much smaller than the flange width. Hence, I_{yc} is calculated for the flange only. In a similar fashion, the moment of inertia of the FRRB, I_{yf}, is the moment of inertia of the main FRRB component about the vertical axis.

Figure 5.22 shows a portion of the compression flange of a girder divided into three unbraced lengths. Points A, B, C, and D are the joints where the FRRB are attached. The unbraced lengths for each segment is labeled as L_{b1}, L_{b2}, and L_{b3}, respectively. For segment 2 shown in Figure 5.21, Equation 5.25 can be simplified when the FRRB is on only one side of the girder (i.e., only one FRRB attaches at each joint). The elastic modulus can also be eliminated if elastic behavior is assumed and if all elements are steel. The moment of inertia for the compression flange is assumed to remain constant along the length of the flange. When the nomenclature from Figure 5.22 is used, Equation 5.25 evaluated at point B reduces to the following:

$$\Psi_B = \frac{I_{yc} L_s}{I_{yf}} \left(\frac{1}{L_{b1}} + \frac{1}{L_{b2}} \right) \qquad \text{(Eq. 5.27)}$$

If the required K factor is known, the required ratio Ψ at both ends of the segment can be found. For segment 2 from Figure 5.22, the ratio Ψ at each end will be the same if segments 1 and 3 have the same length and moment of inertia. If segment 1 and 3 have different lengths or moments of inertia, then Ψ will not be the same for both ends of segment 2.

When Ψ is the same at both ends of an unbraced length, the determination of the required FRRB dimensions is simplified. Ψ for both ends can be determined for a given K factor by a horizontal line on Figure 5.20. Then the unknowns in Ψ can be determined by rearranging Equation 5.25. Typically the unknown in Ψ will be a FRRB dimension, such as I_{yf}.

With the K factor and the FRRB dimensions known, the moment capacity of all of the unbraced segments should be calculated and verified against the maximum demand moment in that segment. The stiffness of the FRRB and unbraced lengths should be used to calculate Ψ at both ends of each segment. The effective length, L_{eff}, of each segment should be determined using Equation 5.20 and the K factor from the alignment chart.

The effective length is then used to determine the lateral-torsional buckling moment capacity using the AASHTO LRFD design specifications as discussed in Section 5.4. Since most unbraced segments will not have uniform moment, the moment distribution factor C_b can be applied as appropriate. Under a uniform construction loading, most unbraced lengths of simply supported bridge girders will have a bending moment less than the maximum demand moment at the midspan. With this reduced demand moment and using the moment distribution factor, C_b, the unbraced lengths near the end of the girder can be increased substantially larger than near the midspan.

5.5.3 Alignment Chart Analysis of Prototype Girders

In the Section 5.3, the prototype girders with FRRBs were analyzed for a range of unbraced lengths using the finite difference analysis method. From the results of those analyses, K factors for the girders with FRRBs were determined. The alignment chart method is expected to be a simpler and less rigorous method than the finite difference analysis method. The unbraced lengths (diaphragm spacing) designed for the prototype girders (Figure 5.2) are the only unbraced lengths considered in the alignment chart analysis.

The unbraced lengths shown in Figure 5.2 were used in the alignment chart analysis. The cross-section dimensions of the prototype girders from Table 5.1, and the FRRB dimensions from Table 5.2 were also used. Ψ values were determined for the joints at either end of the unbraced lengths of the prototype girders. The K factors were determined using the

Ψ values and Figure 5.20. Table 5.3 lists the K factors for the principal unbraced lengths (interior) and the other unbraced lengths of the prototype girders. Also listed are the C_b values for the interior and other unbraced lengths.

5.6 Summary

This chapter presented methods for determining the lateral-torsional buckling resistance of bridge I-girders with FRRBs. Each of the two analysis methods provide effective length (K) factors which can be used with the AASHTO LRFD design specifications to account for inelastic buckling or web slenderness effects. If the girder is controlled by elastic buckling, the finite difference analysis method could be used to determine the lateral-torsional buckling resistance directly. Table 5.4 lists the K factors from the two analysis methods. The K factors from the alignment chart method are slightly less than those from finite difference analysis method. This would indicate that the alignment chart method gives results slightly less conservative than the results of the finite difference analysis method.

Table 5.5 compares the factored construction stage demand moments to the lateral-torsional buckling moment capacities determined using the AASHTO equations with K factors from Table 5.4. The K factors in Table 5.4 are used with the appropriate unbraced length to determine the lateral-torsional buckling moment. The lateral-torsional buckling moment determined using K factors from the finite difference analysis method for girders with diaphragms with FRRBs and increased unbraced lengths is less than the lateral-torsional buckling moment for girders with standard diaphragms at the original spacing. The lateral-torsional buckling moment determined using the K factors from the alignment chart method for girders with diaphragms with FRRBs and increased unbraced lengths is slightly greater than the lateral-torsional buckling moment for the girders with standard diaphragms at the original spacing.

The finite difference analysis was an effective method for determining the lateral-torsional buckling moment. The finite difference analysis was performed on the principal unbraced length of each prototype girder. The set-up of the simultaneous equations can be complicated for the number of points necessary to get accurate results. The solution of the simultaneous equations is simplified by using a computer to solve for the lateral-torsional buckling moment. If the unbraced length is not symmetric, then both halves of the unbraced length would have to be included in the finite difference model. Hence, unbraced lengths near the ends of the girder span require a reformulation of the finite difference model and the matrices.

The alignment chart analysis method was a simple method for determining the lateral-torsional buckling moment. The alignment chart analysis method is easily used by practicing engineers. Unlike the finite difference analysis, the alignment chart analysis is not complicated by unequal end conditions. The results from the alignment chart method are approximate, and appear to be less conservative than the results of the finite difference analysis method.

The diaphragm spacing in a steel I-girder bridge can be increased using FRRBs. The amount of the increase depends on the bending moment in that part of the girder. For the interior regions of the girder, the use of FRRBs can increase the diaphragm spacing by 50 to 60 percent in the region of the highest moment. When the original configuration of diaphragms is evenly spaced over the span, the diaphragm spacing near the bearings of a simply supported girder can be increased by over 100 percent.

Table 5.1 Dimensions of prototype girder cross-sections

Span Length	F_y (MPa)	b_{tf} (mm)	t_{tf} (mm)	D (mm)	t_w (mm)	b_{bf} (mm)	t_{bf} (mm)
33.5 m	485	325	25	1475	10.5	375	30
	690	325	25	1250	9.5	325	30
50 m	485	425	30	1890	13.5	425	40
	690	375	37.5	1700	12	400	37.5

Table 5.2 Dimensions of FRRBs

Span Length	FRRB Length	Interior FRRB		Support End FRRB	
		Width, b	Thickness, t	Width, b	Thickness, t
33.5 m	3.92 m	335 mm	50 mm	335 mm	25 mm
50 m	3.92 m	400 mm	55 mm	200 mm	55 mm

Table 5.3 Results of alignment chart analysis

Span Length	F_y (MPa)	*K* Factor		C_b Factor	
		Interior	End	Interior	End
33.5 m	485	0.64	0.64	1.0	1.75
	690	0.64	0.64	1.0	1.75
50 m	485	0.66	0.72	1.0	1.75
	690	0.65	0.72	1.0	1.75

Table 5.4 Results of analysis methods

Span	F_y (MPa)	M_y (kN-m)	*K* Factor		
			Finite Difference with *J*	Finite Difference without *J*	Alignment Chart
33.5 m	485	7,935	0.66	0.66	0.64
	690	8,861	0.66	0.66	0.64
50 m	485	16,099	0.68	0.68	0.66
	690	20,485	0.66	0.66	0.65

Table 5.5 Critical lateral-torsional buckling moment comparisons

Span	F_y (MPa)	Design Moment (kN-m)	Lateral-torsional Buckling Moment (kN-m)		
			Original L_b $K = 1$	L_b^{FRRB} - *K* from Finite Difference	L_b^{FRRB} - *K* from Alignment Chart
33.5 m	485	4,688	5,266	5,164	5,336
	690	4,688	4,994	4,867	5,081
50 m	485	10,430	11,283	10,868	11,390
	690	10,430	10,638	10,446	11,183

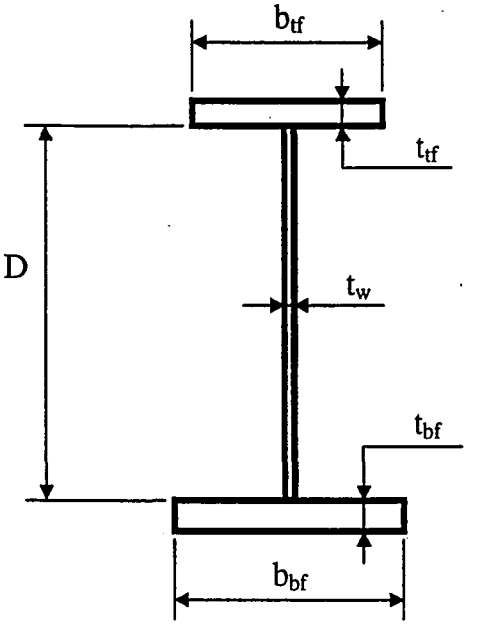

Figure 5.1 Cross-section of girder

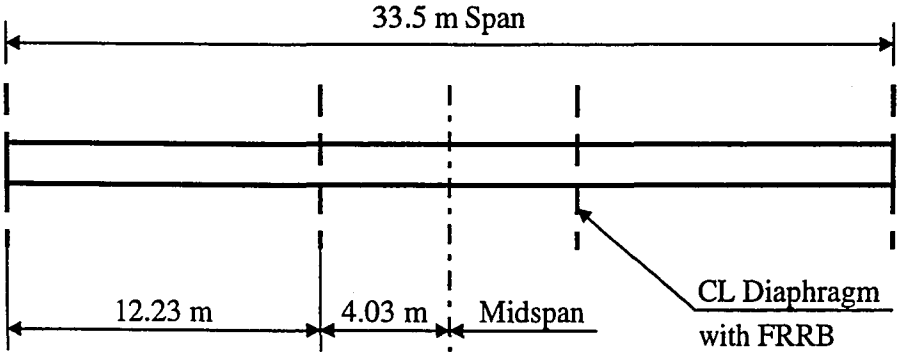

(a) 33.5 m span girders

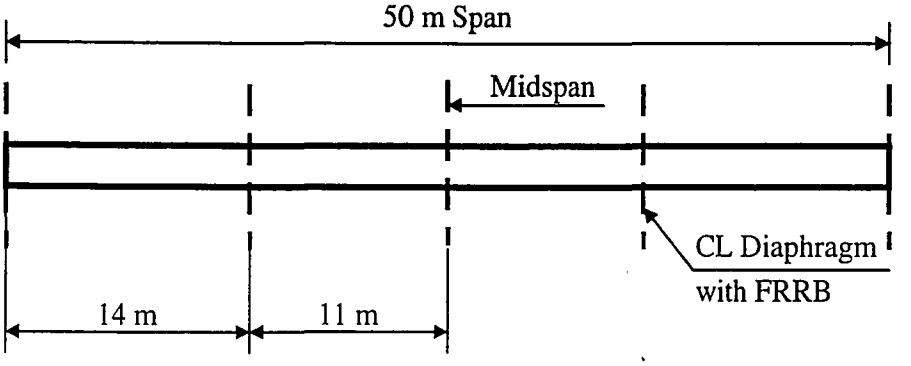

(b) 50 m span girders

Figure 5.2 Locations of diaphragms with FRRBs

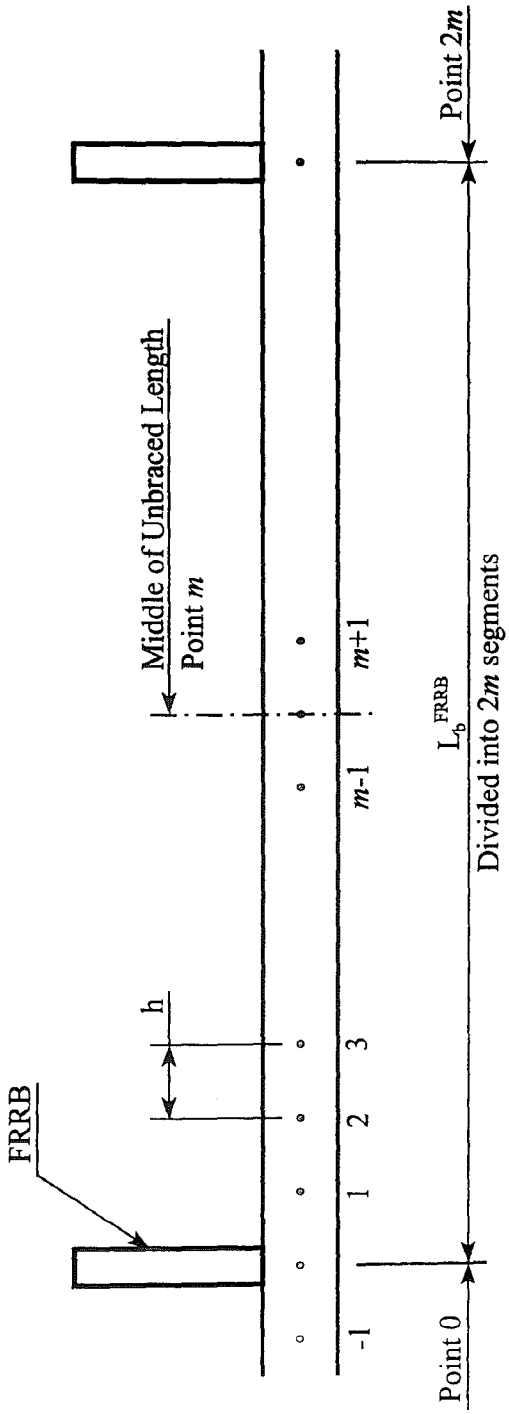

Figure 5.3 Discretization of unbraced length for finite difference analysis

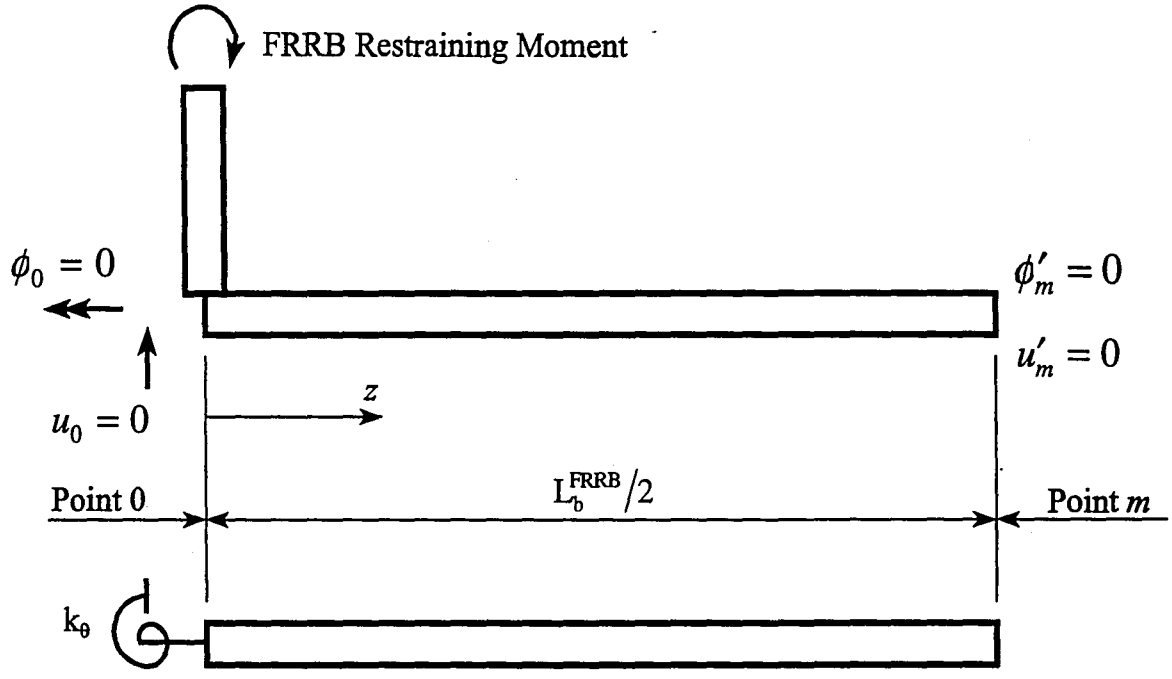

Figure 5.4 Boundary conditions for finite difference analysis

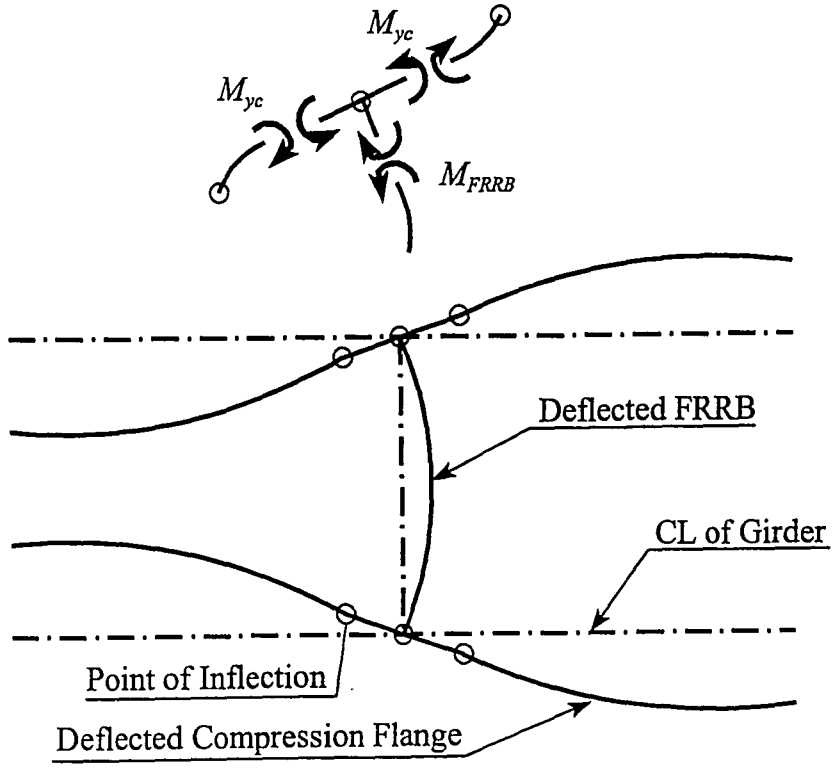

Figure 5.5 Deflected shape of portion of girder pair with FRRB

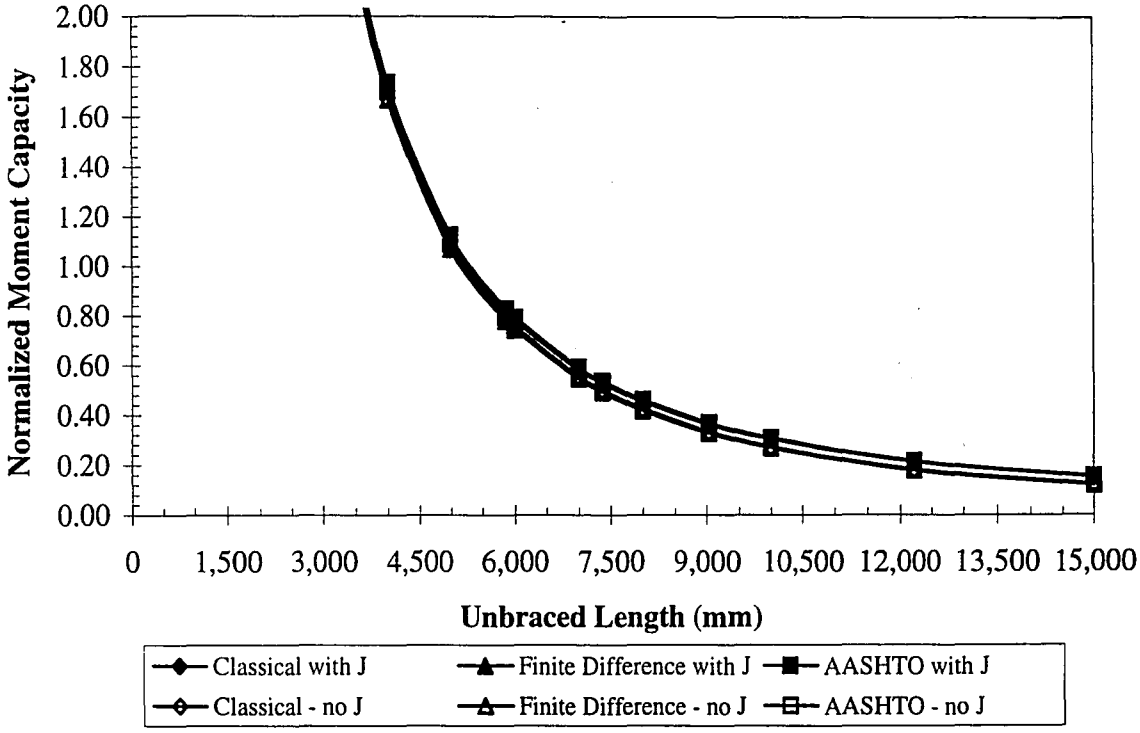

Figure 5.6 Comparison of AASHTO, classical, and finite difference solutions for 33.5 m span 485 MPa yield strength steel girder

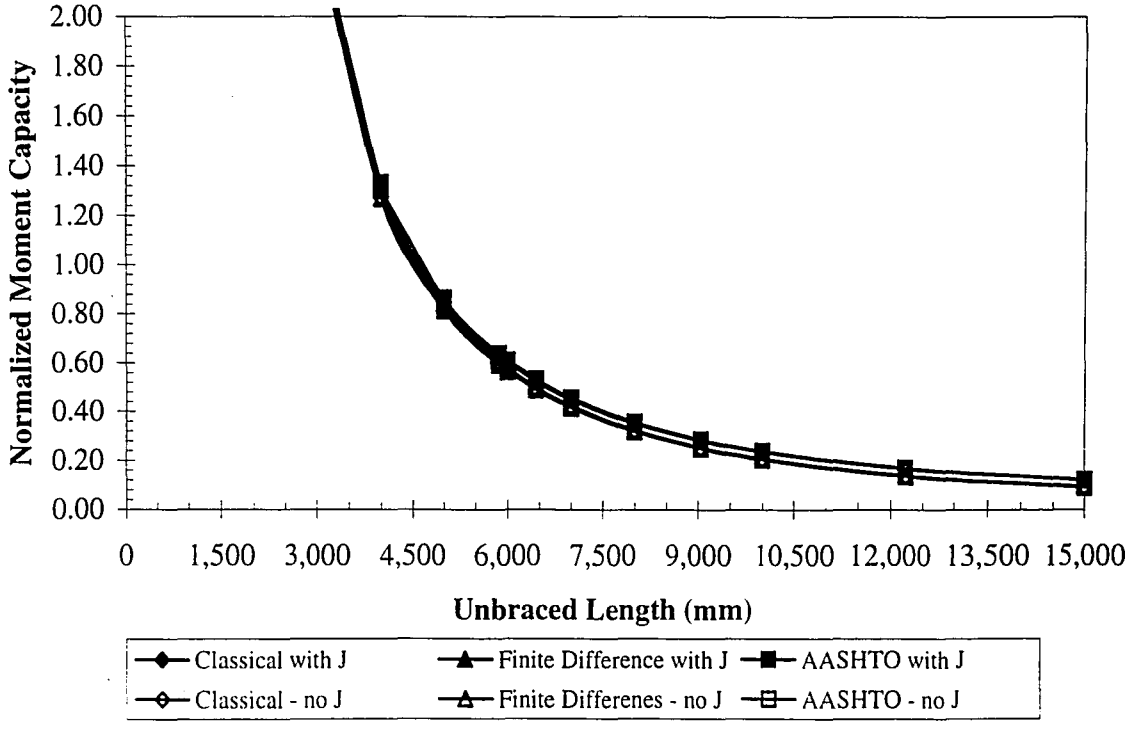

Figure 5.7 Comparison of AASHTO, classical, and finite difference solutions for 33.5 m span 690 MPa yield strength steel girder

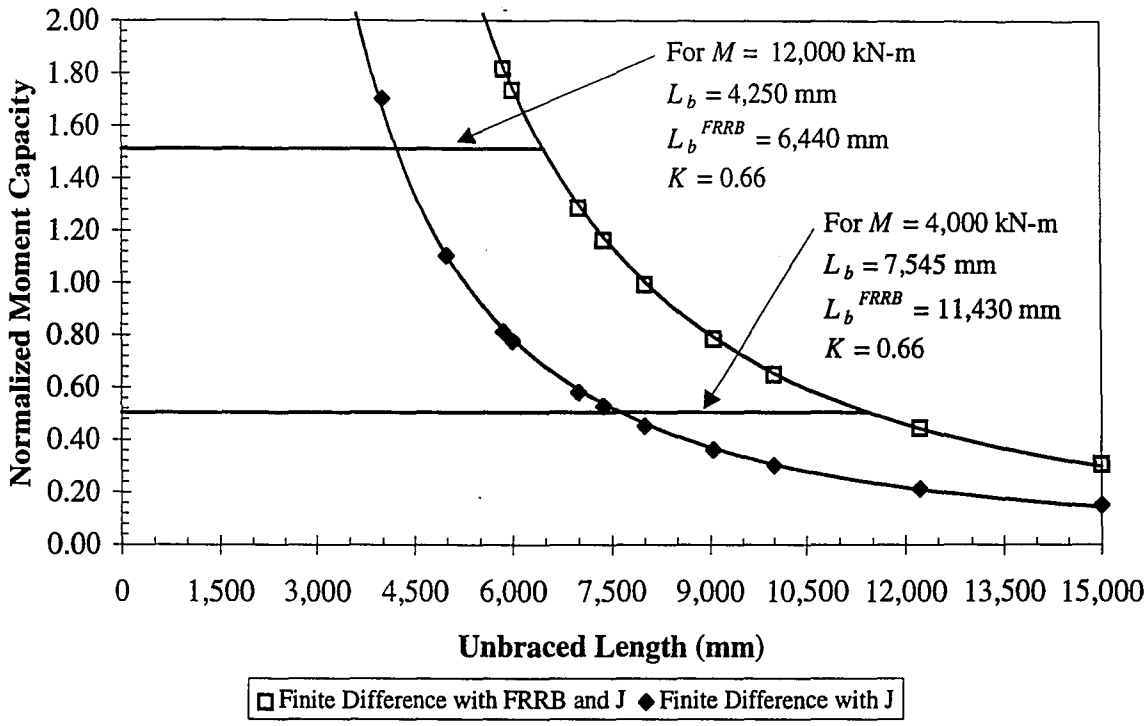

Figure 5.8 Comparison of finite difference solutions for L_b and L_b^{FRRB} with J included for 33.5 m span 485 MPa yield strength steel girder

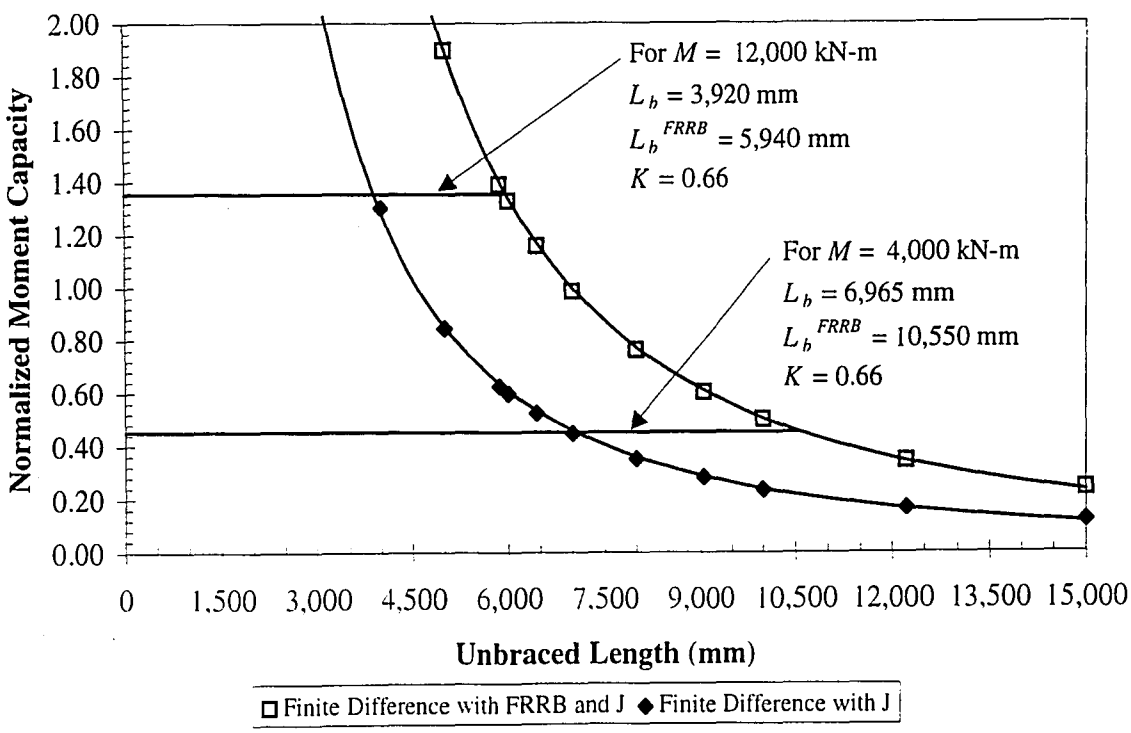

Figure 5.9 Comparison of finite difference solutions for L_b and L_b^{FRRB} with J included for 33.5 m span 690 MPa yield strength steel girder

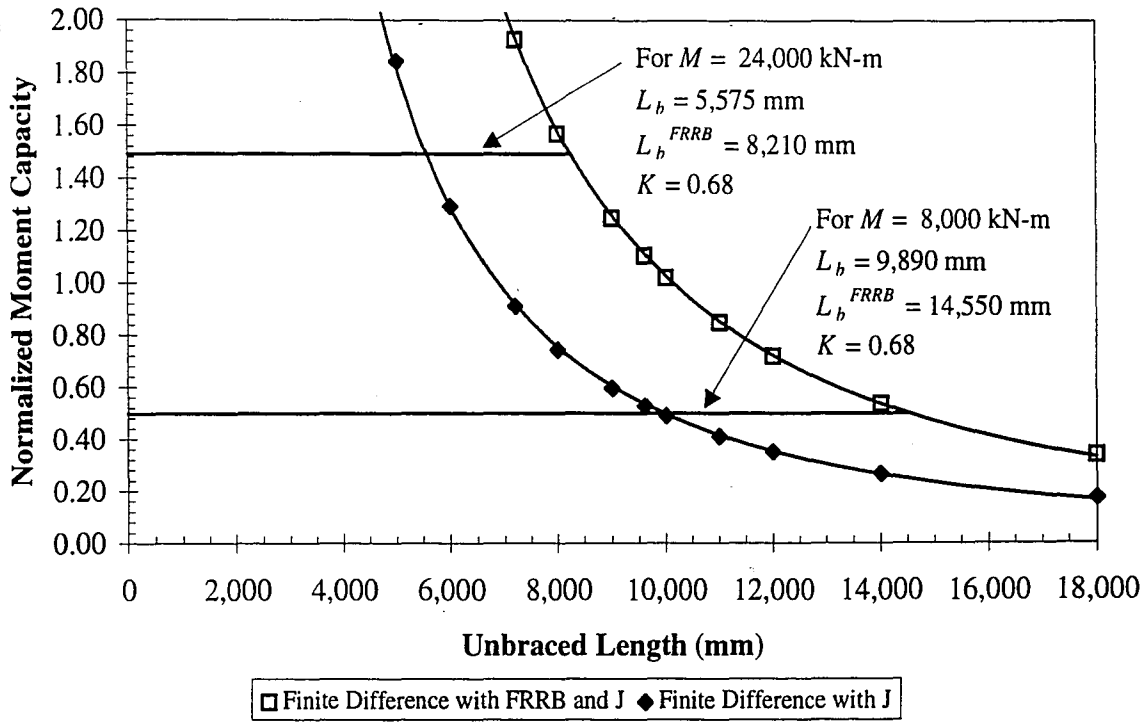

Figure 5.10 Comparison of finite difference solutions for L_b and L_b^{FRRB} with J included for 50 m span 485 MPa yield strength steel girder

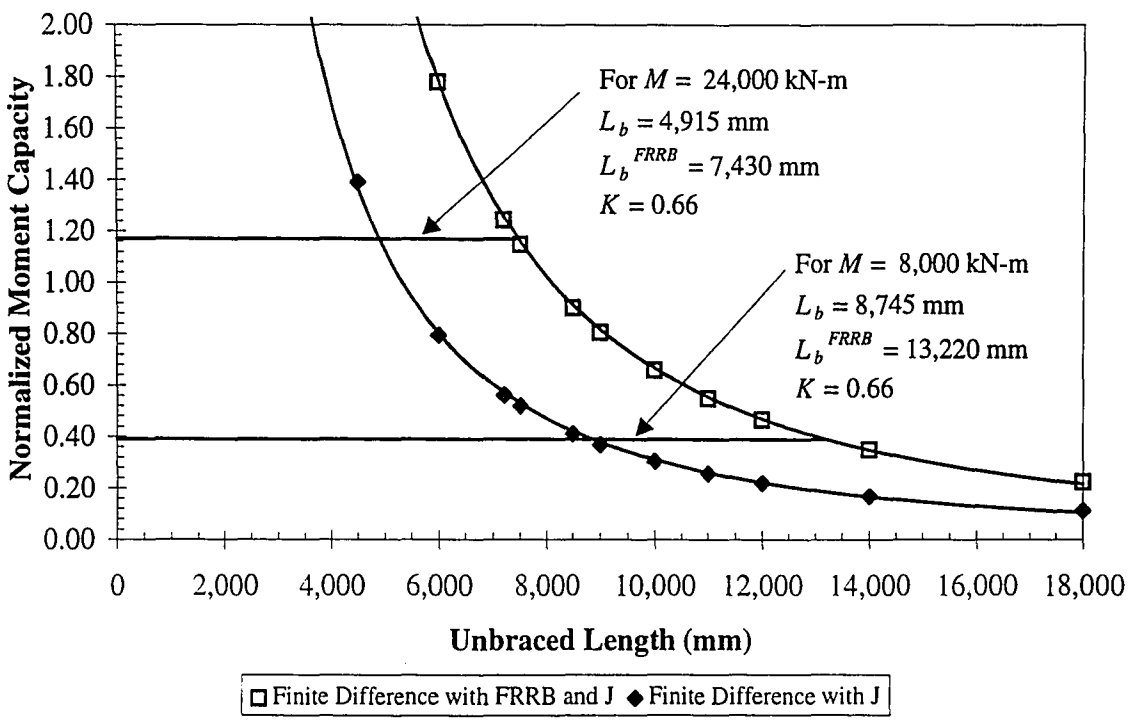

Figure 5.11 Comparison of finite difference solutions for L_b and L_b^{FRRB} with J included for 50 m span 690 MPa yield strength steel girder

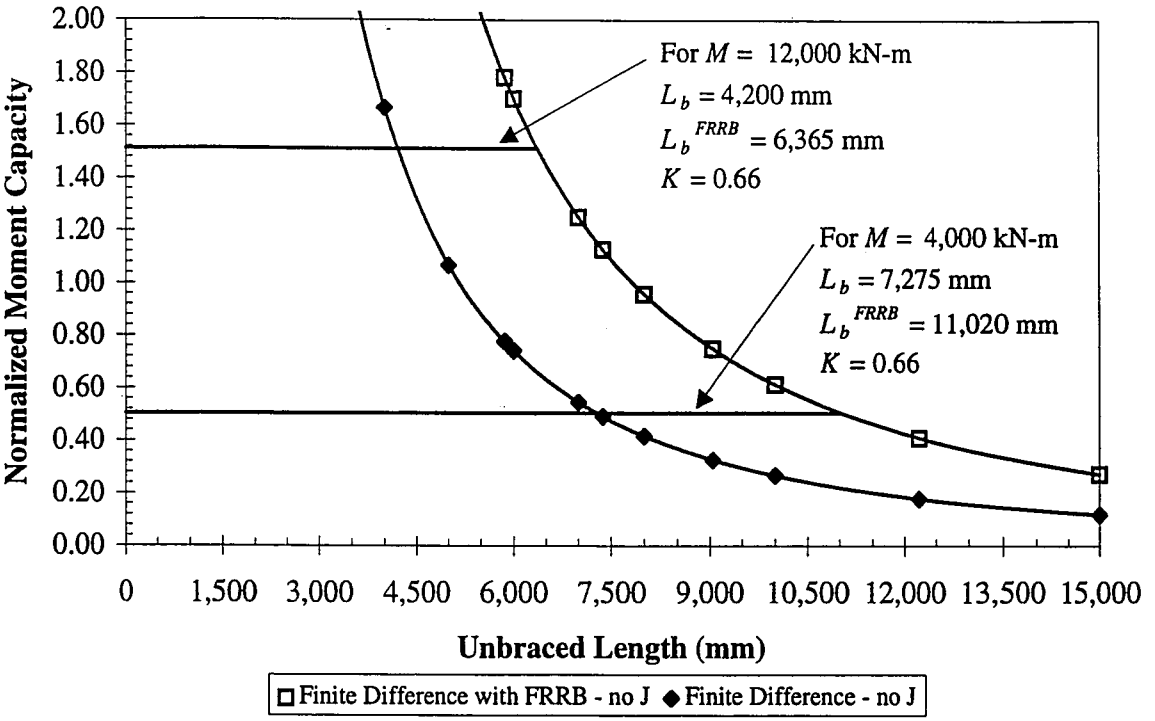

Figure 5.12 Comparison of finite difference solutions for L_b and L_b^{FRRB} without J for 33.5 m span 485 MPa yield strength steel girder

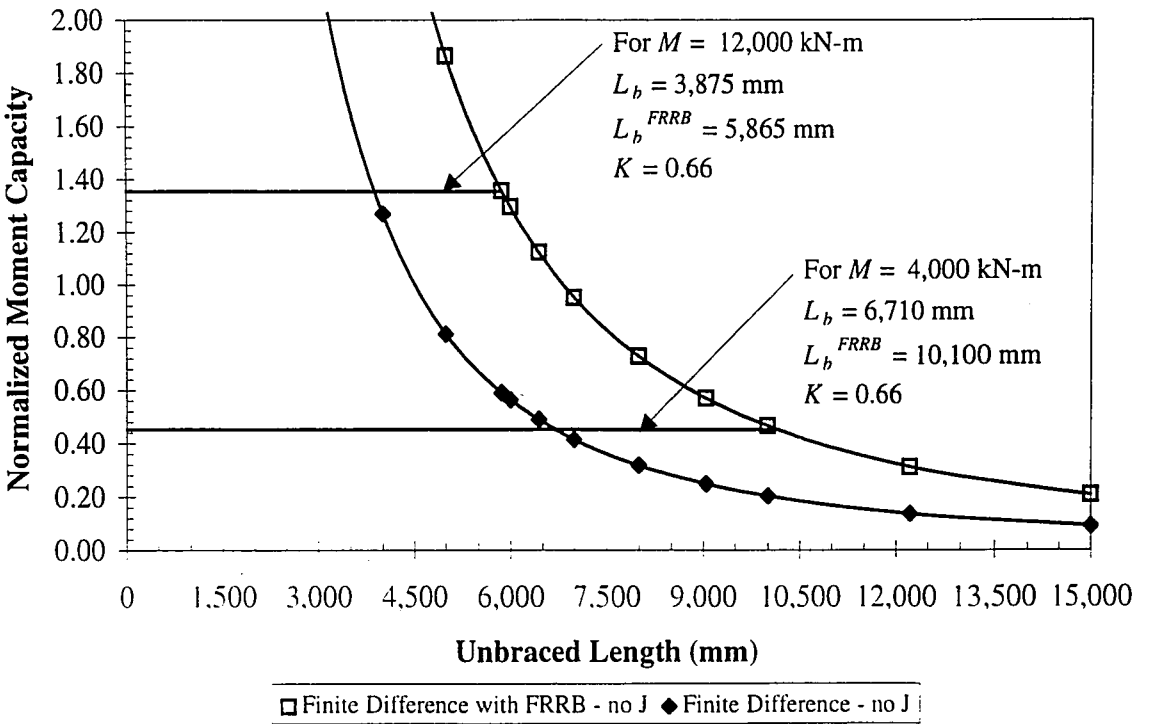

Figure 5.13 Comparison of finite difference solutions for L_b and L_b^{FRRB} without J for 33.5 m span 690 MPa yield strength steel girder

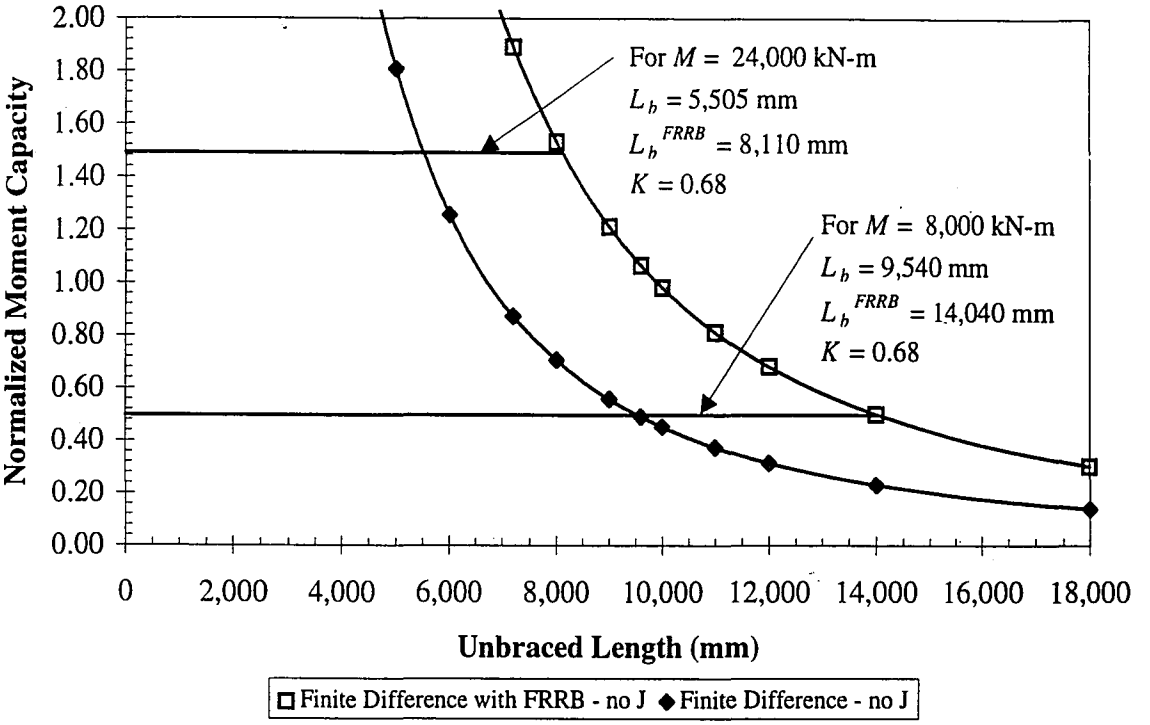

Figure 5.14 Comparison of finite difference solutions for L_b and L_b^{FRRB} without J for 50 m span 485 MPa yield strength steel girder

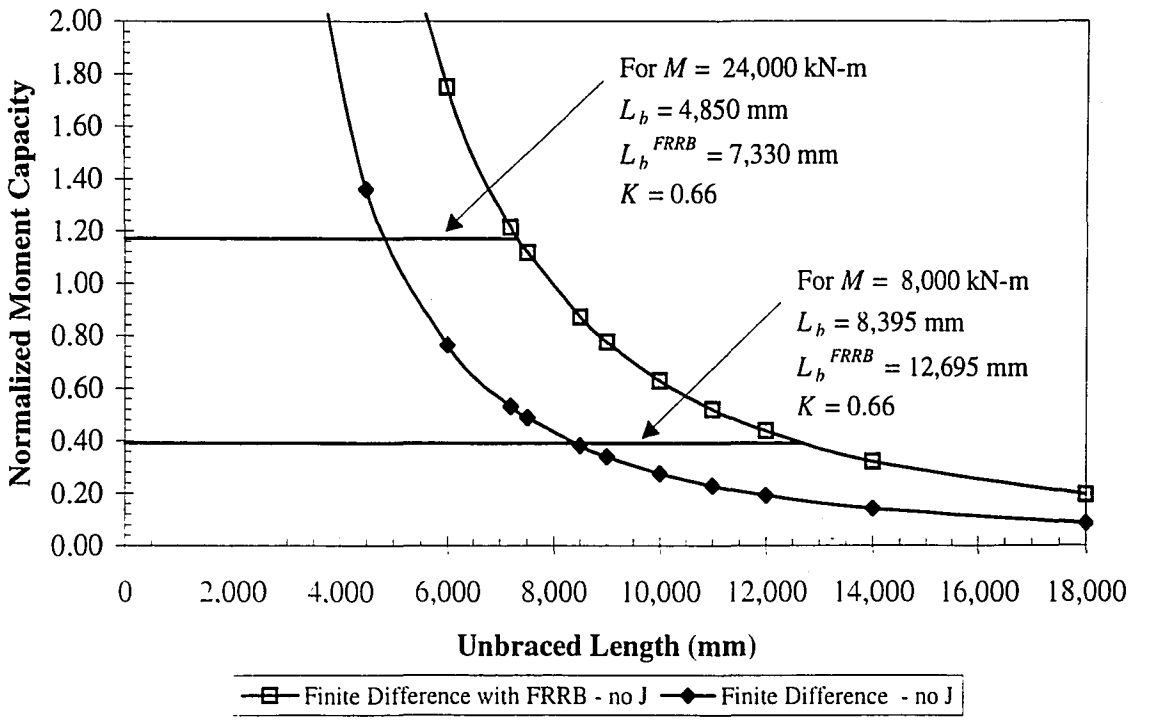

Figure 5.15 Comparison of finite difference solutions for L_b and L_b^{FRRB} without J for 50 m span 690 MPa yield strength steel girder

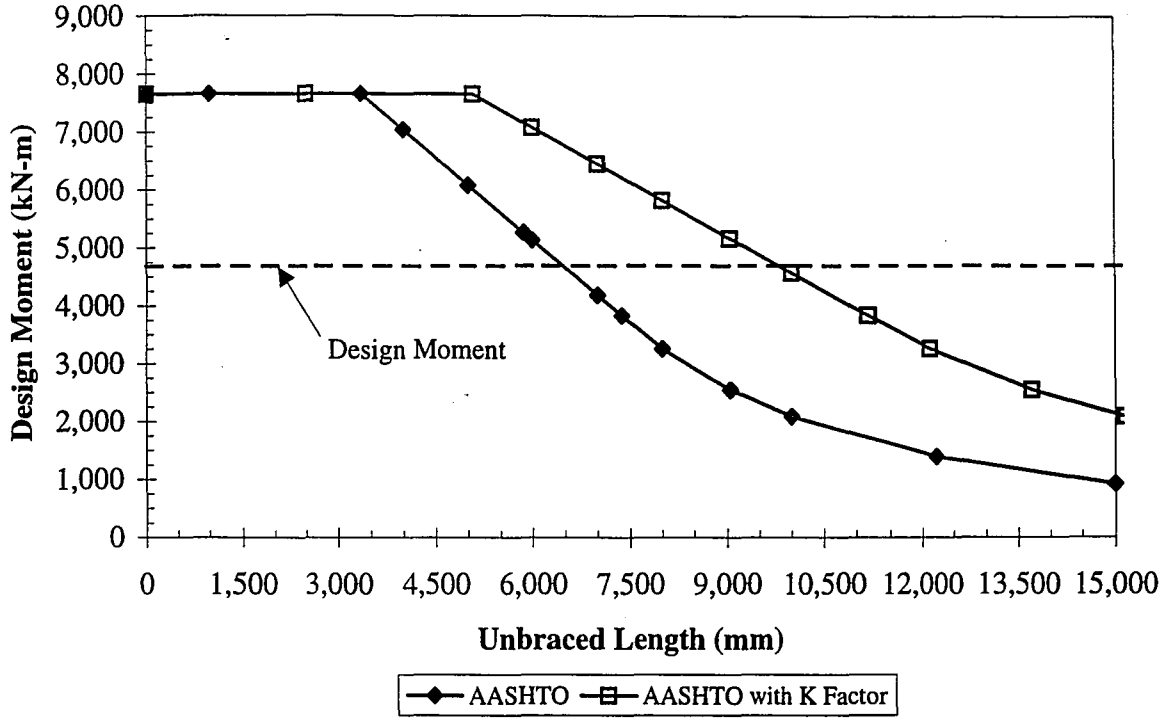

Figure 5.16 Comparison of AASHTO design limits with and without *K* factor for 33.5 m span 485 MPa yield strength steel girder

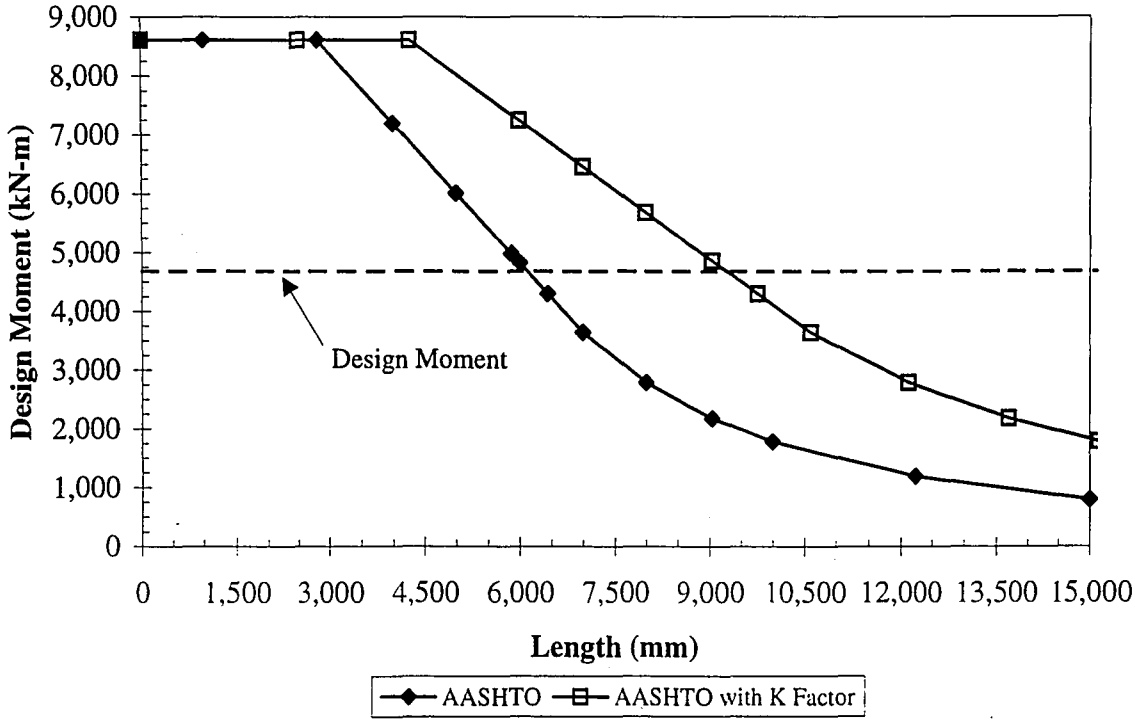

Figure 5.17 Comparison of AASHTO design limits with and without *K* factor for 33.5 m span 690 MPa yield strength steel girder

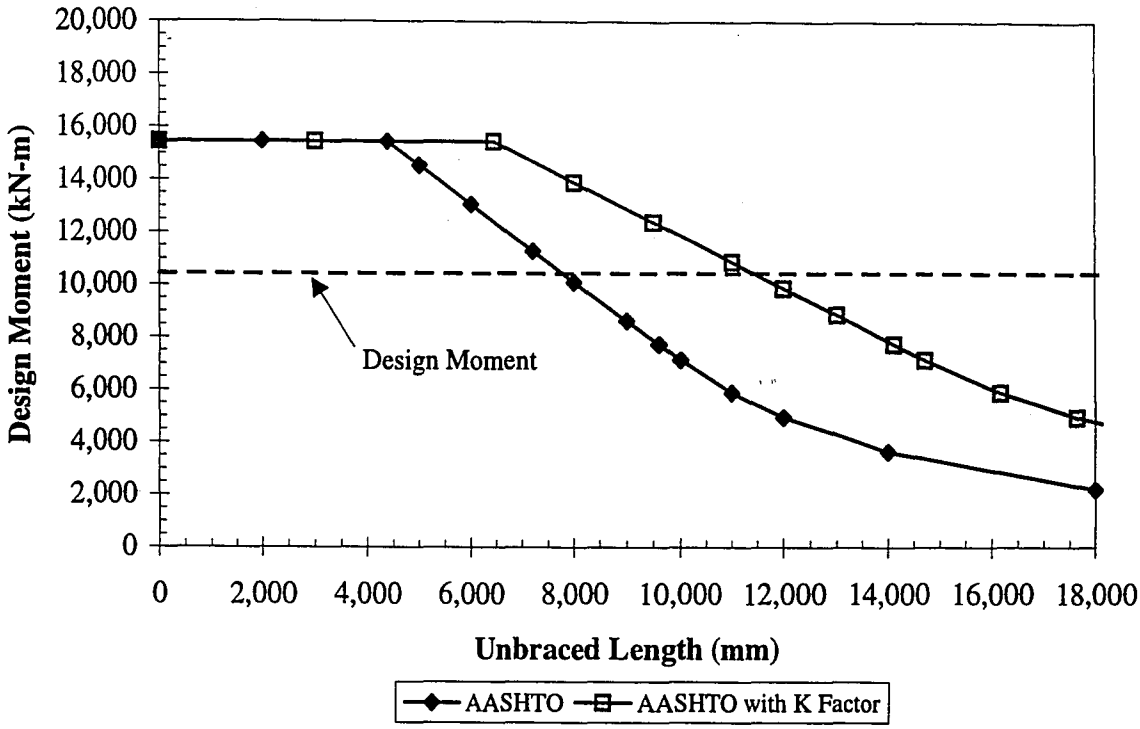

Figure 5.18 Comparison of AASHTO design limits with and without *K* factor for 50 m span 485 MPa yield strength steel girder

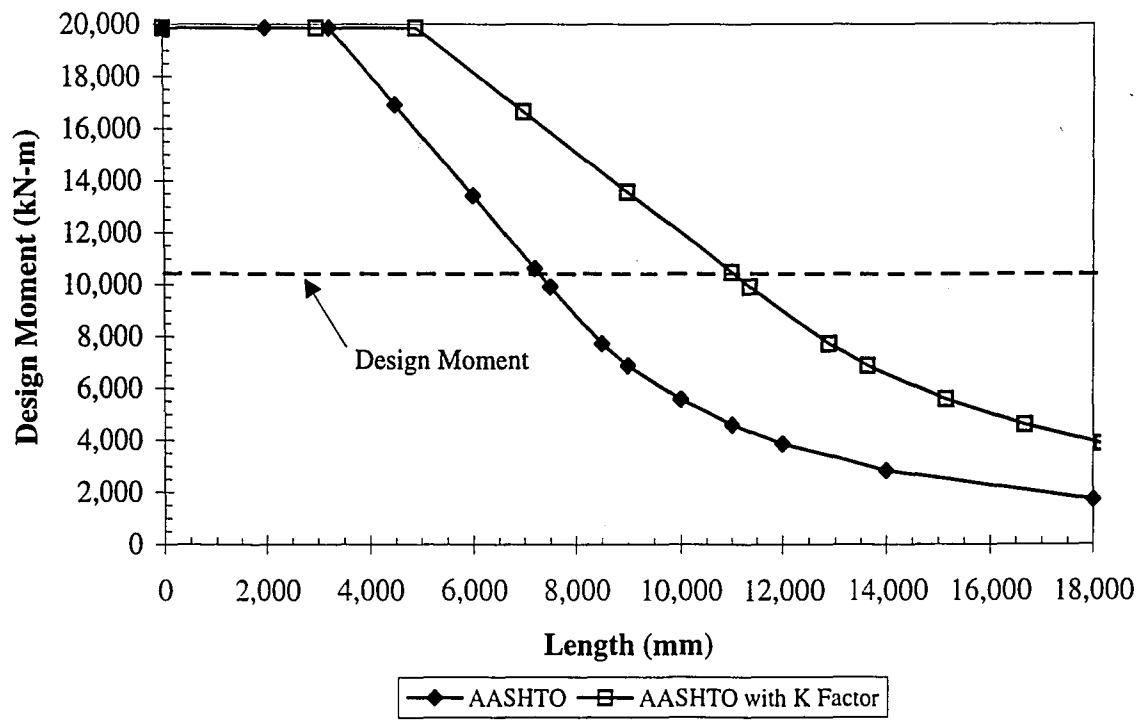

Figure 5.19 Comparison of AASHTO design limits with and without *K* factor for 50 m span 690 MPa yield strength steel girder

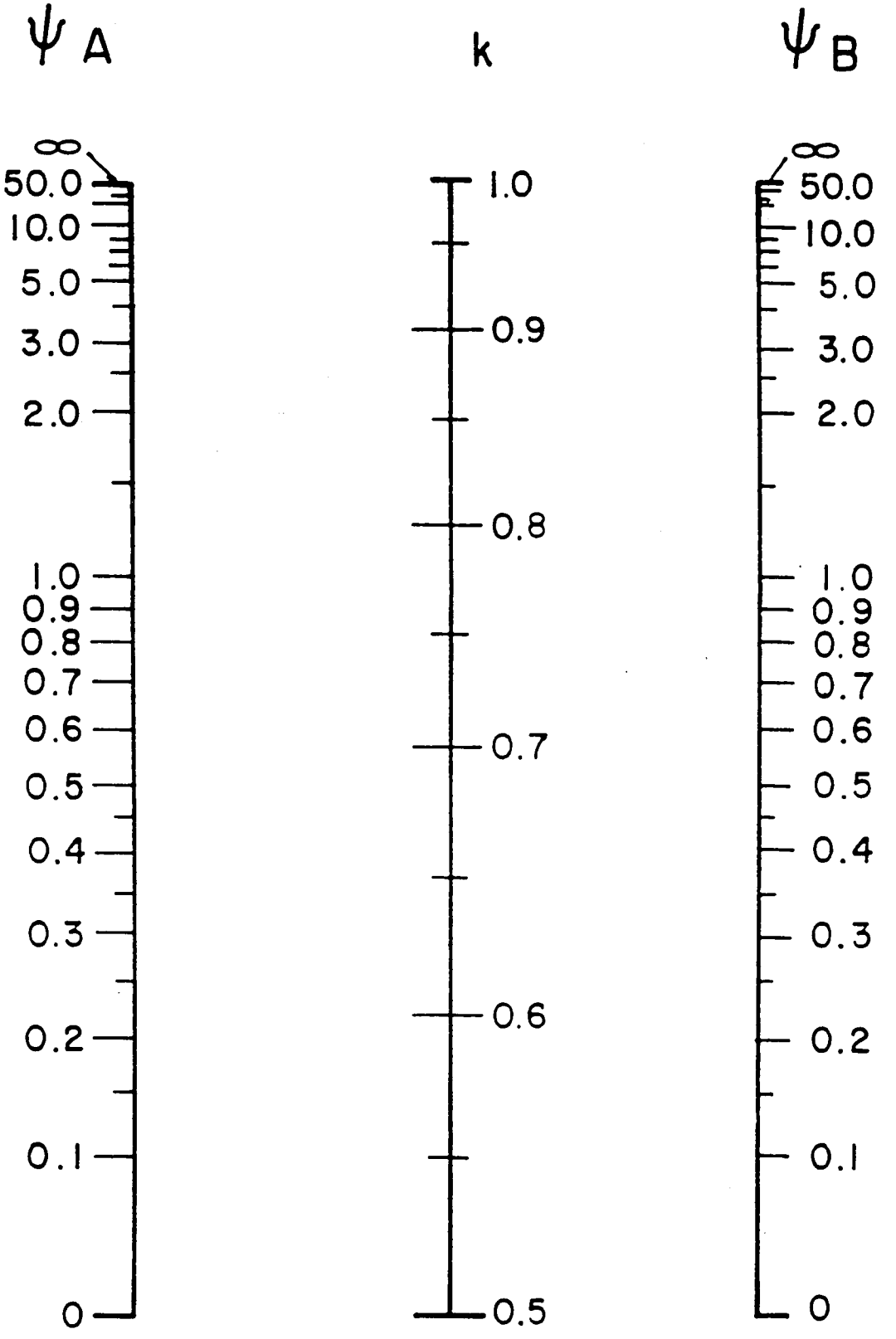

Figure 5.20 Alignment chart with sidesway inhibited (adapted from ACI (1995))

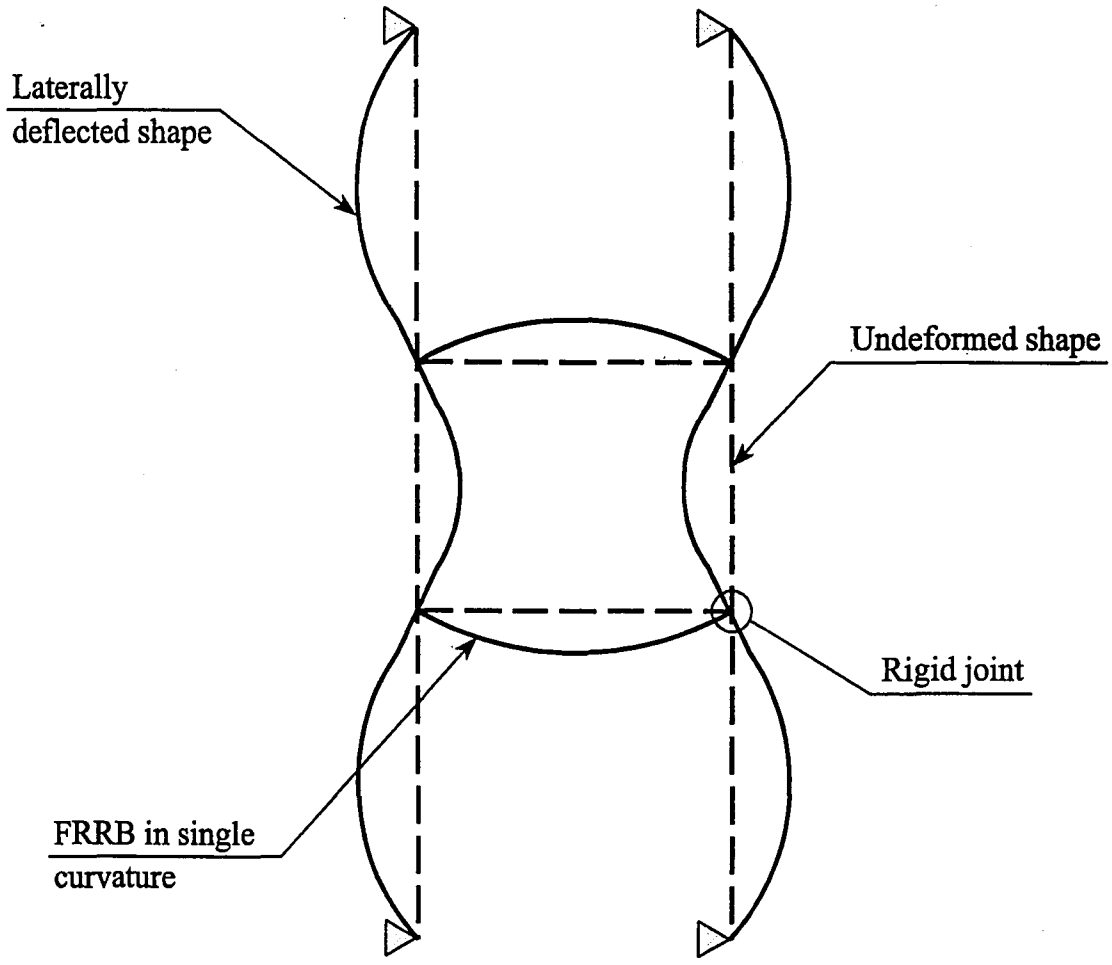

(a) Plan of girder pair laterally buckling

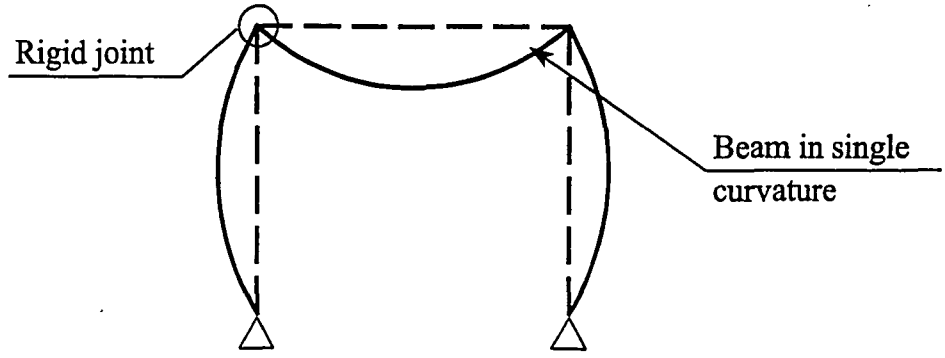

(b) Elevation of braced frame (sidesway inhibited)

Figure 5.21 Lateral deflection of girder pair and braced frame

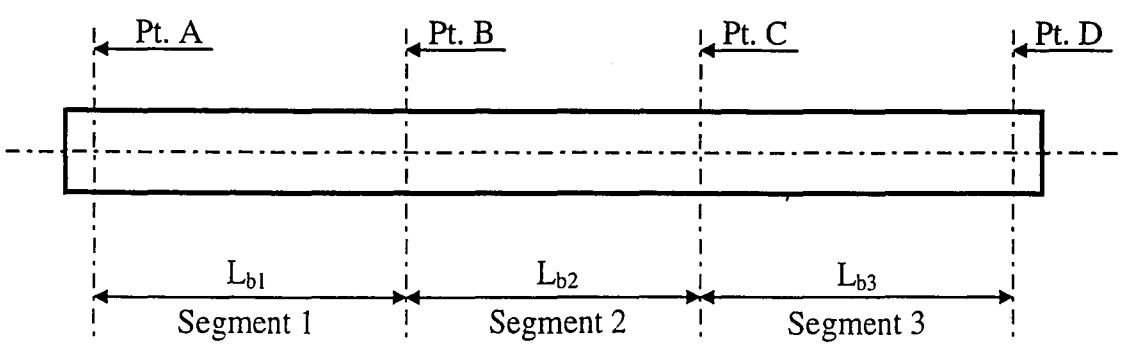

Figure 5.22 Joints and unbraced lengths for alignment chart analysis

6. Finite Element Analysis of Girders with Flange Rotational Restraint Braces

6.1 Introduction

Finite element analyses were conducted to investigate the behavior of girders with flange rotational restraint braces. This behavior was compared to the behavior of girders with standard diaphragm configurations. Both the original unbraced lengths (diaphragm spacing), shown in Figure 2.7, and the increased unbraced lengths (diaphragm spacing with FRRBs), shown in Figure 5.2, were investigated. The prototype girders discussed in Chapter 5 were utilized. The results of the finite element analysis were used to verify the effectiveness of the analysis methods discussed in Chapter 5.

The four prototype girders include two different spans, 33.5 m (110 ft) and 50 m (164 ft), and two different high performance steels with yield strengths of 485 MPa (70 ksi) and 690 MPa (100 ksi). The cross-section dimensions are listed in Table 5.1. Figure 5.1 details the terminology for the cross-sections.

Table 5.2 lists the dimensions of the FRRB utilized in the finite element analysis of the prototype girders with FRRBs. The alignment chart analysis method discussed in Section 5.4 was used to determine the dimensions of the FRRBs for each of the prototype girders. Figure 6.1 shows the arrangement of the FRRBs on half of the 33.5 m span. Figure 6.2 shows the arrangement of the FRRBs on half of the 50 m span. The finite element analysis allows FRRBs to be modeled as a member of the structure rather than as discrete springs.

6.2 Finite Element Models of Prototype Girders

The finite element analysis models discussed in Chapter 4 served as the basis for the finite element models. Two basic finite element models were created. The first basic model was for the 33.5 m (110 ft) span. The second basic model was for the 50 m (164 ft) span. The basic models were modified to account for the widths and thicknesses of the component plates of the

I-girders, the steel properties, and the type of bracing. The prototype girders are symmetric about the midspan so only half of the span was included in each model.

The half-span models for the 33.5 m span include 100 elements along the length. The length of each element is 167.5 mm (6.59 inches). Each flange is divided into four elements across the flange widths given in Table 5.1. The width of the six web elements varies depending on their proximity to the flanges. The web elements nearest the flanges have the smallest width. The web elements near the center of the web are the widest. Eight noded thick-shell elements are used for each element.

The half-span models for the 50 m span include 125 elements along the length. The length of each element is 200 mm (7.87 inches). The flange and web element widths are determined in the same manner as those of the 33.5 m span girder.

Figure 6.3 depicts the simplified steel stress-strain relationship used in the finite element models. The elastic modulus, E, is 200,000 MPa (29,000 ksi), and the Poisson's ratio, ν, is 0.295. Two types of steel were modeled. For the first type of steel, the yield strength, F_y, is 485 MPa (70 ksi), and the ultimate strength, F_u, is 620 MPa (90 ksi). For the second type of steel, the yield strength, F_y, is 690 MPa (100 ksi), and the ultimate strength, F_u, is 760 MPa (110 ksi).

Figure 6.4 shows the residual stress pattern used in the model. The finite element package utilized for the analysis only allowed a constant initial stress over a single element. The model for the residual stresses in the flanges was highly simplified. The outside elements of each flange had a compressive residual stress of 120 MPa (17.4 ksi) and the interior elements had an equal tensile residual stress. The value of the residual stress in the models is based on the value of residual stress, F_r, specified for welded beams in AISC (1994).

The initial out-of-straightness is defined in the model as described in Section 4.3.2. The compression (top) flange in the girder is laterally deflected. The tension flange is assumed to be straight. The web has increasing lateral deflection along its height as determined by Equation 4.2. At the points of lateral support (diaphragms) and at the support end (bearings) of the model, the initial lateral deflection of the compression flange and the web is zero. The maximum initial deflection of the compression flange between points of lateral support was set to $L_b/1000$. For all of the models, the principal unbraced length (that with largest demand moment) was used to determine the maximum initial lateral deflection.

Figure 6.5 shows the initial out-of-straightness for the 33.5 m span models with the standard diaphragms. The maximum 5.9 mm (0.23 in) initial lateral deflection is at the middle of each unbraced length. Figure 6.6 shows the initial out-of-straightness for the 50 m span models with the standard diaphragms. The maximum 7.2 mm (0.28 in) initial lateral deflection is at the middle of each unbraced length.

Two different initial out-of straightness values were used for the models with FRRBs. The first case has the maximum initial lateral deflection determined as $L_b/1000$ using the increased unbraced length used with the FRRBs. The second case has the same maximum initial lateral deflection as the corresponding model with standard diaphragms. Figure 6.7 shows the initial out-of-straightness for the 33.5 m span models with FRRBs. The maximum initial lateral deflection of 9.0 mm (0.35 in) is used in the first case. The second case has a maximum initial lateral deflection of 5.9 mm (0.23 in). Figure 6.8 shows the initial out-of-straightness for the 50 m span models with FRRBs. The maximum initial lateral deflection of 11.0 mm (0.43 in) is used in the first case. The second case has a maximum initial lateral deflection of 7.2 mm (0.28 in).

The boundary conditions were used to impose symmetry at the midspan cross-section, to model the lateral support from both the standard diaphragms and the diaphragms with FRRBs, and to model the support end of the girder. Figure 3.9 shows the cross-section of the model at the midspan; the definition of the points shown in the figure is given in Section 3.3.2. Table 6.1 lists the boundary conditions for each point at the midspan. The web displacements at midspan are controlled through point A. It is assumed that the web does not distort at this cross-section, thus points B and C are rigidly constrained to point A. The remaining boundary conditions are required by the symmetry conditions at midspan. Figure 3.9 can also be used to describe the boundary conditions at each of the lateral supports (standard diaphragm or diaphragm with FRRB). Table 6.2 lists the boundary conditions for the cross-sections at lateral supports. The web displacements are controlled through point A. The web is restrained from twisting and lateral deflection, and does not distort (to model the diaphragm connection plate), thus points B and C are rigidly constrained to point A. Figure 3.10 shows a cross-section of the model at the support end. Table 6.3 lists the boundary conditions for the support end. The support conditions are controlled through point C. The web is not permitted to distort.

Figure 6.9 shows the boundary conditions at the midspan of each FRRB. As shown, only half of the FRRBs was included on the models because of symmetry. Figure 6.9 is an isometric view of a portion of the compression flange and the portion of the FRRB included in the model. The vertical and longitudinal deflections (relative to the span) are free while the lateral deflection is restrained. The FRRB can twist about its own longitudinal axis, but is restrained from rotation about the other two axes.

All of the models were loaded by applying a pressure on the compression (top) flange to model the loading imposed during the construction stage of the prototype highway bridge.

The pressure acts across the width of the flange and along the length of the span. Corresponding reactions and moments are determined from the flange pressure.

6.3 Results of Analysis

6.3.1 General Results

Each prototype girder was analyzed with standard diaphragms at the original unbraced length and with diaphragms with FRRBs at the increased unbraced length. Two analyses were run for the girders with the FRRBs. The first case had the large initial out-of-straightness shown in Figures 6.7 and the second case had the smaller initial out-of-straightness. The lateral-torsional buckling resistance determined from the finite element analyses was compared with the results obtained from the appropriate AASHTO LRFD equations (for standard diaphragms) and the results from the AASHTO LRFD equations using effective length (K) factors determined by the analyses discussed in Chapter 5. The cases considered for each prototype girder are as follows:

(1) AASHTO: AASHTO LRFD lateral-torsional buckling capacity for girder with standard diaphragms at L_b,
(2) FE: finite element analysis of girder with standard diaphragms at L_b,
(3) AASHTO K - FD: AASHTO LRFD lateral-torsional buckling capacity for girder with FRRBs calculated using L_{eff} with K from finite difference analysis,
(4) AASHTO K - AC: AASHTO LRFD lateral-torsional buckling capacity for girder with FRRBs with capacity calculated using L_{eff} with K from alignment chart analysis,
(5) FE - A: finite element analysis for girder with FRRBs at L_b^{FRRB} and larger initial out-of straightness, and
(6) FE - B: finite element analysis for girder with FRRBs at L_b^{FRRB} and smaller initial out-of straightness.

The finite element analysis results are compared to the other results to establish the accuracy of the analysis methods described in Chapter 5. Table 6.4 lists the lateral-torsional

buckling moment capacities for the 33.5 m span girder for the cases listed above. Table 6.5 lists the lateral-torsional buckling moment capacities for the 50 m span girder for the cases listed above. The finite element analysis results compare reasonably well to the results from the other analysis methods.

6.3.2 Discussion of Selected Cases

Two of the finite element analyses of girders with FRRBs are discussed to provide insight into the behavior of girders with FRRBs. The finite element results for the 33.5 m span 690 MPa yield strength steel girder and the 50 m span 485 MPa yield strength steel girder are further investigated. The results for the cases with smaller initial out-of-straightness are discussed.

Figure 6.10 shows the location of the nodes used in the discussion of the 33.5 m span 690 MPa yield strength girder. All of the nodes are at the midspan of the girder. The vertical (y axis) deflection is labeled *u2* for each node, and the transverse (x axis) deflection is labeled *u3*. Figure 6.11 shows the location of elements used in the discussion of the results for the 33.5 m span 690 MPa yield strength girder. The elements are adjacent to the midspan of the girder. The stresses and strains in each direction are given at the top and bottom surfaces of each element. The circles on the figure show the location of where the stresses and strains are reported.

Figure 6.12 shows the location of the nodes used in the discussion of the 50 m span 485 MPa yield strength girder. All of the nodes in the figure are at the location of maximum lateral deflection of the compression flange. The vertical (y axis) deflection is labeled *u2* for each node, and the transverse (x axis) deflection is labeled *u3*. Figure 6.13 shows the location of elements used in the discussion of the results for the 50 m span 485 MPa yield strength girder. The elements are at the location of maximum lateral deflection. The circles on the figure show the location of where the stresses and strains are reported.

Figure 6.14 shows the normalized moment versus midspan deflection for the 33.5 m span 690 MPa yield strength steel girder with FRRBs. The location of the nodes is given in Figure 6.10. The theoretical elastic deflection (from beam theory) compares very well to the vertical deflection until the beam experiences significant lateral deflections.

Figure 6.15 shows the deflected shape of a portion of the finite element model at the final step of the analysis. The view is from the midspan to slightly beyond the FRRB nearest the midspan. The displacement has been magnified and the view rotated. Some distortion can be seen in the web.

Figure 6.16 shows the normalized moment versus strain near the midspan of the 33.5 m span 690 MPa yield strength girder. The location of the elements is shown in Figure 6.11. Figure 6.16 shows the occurrence of the lateral-torsional buckling. The strain separation begins early in the analysis. There is some strain separation between the top and bottom surface at one flange tip (top and bottom of element 1301), but a local buckle does not form.

Figure 6.17 shows the normalized moment versus deflection for the 50 m span length 485 MPa yield strength steel girder with FRRBs. The lateral deflections are at the location of the maximum lateral deflection of the compression flange. The location of the nodes on the cross-section is given in Figure 6.12. The vertical deflection is given for node 25300 which occurs at the compression flange-to-web connection at midspan. The theoretical elastic deflection compares well to the vertical deflection until the beam experiences significant lateral deflections.

Figure 6.18 shows the deflected shape of a portion of the finite element model at the final step of the analysis. The view is from the midspan FRRB to slightly beyond the FRRB nearest the midspan. The displacement has been magnified and the view rotated. A significant amount of distortion can be seen in the web.

Figure 6.19 shows the normalized moment versus strain at the location of the maximum lateral deflection of the compression flange for the 50 m span 485 MPa yield strength girder. The location of the elements is shown in Figure 6.13. Figure 6.19 shows the occurrence of lateral-torsional buckling in the 50 m span length. The strain separation begins to occur early in the analysis, but does not diverge as rapidly as the strains for the 33.5 m span 690 MPa yield strength girder shown in Figure 6.16.

Both of the girders behaved as expected for girders undergoing lateral-torsional buckling. The vertical and lateral deflections are similar to the results of the finite element models developed in Chapter 4.

6.4 Summary

Finite element analyses were conducted to investigate the lateral-torsional behavior of the prototype girders with FRRBs. The finite element models were based on the models developed in Chapter 4. The finite element analysis results were compared to the lateral-torsional buckling moment capacities from AASHTO LRFD design equations using K factors from the finite difference and alignment chart analyses. The finite element analysis results also provided insight into the lateral-torsional buckling behavior of girders with standard diaphragms and with diaphragms with FRRBs.

Table 6.4 shows the lateral-torsional buckling moment capacities for the 33.5 m span girders. Table 6.5 shows the lateral-torsional buckling moment capacities for the 50 m span girders. The lateral-torsional buckling moment obtained from the finite element analyses for the girders with standard diaphragms exceeded that obtained from the AASHTO LRFD equations. The comparisons of the results for the girders with FRRBs is more difficult to generalize. For the 33.5 m span 485 MPa yield strength steel girder, the lateral-torsional buckling moment from the finite element analyses were less than the lateral-torsional buckling moments determined

from the AASHTO LRFD equations with the K factors. For the 50 m span 690 MPa yield strength steel girder, the lateral-torsional buckling from the finite element analyses were greater than the lateral-torsional moments determined from the AASHTO LRFD (1994) equations with the K factors. For the other two girders, the lateral-torsional buckling moment for the finite element model with larger initial out-of-straightness exceeded only the lateral-torsional buckling moment calculated using K factors from the finite difference analysis. The lateral-torsional buckling moment for the finite element model with smaller initial out-of-straightness exceeded the lateral-torsional buckling moment calculated using K factors from both analysis methods.

Table 6.1 Boundary conditions at midspan of finite element models

DOF	Location				
	A	A'	B	C	C'
Δx	free	free	rigid constraint to point A	rigid constraint to point A	free
Δy	free	free	"	"	free
Δz	fixed	fixed	"	"	fixed
θx	fixed	fixed	"	"	fixed
θy	fixed	fixed	"	"	fixed
θz	free	free	"	"	free

Table 6.2 Boundary conditions at lateral supports of finite element models

DOF	Location				
	A	A'	B	C	C'
Δx	fixed	free	rigid constraint to point A	rigid constraint to point A	free
Δy	free	free	"	"	free
Δz	free	free	"	"	free
θx	free	free	"	"	free
θy	free	free	"	"	free
θz	fixed	free	"	"	free

Table 6.3 Boundary conditions at support end of finite element models

DOF	Location				
	A	A'	B	C	C'
Δx	rigid constraint to point C	free	rigid constraint to point C	fixed	free
Δy	"	free	"	fixed	fixed
Δz	"	free	"	free	free
θx	"	free	"	free	free
θy	"	free	"	free	free
θz	"	free	"	fixed	fixed

Table 6.4 Lateral-torsional buckling moment capacities for 33.5 m span girders

Yield Strength (MPa)	33.5 m Span Lateral-torsional Buckling Moments (kN-m)					
	Standard Diaphragms		Diaphragms with FRRBs			
	AASHTO	FE	AASHTO *K* - FD	AASHTO *K* - AC	FE - A	FE - B
485	5,266	5,507	5,164	5,336	4,897	5,124
690	4,994	5,745	4,867	5,081	4,915	5,106

Table 6.5 Lateral-torsional buckling moment capacities for 50 m span girders

Yield Strength (MPa)	50 m Span Lateral-torsional Buckling Moments (kN-m)					
	Standard Diaphragms		Diaphragms with FRRBs			
	AASHTO	FE	AASHTO *K* - FD	AASHTO *K* - AC	FE - A	FE - B
485	11,283	11,820	10,868	11,390	11,050	11,502
690	10,638	12,352	10,446	11,183	11,977	12,492

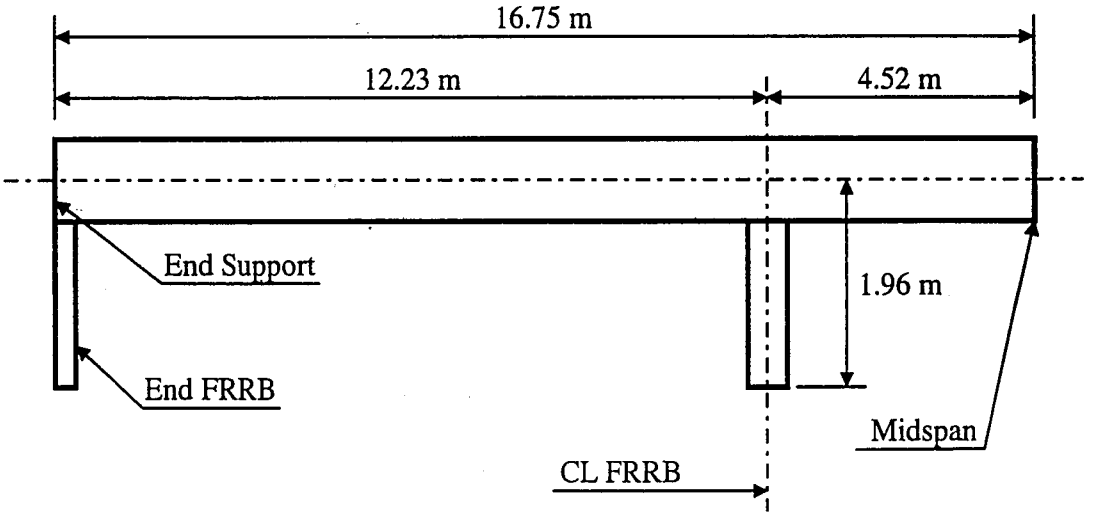

Figure 6.1 Top flange plan for 33.5 m span girder

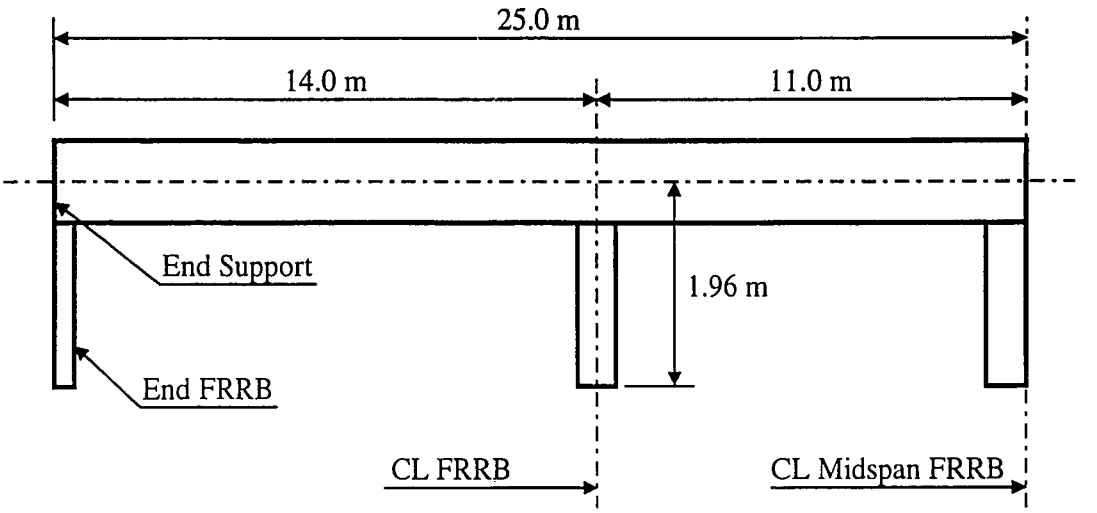

Figure 6.2 Top flange plan for 50 m span girder

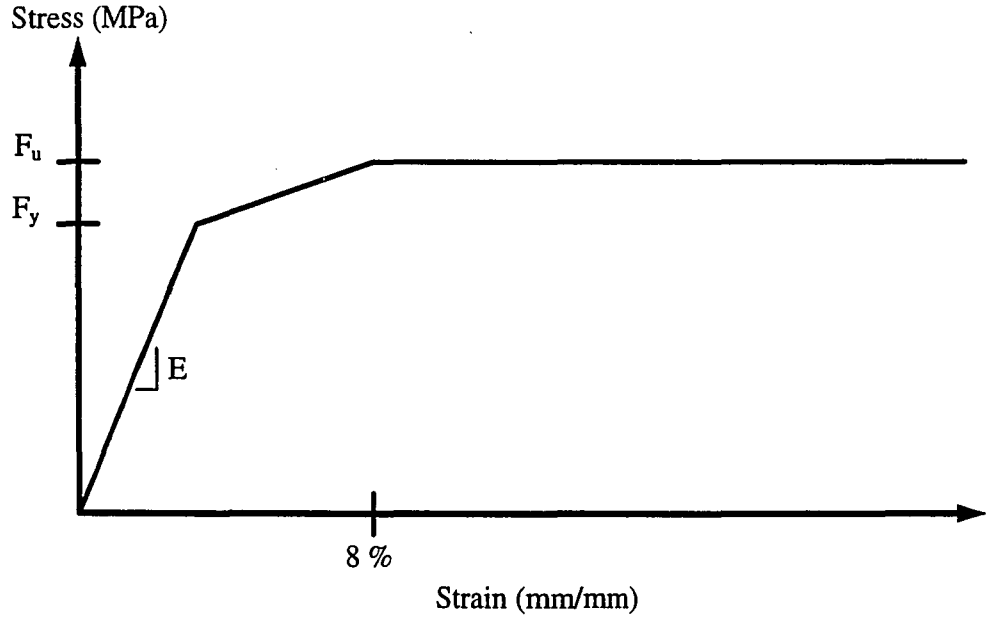

Figure 6.3 Stress-strain relationship used in finite element models

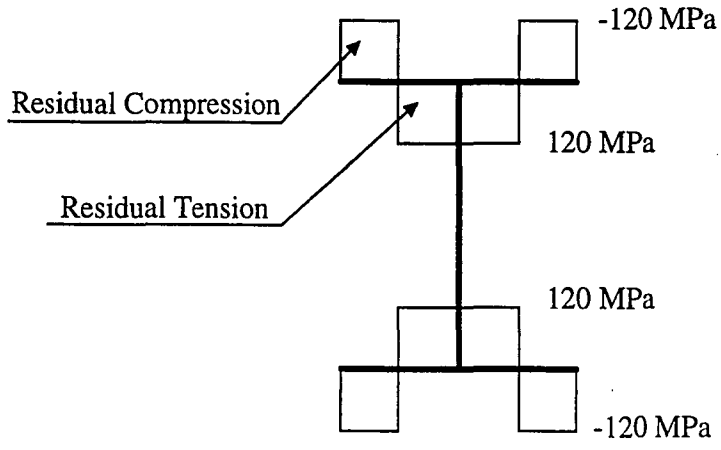

Figure 6.4 Residual stress distribution used in finite element models

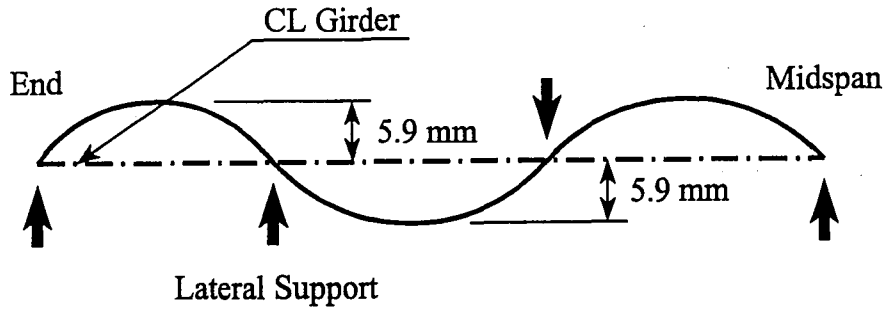

Figure 6.5 Initial out-of-straightness for 33.5 m span girder with standard diaphragms

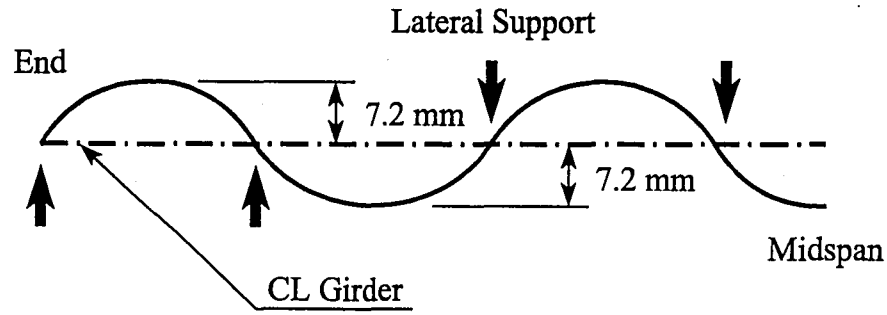

Figure 6.6 Initial out-of-straightness for 50 m span girder with standard diaphragms

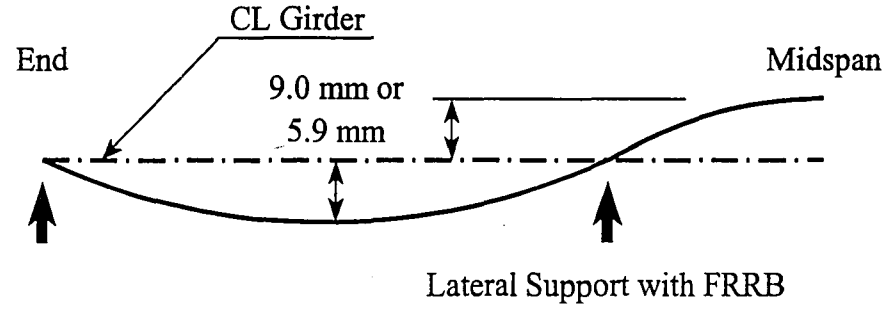

Figure 6.7 Initial out-of-straightness for 33.5 m span girder with FRRBs

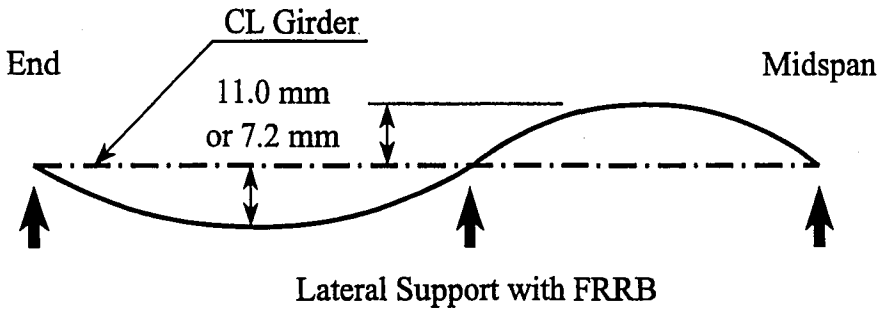

Figure 6.8 Initial out-of-straightness for 50 m span girder with FRRBs

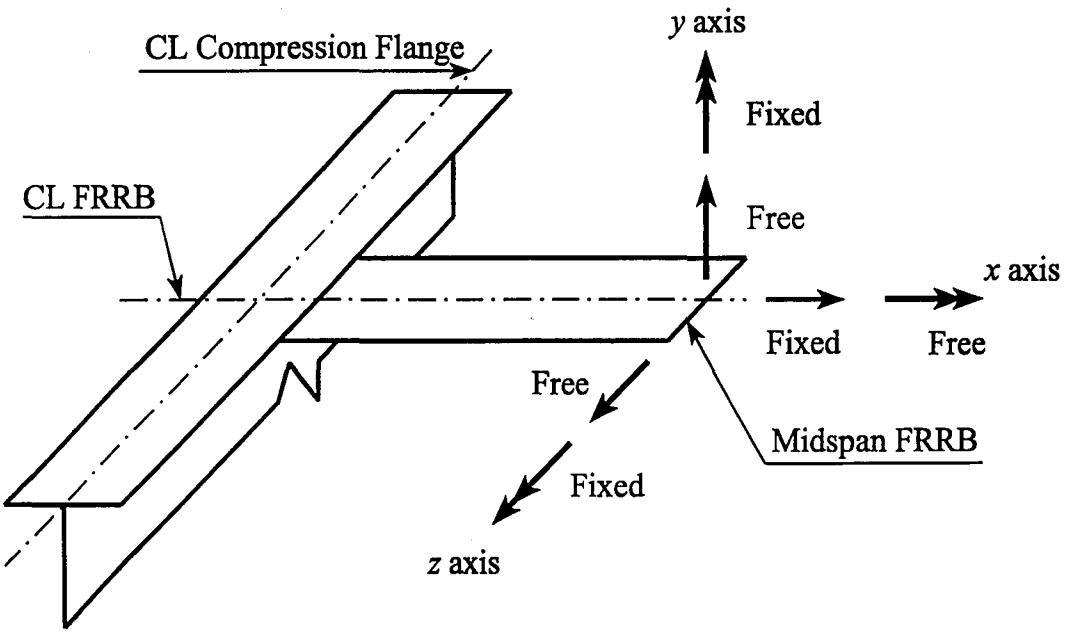

Figure 6.9 Boundary conditions at midspan of FRRB

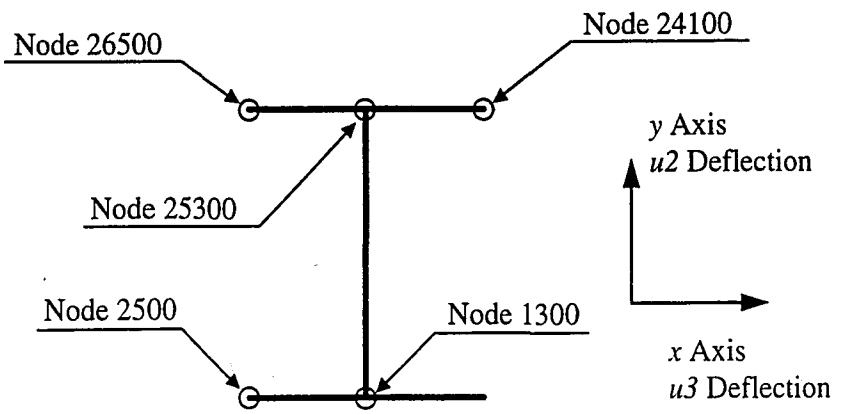

Figure 6.10 Location of nodes at midspan of 33.5 m span girder

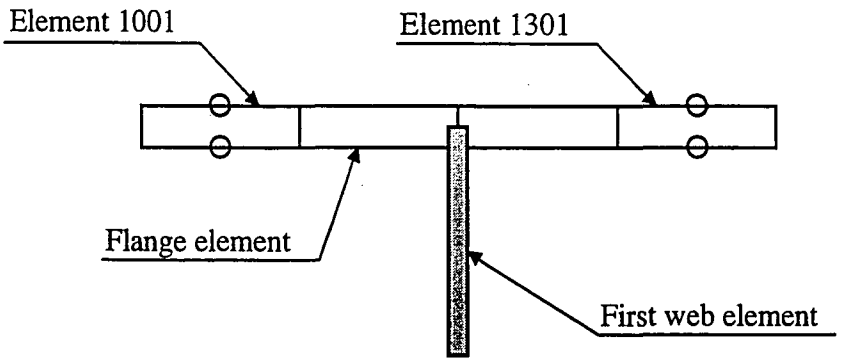

Figure 6.11 Location of elements adjacent to midspan of 33.5 m span girder

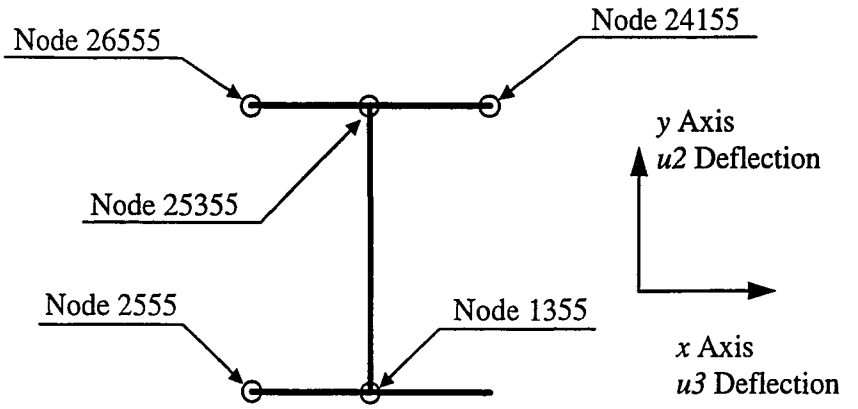

Figure 6.12 Location of nodes at point of maximum lateral deflection of 50 m span girder

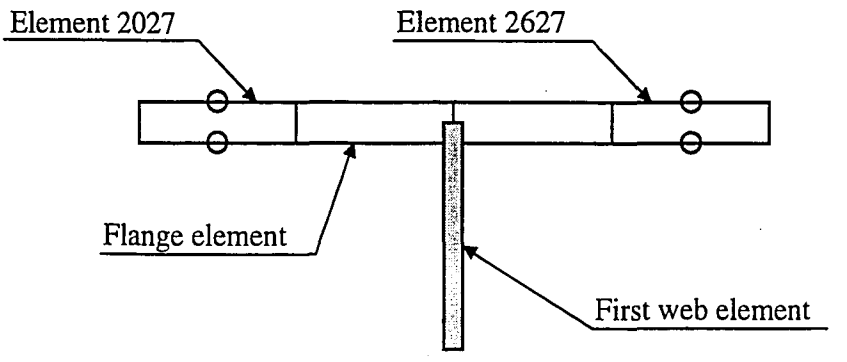

Figure 6.13 Location of elements at point of maximum lateral deflection of 50 m span girder

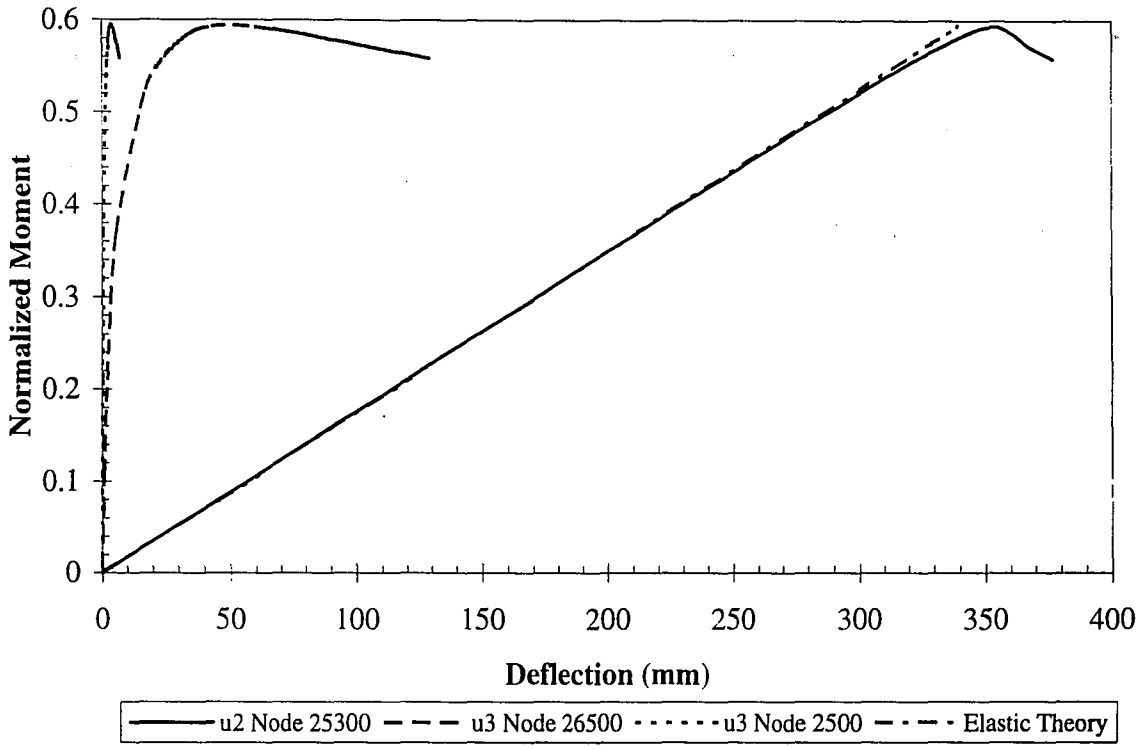

Figure 6.14 Normalized moment versus deflection for finite element model of 33.5 m span 690 MPa yield strength steel girder with smaller initial out-of-straightness

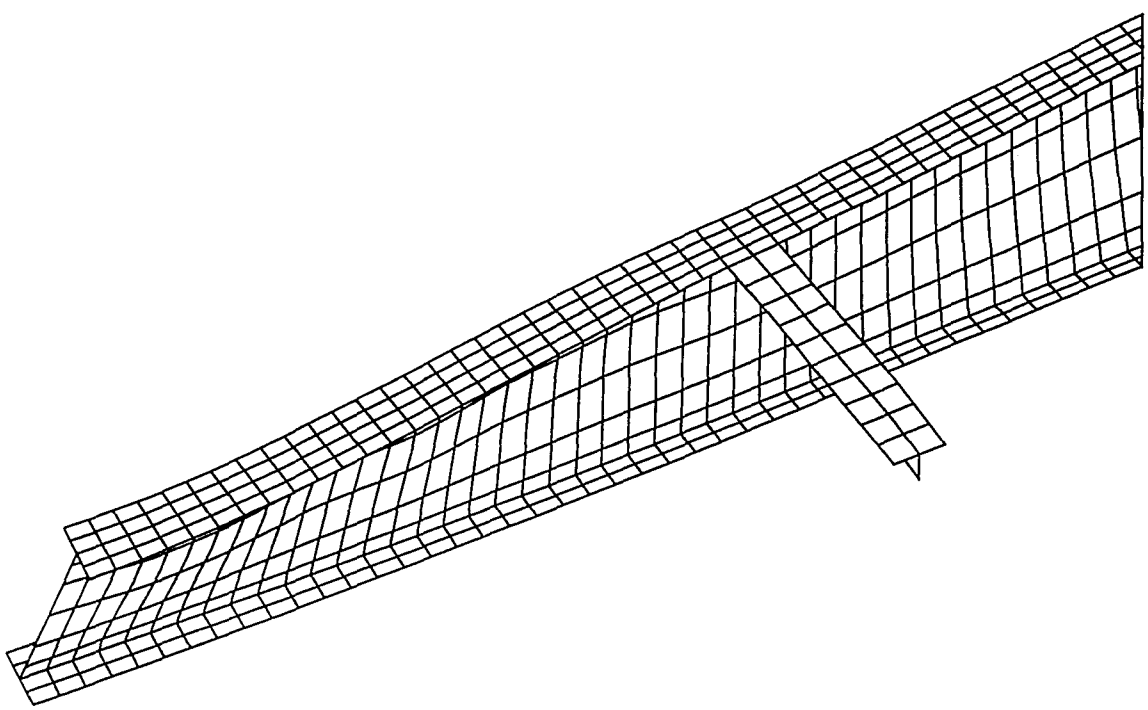

Figure 6.15 Deflected shape for primary unbraced length of finite element model of 33.5 m span 690 MPa yield strength steel girder with smaller initial out-of-straightness

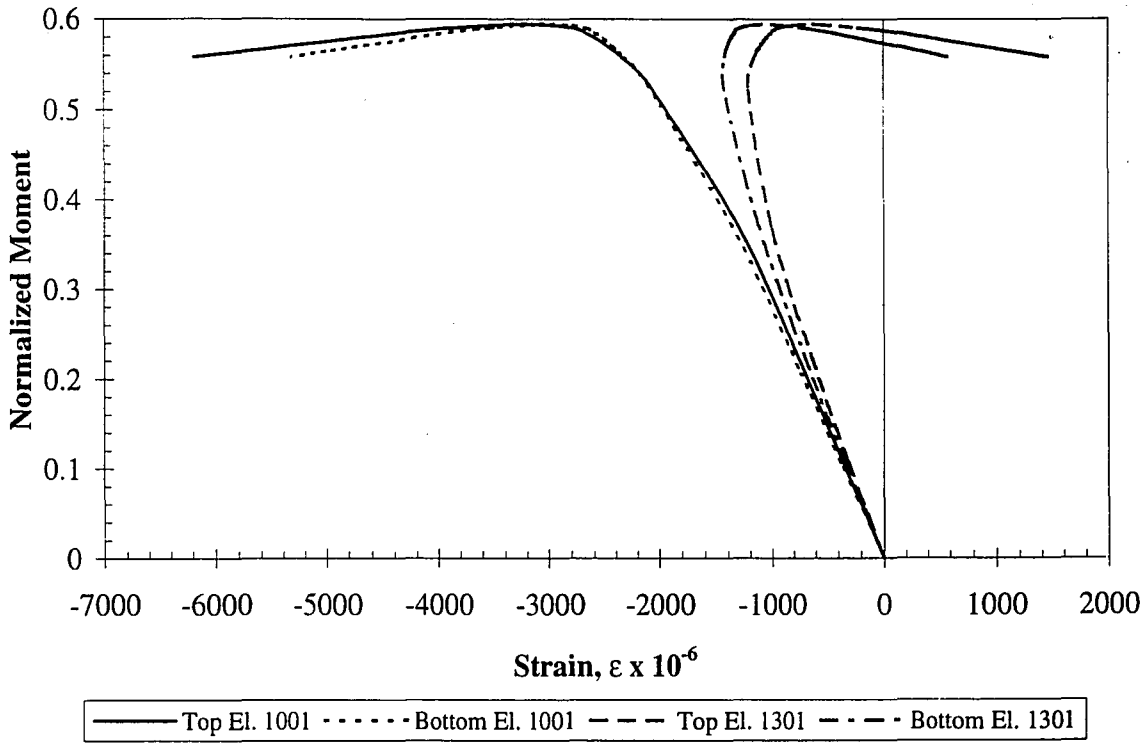

Figure 6.16 Normalized moment versus longitudinal strain in compression flange for finite element model of 33.5 m span 690 MPa yield strength steel girder with smaller initial out-of-straightness

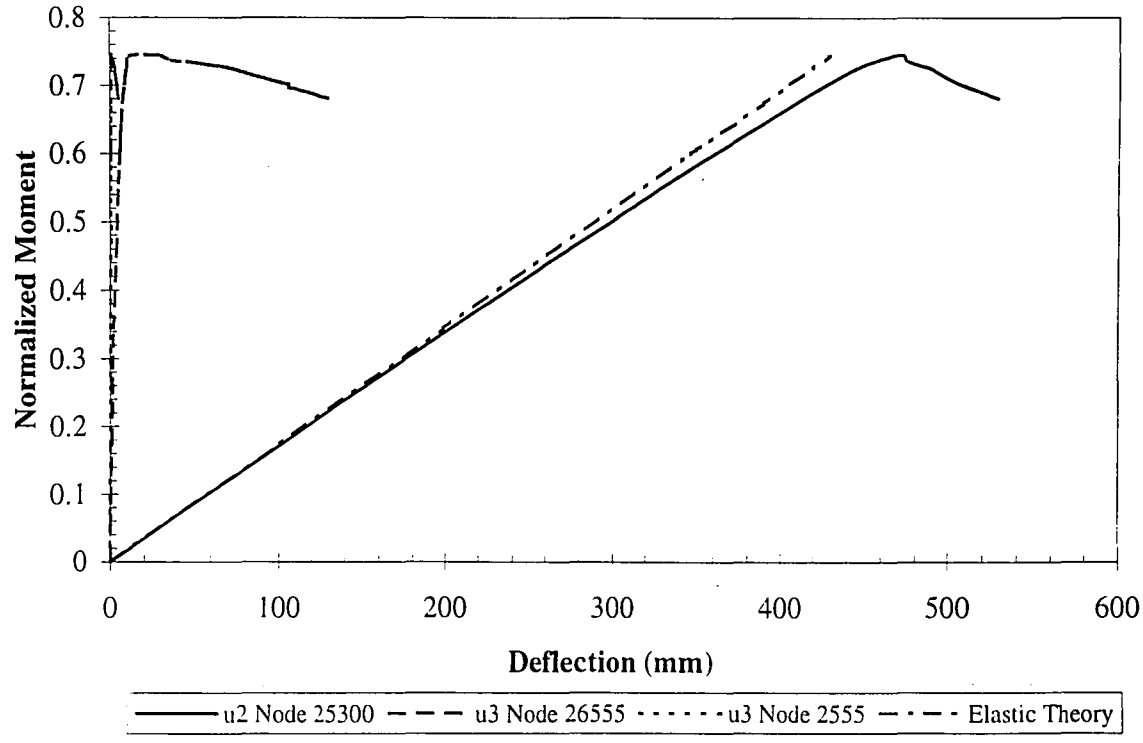

Figure 6.17 Normalized moment versus deflection for finite element model of 50 m span 485 MPa yield strength steel girder with smaller initial out-of-straightness

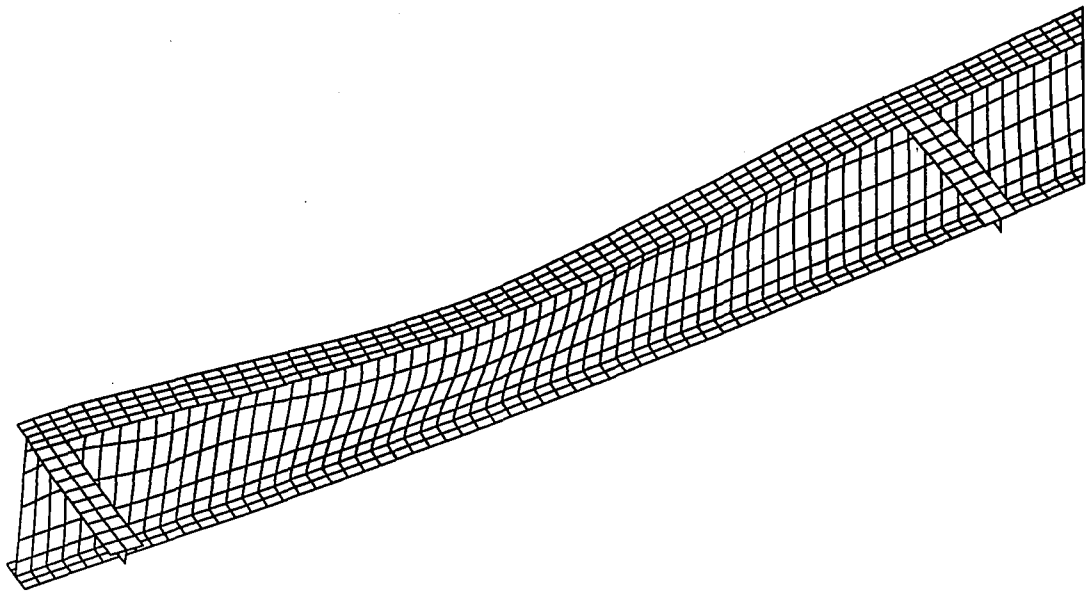

Figure 6.18 Deflected shape for primary unbraced length of finite element model of 50 m span 485 MPa yield strength steel girder with smaller initial out-of-straightness

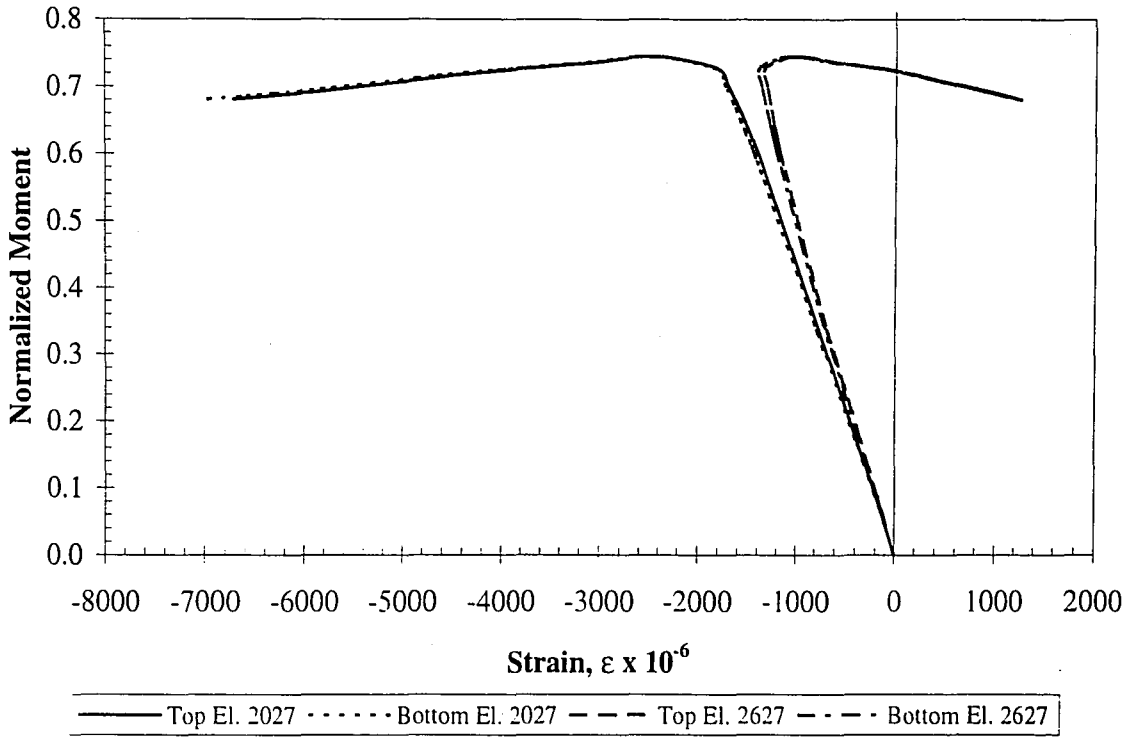

Figure 6.19 Normalized moment versus longitudinal strain in compression flange for finite element model of 50 m span 485 MPa yield strength steel girder with smaller initial out-of-straightness

7. Conclusions, and Future Work

7.1 Conclusions

This thesis presented research investigating the use of high performance steel (HPS) I-girders with flange rotational restraint braces (FRRB). The research is part of a project entitled "Innovative Bridge Designs Using High Performance Steels." Previous research on the project has determined that buckling design limits are one of the barriers to the use of HPS in I-girder bridges. HPS girders can have slender components with low buckling resistance. Lateral-torsional buckling of HPS girders is a concern during the construction stage when the compression flange in the positive moment region is not yet composite with the concrete deck and is laterally supported only at the diaphragms. The use of FRRBs permits an increase in the diaphragm spacing without an increase in the cross-section dimensions of the girder. Increased diaphragm spacing can increase the economy of steel I-girder bridges.

Three bridge girder design concepts were discussed in the thesis. The FRRB design concept allows greater diaphragm spacing by improving the lateral-torsional buckling behavior of bridge I-girders. The batten plate concept increases the torsional resistance of the I-girder cross-section. It was found that the use of batten plates did not substantially reduce the need for diaphragms. The girder pair design concept can be used with or without the FRRB design concept to increase the economy of an I-girder bridge.

Finite element models were developed to simulate the lateral-torsional buckling behavior of girders and the effect of FRRBs on the lateral-torsional buckling of girders. Test data from Kubo and Fukumoto (1988) was used to calibrate the finite element models. The parameters that influenced the buckling behavior of the models were investigated. Two of the most important modeling parameters were the initial out-of-straightness and the residual stresses in the flanges. Several conclusions were drawn from the development and analysis of

these finite element models. First, finite element models can adequately simulate the lateral-torsional buckling behavior of I-shaped girders. Second, modified finite element models with FRRBs had greater lateral-torsional buckling capacity than the models of the girder without FRRBs.

Although finite element models can be used to simulate the lateral-torsional buckling behavior of I-girders both with and without FRRBs, simpler analytical approaches were developed for use in design. Two analysis methods were investigated to determine the lateral-torsional buckling capacity of girders with FRRBs. The first analysis method used the finite difference method to determine the elastic lateral-torsional buckling moment of the girder with and without FRRBs. The FRRBs were included in the finite difference model by modifying the boundary conditions to include the rotational stiffness of the FRRB. An effective length (K) factor was determined by comparing the lateral-torsional buckling capacities of the girder with and without FRRBs. The second analysis method was based on the alignment charts that are used to determine K factors for columns and other compression members in braced frames. The two analysis methods provided similar results for several prototype girders. The K factors determined from the two analysis methods were used to determine the effective unbraced lengths for the prototype girders with FRRBs. The effective lengths were used with AASHTO LRFD (1994) lateral-torsional buckling design specifications to allow inelastic lateral-torsional buckling and web slenderness effects to be included in determining the lateral-torsional buckling capacity of the prototype girders.

Finite element models of the prototype girders were used to verify the results of the simpler analysis methods. The finite element analysis results were compared to the results obtained using the K factors with the AASHTO LRFD design equations. The finite element analysis results compared well with the results from the simpler analysis methods.

The FRRB design concept can be used to increase the spacing of diaphragms in steel I-girder highway bridges by improving the lateral-torsional buckling behavior of the I-girders, in particular during the construction stage. The effectiveness of FRRBs can be determined using the proposed analysis methods. When necessary, finite element models can be used to simulate the lateral-torsional buckling behavior of girders with and without FRRBs.

7.2 Future Work

To exploit the potential advantages of FRRBs in highway bridges, laboratory experiments are needed to verify the analytical results presented in this thesis. Tests of I-girders with FRRBs would verify the behavior of girders with FRRBs as discussed in this thesis.

Tests of a girder pair with full-length FRRBs spanning between the girders would further verify the effectiveness of the FRRBs and verify the analysis results. The tests would also validate the girder pair concept. The stability of girder pairs, with or without FRRBs, could be determined.

Further analytical studies should be performed. The properties of the I-girders should be more widely varied, and a larger number of I-girders should be analyzed. More rigorous finite element models should be developed. The modeling of residual stresses and initial out-of-straightness should be improved to achieve more consistent comparisons with experimental results.

Costs analyses should be performed to compare the economy of bridges with FRRBs spacing with that of bridges with conventional diaphragms. The cost analyses should compare the fabrication costs of diaphragms with FRRBs and the fabrication costs of standard diaphragms. The effects of different methods of installation of the FRRB, such as shop-installation or field installation, should be included in the cost analysis.

References

AASHTO LRFD Bridge Design Specifications, American Association of State Highway and Transportation Officials, Washington, DC, 1994.

AASHTO Standard Specifications for Highway Bridges, American Association of State Highway and Transportation Officials, Washington, DC, 1992.

ACI Building Code Requirements for Structural Concrete and Commentary, American Concrete Institute, Farmington Hills, Michigan, 1995.

AISC Manual of Steel Construction: Load & Resistance Factor Design, Vol. 1, American Institute of Steel Construction, Chicago, 1994.

Austin, W. J., S. Yegian, and T. P. Tung, "Lateral Buckling of Elastically End-restrained I-beams," *Transactions*, Vol. 122, ASCE, 1957.

Czaplicki, N. A., R. Sause, S. S. Murphy, M. D. Cortes, and F. J. Perez, *Design and Behavior of High Performance I-Girders with Composite Webs*, ATLSS Report No. 96-13, Lehigh University, Bethlehem, PA, 1996.

Galambos, T. V., *Structural Members and Frames*, Prentice-Hall, Englewood Cliffs, NJ, 1968.

Galambos, T. V., "Inelastic Lateral Buckling of Beams," *Journal of the Structural Division*, Vol. 89 (ST5), ASCE, October, 1963.

Guide to Stability Design Criteria for Metal Structures, Structural Stability Research Council, Wiley, New York, 1988.

Helwig, T. A., and K. H. Frank, "Bracing of Steel Girders by Metal Deck Forms," *Proceedings of Structures Congress XIII*, ASCE, 1995.

Huzzard, R. K., and R. P. Alpago, "Economic Details for Bridges: Cross Frames and Cross Frame Connections," Technical Bulletin No. TB-315A, Bethlehem Steel Corporation, Bethlehem, PA, 1996.

Kavanagh, T. C., "Effective Length of Framed Columns," *Transactions*, Vol. 127, Part II, ASCE, 1962.

Kitipornchai, S., and N. S. Trahair, "Buckling Properties of Monosymmetric I-Beams," *Journal of the Structural Division*, Vol. 106 (ST5), ASCE, 1980.

Kubo, M., and Y. Fukumoto, "Lateral-Torsional Buckling of Thin-Walled I-Beams," *Journal of Structural Engineering*, Vol. 114, No. 4, ASCE, 1988.

Mertz, D. R., "Cross-Frame Diaphragms for Steel Girder Bridges Using *the AASHTO LRFD Bridge Design Specifications*," *Proceedings of Structures Congress XIV*, ASCE, 1996.

Sause, R., and J. W. Fisher. "Application of High Performance Steel in Highway Bridges," *Proceedings of the International Symposium on High Performance Steels for Structural Applications*, ASM International, 1995.

Szewczak, R. M., E. A. Smith, and J. T. DeWolf "Beams with Torsional Stiffeners," *Journal of Structural Engineering*, Vol. 109, No. 7, ASCE, 1983.

Takabatake, H., S. Kusumoto, and T. Inoue, "Lateral Buckling Behavior of *I* Beams Stiffened with Stiffeners," *Journal of Structural Engineering*, Vol. 117, No. 11, ASCE, 1991.

Takabatake, H., "Lateral Buckling of *I* Beams with Web Stiffeners and Batten Plates," *International Journal of Solid Structures*, Vol. 24, No. 10, Pergamon Press, London, 1988.

Vita

Sean Stephen Murphy was born in Springfield, Massachusetts, on January 13, 1968. He is the son of Dr. Russell Elliot Murphy and Dr. Susan Katherine Hopkins Kurjiaka. Mr. Murphy obtained his Bachelor of Science degree in civil engineering from Lehigh University in June 1990. At Lehigh University, Mr. Murphy was a National Merit Scholar. He was a structural engineer at The RBA Group in Morristown, New Jersey, and New York City between June 1990 and July 1993. He then attended Clemson University where he was a research and teaching assistant. He performed research on natural hazard mitigation for low-rise structures. At Clemson University, Mr. Murphy was initiated into Chi Epsilon, the national civil engineering honor society. Mr. Murphy received the Master of Science degree in civil engineering from Clemson University in May 1995. He then attended Lehigh University where he was a research scholar at the ATLSS Engineering Research Center. Mr. Murphy will receive the Master of Science degree in civil and environmental engineering from Lehigh University in June 1997. After graduation, Mr. Murphy will be working at Erdman Anthony Associates as a structural engineer in Mechanicsburg, Pennsylvania.

END OF TITLE